UNIVERSIDADE BEIRA INTERIOR

Development of IR780 based nanoparticles for photothermal therapy of breast cancer

Cátia Gomes Alves

Tese para obtenção do Grau de Doutor em
Biomedicina
(3º ciclo de estudos)

Orientador: Prof. Doutor Ilídio Joaquim Sobreira Correia
Co-orientador: Prof. Doutor Duarte Miguel de Melo Diogo

Júri:

Prof. Doutor Joaquim Mateus Paulo Serra
Profª. Doutora Maria de La Salette Hipólito Reis
Prof. Doutor Ricardo Saraiva Loureiro de Oliveira Louro
Prof. Doutor António José Geraldes de Mendonça
Profª. Doutora Sandra Pucciarelli
Doutora Ana Sofia Matias da Silva
Prof. Doutor Duarte Miguel de Melo Diogo

20 de março de 2023

Declaração de Integridade

Eu, Cátia Gomes Alves, que abaixo assino, estudante com o número de inscrição D2443 de/o Biomedicina da Faculdade de Ciências da Saúde, declaro ter desenvolvido o presente trabalho e elaborado o presente texto em total consonância com o **Código de Integridades da Universidade da Beira Interior**.

Mais concretamente afirmo não ter incorrido em qualquer das variedades de Fraude Académica, e que aqui declaro conhecer, que em particular atendi à exigida referenciação de frases, extratos, imagens e outras formas de trabalho intelectual, e assumindo assim na íntegra as responsabilidades da autoria.

Universidade da Beira Interior, Covilhã 23/03/2023

Assinado por: **CÁTIA GOMES ALVES**
Num. de Identificação: 14541053
Data: 2023.03.23 17:26:47+00'00'

- A mistake that makes you humble
is better than an achievement that makes you arrogant.

- Não existe nada permanente,
a não ser a mudança.

Foi graças a vocês e para vocês,
Mãe, Pai, Avozinha, Nuno, Ikas, Ricardo, Dora, Lucas, L., B.

Agradecimentos

Em primeiro lugar, gostaria de agradecer ao meu orientador, Professor Doutor Ilídio Correia e ao meu co-orientador, Doutor Duarte Diogo. Queria agradecer-lhes a oportunidade de realizar a minha tese de mestrado e de seguida, tese de doutoramento sob a sua orientação. Para além disto, um muito obrigado por todas as ajudas, ensinamentos, e lições que me ensinaram ao longo destes mais de 5 anos, que me ajudaram a crescer como profissional e como pessoa.

De seguida, queria agradecer à Universidade da Beira Interior e ao Centro de Investigação em Ciências da Saúde (CICS-UBI) por providenciarem as instalações e os equipamentos necessários à realização desta tese de doutoramento.

Para além disto, gostaria de agradecer à Fundação para a Ciência e a Tecnologia (FCT) por me providenciar financiamento através de uma bolsa individual de doutoramento (SFRH/BD/145386/2019).

A todo o grupo de trabalho, um muito obrigado por todas as ajudas e ambiente vivenciado. Ao André, e aos mini-PhD (Nata, Bruna, Mariana), obrigada pelas conversas, principalmente por ouvirem, pela paciência e pelas sessões motivacionais! Há coisas que o tempo trouxe, que jamais serão apagadas. Aos "miúdos" deste ano e os restantes que co-orientei, espero que não se tenham fartado de me ouvir, e que tenham aprendido algo de bom. Obrigada por tudo aquilo que também me foram ensinando.

Às minhas Frozens, Carol, Rita, Sol, a vocês, não tenho palavras para agradecer. É incrível como aquilo que começa por ser "colegas de tese" (por vezes até chatinhas!) passa a ser a nossa mais-valia para superar tudo o que nos aparece à frente! Com vocês ri, chorei, passei os piores e os melhores momentos! Venha o que vier, as gargalhadas em conjunto já ficaram tatuadas! Com vocês aprendi o mais importante, científico e não científico! Aprendi o que é ter alguém sempre do nosso lado, mesmo quando tudo parece estar do avesso. Se não fossem as minhas Frozens, bem sei que há coisas que não tinha aguentado. Obrigada! Obrigada por tudo, por toda a motivação e por serem as melhores companheiras de gabinete de sempre! Dizem que temos de olhar sempre para o lado bom…vocês são e serão sempre o lado bom disto! #FNC4ever! Vocês são como "aquelas pessoas-bússola, que seguem sempre ao nosso lado e não nos deixam cair quando as pernas tremem, a estas, não as podemos perder de vista".

Às minhas meninas de sempre, Chica, Inês, Andreia, Ritinha, obrigada por, mesmo passados 4 anos da última vez que escrevi algo do género, continuarem a estar comigo

em todos os momentos, apesar da distância! O que a UBI juntou, já nada separa! Se me aguentaram todos estes anos, também já não se vão ver livres depois disto! Venham mais festaças! Já que, aqueles encontros, apesar de esporádicos, fazem parecer que continuamos a viver na melhor casa da Anil ou a ir a todas as aulas juntas!

De seguida queria agradecer à minha família, à minha mãe, ao meu pai, à minha avozinha, aos meus irmãos, Nuno e Ikas, à Dorita, ao meu Luquinhas. Só graças a vocês é que tudo isto foi possível, sem todo o vosso apoio, compreensão, conversas, sorrisos, paciência para os fins de semana em que eu chegava sem ela…não teria conseguido! Não foram anos fáceis, mas superámos, vamos superando! Juntos! Que é o que realmente importa! Obrigada por tudo o que tenho aprendido com vocês! Quero também agradecer à Lana por todos os saltos de alegria que animavam qualquer final de dia mais depressivo! Estes seres, valem muito mais do que alguns.

Ao Ricardo, tenho a dizer que o futuro ninguém o sabe, mas esta, é para ti! O que aguentou todas as crises destes anos! Só eu e tu sabemos o que tiveste de aturar! E o apoio que me deste… a esse, tenho o maior obrigado do mundo a dar! Aconteça o que acontecer, o que aconteceu… já ninguém nos tira! Aprendemos que nem tudo (ou quase nada!) sai como planeado! E que não existem momentos perfeitos! Mas, mesmo com medo, o importante é enfrentar e superar! Como temos feito até agora! Obrigada por tudo o que me tens dado!

A todos vós e a toda esta fase, tenho a agradecer todos os ensinamentos além-ciência! Obrigada por me terem ensinado o que realmente importa nesta vida e que não existe nada nem ninguém superior, a não ser o amor! E que só podemos dar importância ao que conseguimos controlar. Obrigada a quem me ensinou o que quero e especialmente o que não quero ser! Obrigada!

— O que é mais importante? O caminho ou o destino?

— A companhia!

List of Publications

Articles published in peer-reviewed international journals that were included in this Doctoral thesis

I. IR780 loaded sulfobetaine methacrylate-functionalized albumin nanoparticles aimed for enhanced breast cancer phototherapy
Cátia G. Alves, Duarte de Melo-Diogo, Rita Lima-Sousa, Ilídio J. Correia
International Journal of Pharmaceutics, 2020, 582: 119346
DOI: 10.1016/j.ijpharm.2020.119346
I.F. = 6.51; Q1 Pharmacology & Pharmacy (40/279)
Citations - ISI Web of Knowledge: 16, Google Scholar: 18, Scopus: 17

II. Poly(2-ethyl-2-oxazoline)-IR780 conjugate nanoparticles for breast cancer phototherapy
Cátia G. Alves, Rita Lima-Sousa, Bruna L. Melo, Paula Ferreira, André F. Moreira, Ilídio J. Correia, Duarte de Melo-Diogo
Nanomedicine, 2023, 17: 2057-2072
DOI: 10.2217/nnm-2022-0218
I.F. = 6.096; Q1 Biotechnology & Applied Microbiology (31/159)
Citations - ISI Web of Knowledge: 0, Google Scholar: 0, Scopus: 0

Articles published in peer-reviewed international journals not included in this Doctoral thesis

I. Hyaluronic acid functionalized nanoparticles loaded with IR780 and DOX for cancer chemo-photothermal therapy
Cátia G. Alves, Duarte de Melo-Diogo, Rita Lima-Sousa, Elisabete C. Costa, Ilídio J. Correia
European Journal of Pharmaceutics and Biopharmaceutics, 2019, 137: 86-94
DOI: 10.1016/j.ejpb.2019.02.016
I.F. = 5.589; Q1 Pharmacology & Pharmacy (60/279)
Citations - ISI Web of Knowledge: 42, Google Scholar: 48, Scopus: 43

II. Graphene Family Nanomaterials for Application in Cancer Combination Photothermal Therapy
Duarte de Melo-Diogo, Rita Lima-Sousa, Cátia G. Alves, Ilídio J. Correia
Biomaterials Science, 2019, 7: 3534
DOI: 10.1039/c9bm00577c
I.F. = 7.59; Q1 Materials Science, Biomaterials (9/44)
Citations - ISI Web of Knowledge: 55, Google Scholar: 67, Scopus: 57

III. Prototypic heptamethine cyanine incorporating nanomaterials for cancer phototheragnostic
Miguel M. Leitão, Duarte de Melo-Diogo, Cátia G. Alves, Rita Lima-Sousa, Ilídio J. Correia
Advanced Healthcare Materials, 2020, 9(6): 1901665
DOI: 10.1002/adhm.201901665
I.F. = 11.092; Q1 Engineering, Biomedical (8/98)
Citations - ISI Web of Knowledge: 40, Google Scholar: 44, Scopus: 40

IV. The importance of spheroids in analyzing nanomedicine efficacy
Inês Mó, Ivo J. Sabino, Duarte de Melo-Diogo, Rita Lima-Sousa, Cátia G. Alves, Ilídio J. Correia
Nanomedicine, 2020, 15(15): 1513-1525
DOI: 10.2217/nnm-2020-0054
I.F. = 6.096; Q1 Biotechnology & Applied Microbiology (31/158)
Citations - ISI Web of Knowledge: 12, Google Scholar: 13, Scopus: 11

V. Injectable *in situ* forming thermo-responsive graphene based hydrogels for cancer chemo-photothermal therapy and NIR light-enhanced antibacterial applications
Rita Lima-Sousa, Duarte de Melo-Diogo, Cátia G. Alves, Cátia S. D. Cabral, Sónia P. Miguel, António G. Mendonça, Ilídio J. Correia
Materials Science and Engineering: C, 2020, 117: 111294
DOI: 10.1016/j.msec.2020.111294
I.F. = 8.457; Q1 Materials Science, Biomaterials (8/44)
Citations - ISI Web of Knowledge: 36, Google Scholar: 48, Scopus: 40

VI. Sulfobetaine methacrylate-functionalized graphene oxide-IR780 nanohybrids aimed at improving breast cancer phototherapy
Miguel M. Leitão, Cátia G. Alves, Duarte de Melo-Diogo, Rita Lima-Sousa, André F. Moreira, Ilídio J. Correia
RSC Advances, 2020, 10: 38621-38630
DOI: 10.1039/D0RA07508F
I.F. = 4.036; Q2 Chemistry, Multidisciplinary (75/179)
Citations - ISI Web of Knowledge: 9, Google Scholar: 10, Scopus: 8

VII. Assessing the Combinatorial Chemo-Photothermal Therapy Mediated by Sulfobetaine Methacrylate-Functionalized Nanoparticles in 2D and 3D *In Vitro* Cancer Models
Inês Mó, Cátia G. Alves, Duarte de Melo-Diogo, Rita Lima-Sousa, Ilídio J. Correia
Biotechnology Journal, 2020, 15: 2000219
DOI: 10.1002/biot.202000219
I.F. = 5.726; Q1 Biochemical Research Methods (13/79)
Citations - ISI Web of Knowledge: 8, Google Scholar: 7, Scopus: 8

VIII. Sulfobetaine methacrylate-albumin-coated graphene oxide incorporating IR780 for enhanced breast cancer phototherapy
Bruna L. Melo, Rita Lima-Sousa, Cátia G. Alves, Paula Ferreira, André F. Moreira, Ilídio J. Correia, Duarte de Melo-Diogo
Nanomedicine, 2021, 16(6): 453-464
DOI: 10.2217/nnm-2020-0460
I.F. = 6.096; Q1 Biotechnology & Applied Microbiology (31/158)
Citations - ISI Web of Knowledge: 3, Google Scholar: 3, Scopus: 3

IX. Injectable *in situ* forming hydrogels incorporating dual-nanoparticles for chemo-photothermal therapy of breast cancer cells
Ivo J. Sabino, Rita Lima-Sousa, Cátia G. Alves, Bruna L. Melo, André F. Moreira, Ilídio J. Correia, Duarte de Melo-Diogo
International Journal of Pharmaceutics, 2021, 600: 120510
DOI: 10.1016/j.ijpharm.2021.120510
I.F. = 6.51; Q1 Pharmacology & Pharmacy (40/279)
Citations - ISI Web of Knowledge: 11, Google Scholar: 11, Scopus: 10

X. Combining Photothermal-Photodynamic Therapy Mediated by Nanomaterials with Immune Checkpoint Blockade for Metastatic Cancer Treatment and Creation of Immune Memory
Rita Lima-Sousa, Bruna L. Melo, Cátia G. Alves, André F. Moreira, António G. Mendonça, Ilídio J. Correia, Duarte de Melo-Diogo
Advanced Functional Materials, 2021, 31: 2010777
DOI: 10.1002/adfm.202010777
I.F. = 19.924; Q1 Chemistry, Multidisciplinary (10/179)
Citations - ISI Web of Knowledge: 7, Google Scholar: 9, Scopus: 7

XI. Mitoxantrone-loaded lipid nanoparticles for breast cancer therapy - Quality-by-design approach and efficacy assessment in 2D and 3D *in vitro* cancer models
Andreia Granja, Rita Lima-Sousa, Cátia G. Alves, Duarte de Melo-Diogo, Marina Pinheiro, Célia T. Sousa, Ilídio J. Correia, Salette Reis
International Journal of Pharmaceutics, 2021, 607: 121044
DOI: 10.1016/j.ijpharm.2021.121044
I.F. = 6.51; Q1 Pharmacology & Pharmacy (40/279)
Citations - ISI Web of Knowledge: 3, Google Scholar: 9, Scopus: 6

XII. Poly(2-ethyl-2-oxazoline) functionalized reduced graphene oxide: Optimization of the reduction process using dopamine and application in cancer photothermal therapy
Rita Lima-Sousa, Cátia G. Alves, Bruna L. Melo, André F. Moreira, António G. Mendonça, Ilídio J. Correia, Duarte de Melo-Diogo
Materials Science and Engineering: C, 2021, 130: 112468
DOI: 10.1016/j.msec.2021.112468
I.F. = 8.457; Q1 Materials Science, Biomaterials (8/44)
Citations - ISI Web of Knowledge: 2, Google Scholar: 2, Scopus: 2

XIII. Heptamethine Cyanine-Loaded Nanomaterials for Cancer Immuno-Photothermal/Photodynamic Therapy: A Review
Cátia G. Alves, Rita Lima-Sousa, Bruna L. Melo, André F. Moreira, Ilídio J. Correia, Duarte de Melo-Diogo
Pharmaceutics, 2022, 14(5): 1015
DOI: 10.3390/pharmaceutics14051015
I.F. = 6.525; Q1 Pharmacology & Pharmacy (39/279)
Citations - ISI Web of Knowledge: 0, Google Scholar: 1, Scopus: 0

XIV. Chitosan-based injectable *in situ* forming hydrogels containing dopamine-reduced graphene oxide and resveratrol for breast cancer chemo-photothermal therapy

Bruna L. Melo, Rita Lima-Sousa, Cátia G. Alves, André F. Moreira, Ilídio J. Correia, Duarte de Melo-Diogo

Biochemical Engineering Journal, 2022, 185: 108529

DOI: 10.1016/j.bej.2022.108529

I.F. = 4.446; Q2 Biotechnology & Applied Microbiology (55/158)

Citations - ISI Web of Knowledge: 0, Google Scholar: 0, Scopus: 0

Book chapter in a peer-reviewed scientific book published by an international publisher not included in this Doctoral thesis

I. Chapter 10 - Inorganic-based drug delivery systems for cancer therapy

Carolina F. Rodrigues, Cátia G. Alves, Rita Lima-Sousa, André F. Moreira, Duarte de Melo-Diogo, Ilídio J. Correia

Advances and Avenues in the Development of Novel Carriers for Bioactives and Biological Agents, Edited by Manju Rawat Singh, Deependra Singh, Jagat R. Kanwar, Nagendra Singh Chauhan

Published by Academic Press, 2020, 286-316

DOI: 10.1016/B978-0-12-819666-3.00010-9

Citations - Google Scholar: 5, Scopus: 5

List of Scientific Communications

Oral presentations

I. Cátia G. Alves, *Development of IR780 based nanomaterials for cancer therapy*, V Encontro Científico NEQ/AAC, Universidade de Coimbra, February 19th, 2020, Coimbra, Portugal.

II. Bruna L. Melo, Rita Lima-Sousa, Cátia G. Alves, Paula Ferreira, André F. Moreira, Ilídio J. Correia, Duarte de Melo-Diogo, *Graphene Oxide functionalized with Sulfobetaine methacrylate-albumin and loaded with IR780 for improved breast cancer photothermal therapy,* XVI Annual CICS-UBI Symposium, Centro de Investigação em Ciências da Saúde, September 30th, 2021, Covilhã, Portugal.

Poster presentations

I. Cátia G. Alves, Duarte de Melo-Diogo, Rita Lima-Sousa, Elisabete C. Costa, Ilídio J. Correia, *IR780 and DOX Loaded Hyaluronic Acid-based Micelles for Targeted Cancer Chemo-Phototherapy*, 6th IEEE Portuguese Meeting on Bioengineering (ENBENG 2019), February 22nd, 2019, Lisboa, Portugal.

II. Rita Lima-Sousa, Duarte de Melo-Diogo, Cátia G. Alves, Elisabete C. Costa, Ricardo O. Louro, Ilídio J. Correia, *Targeted cancer photothermal therapy using hyaluronic acid functionalized green reduced graphene oxide*, 6th IEEE Portuguese Meeting on Bioengineering (ENBENG 2019), February 22nd, 2019, Lisboa, Portugal.

III. Rita Lima-Sousa, Duarte de Melo-Diogo, Cátia G. Alves, Elisabete C. Costa, Paula Ferreira, Ricardo O. Louro, António G. Mendonça, Ilídio J. Correia, *Breast Cancer Targeted Photothermal Therapy Mediated By Hyaluronic Acid Functionalized Reduced Graphene Oxide*, XIV Annual CICS-UBI Symposium, July 4th, 2019, Covilhã, Portugal.

IV. Cátia G. Alves, Duarte de Melo-Diogo, Rita Lima-Sousa, Elisabete C. Costa, Ilídio J. Correia, *Co-encapsulation of IR780 and DOX in Hyaluronic Acid Functionalized Micelles for Targeted Cancer Chemo-phototherapy*, XIV Annual CICS-UBI Symposium, July 4th, 2019, Covilhã, Portugal.

V. Rita Lima-Sousa, Duarte de Melo-Diogo, Cátia G. Alves, Elisabete C. Costa, Paula Ferreira, Ricardo O. Louro, António G. Mendonça, Ilídio J. Correia, *Hyaluronic acid functionalized reduced graphene oxide nanomaterials for targeted cancer photothermal therapy*, Encontro com a Ciência e Tecnologia em Portugal 2019, July 8th, 2019, Lisboa, Portugal.

VI. Cátia G. Alves, Duarte de Melo-Diogo, Rita Lima-Sousa, Elisabete C. Costa, Ilídio J. Correia, *Hyaluronic Acid-based Micelles loaded with IR780 and DOX for Targeted Cancer Chemo-Photothermal Therapy*, Encontro com a Ciência e Tecnologia em Portugal 2019, July 8th, 2019, Lisboa, Portugal.

VII. Rita Lima-Sousa, Duarte de Melo-Diogo, Cátia G. Alves, Elisabete C. Costa, Paula Ferreira, Ricardo O. Louro, António G. Mendonça, Ilídio J. Correia, *Environmentally-friendly reduced graphene oxide functionalized with hyaluronic acid for targeted cancer photothermal therapy*, 5th Edition of the European Graphene Forum - EGF, October 23rd, 2019, Lisboa, Portugal.

VIII. Duarte de Melo-Diogo, Elisabete C. Costa, Cátia G. Alves, Rita Lima-Sousa, Paula Ferreira, Ricardo O. Louro, Ilídio J. Correia, *POxylated Graphene Oxide for cancer phototherapy and combinatorial drug delivery*, 5th Edition of the European Graphene Forum - EGF, October 23rd, 2019, Lisboa, Portugal.

IX. Cátia G. Alves, Duarte de Melo-Diogo, Rita Lima-Sousa, Ilídio J. Correia, *Sulfobetaine methacrylate-albumin nanoparticles loaded with IR780 for breast cancer therapy*, XV Annual CICS-UBI Symposium, October 1st, 2020, Covilhã, Portugal.

X. Rita Lima-Sousa, Duarte de Melo-Diogo, Cátia G. Alves, Cátia S. D. Cabral, Sónia P. Miguel, António G. Mendonça, Ilídio J. Correia, *Graphene-based injectable in situ forming hydrogels for cancer combinatorial therapy*, XV Annual CICS-UBI Symposium, October 1st, 2020, Covilhã, Portugal.

XI. Cátia G. Alves, Duarte de Melo-Diogo, Rita Lima-Sousa, Ilídio J. Correia, *IR780 loaded Sulfobetaine Methacrylate-Albumin Nanoparticles for Breast Cancer Photothermal Therapy*, Encontro com a Ciência e Tecnologia em Portugal 2021, June 28th, 2021, Lisboa, Portugal.

XII. Bruna L. Melo, Rita Lima-Sousa, Cátia G. Alves, Paula Ferreira, André F. Moreira, Ilídio J. Correia, Duarte de Melo-Diogo, *IR780 loaded and Sulfobetaine methacrylate-albumin-coated Graphene Oxide for improved breast cancer photothermal therapy*, Encontro com a Ciência e Tecnologia em Portugal 2021, June 28th, 2021, Lisboa, Portugal.

XIII. Rita Lima-Sousa, Duarte de Melo-Diogo, Cátia G. Alves, Cátia S. D. Cabral, Sónia P. Miguel, António G. Mendonça, Ilídio J. Correia, *Injectable thermo-responsive hydrogel incorporating graphene-based nanomaterials and a dual drug combination for breast cancer chemo-photothermal therapy*, Encontro com a Ciência e Tecnologia em Portugal 2021, June 28th, 2021, Lisboa, Portugal.

XIV. Rita Lima-Sousa, Teresa Cernadas, Duarte de Melo-Diogo, Cátia G. Alves, Elisabete C. Costa, Paula Ferreira, Ricardo O. Louro, António G. Mendonça, Ilídio J. Correia, *Environmentally-friendly reduction of graphene oxide for future application in cancer photothermal therapy*, 2nd International Conference on Chemical Engineering and Catalysis (ICCEC-2021), November 16th, 2021, Miami, USA.

Conference Organizing Committees

Member of the organizing committee of scientific conferences

I. III International Congress in Health Sciences Research towards innovation and entrepreneurship: Trends in Aging and Cancer, Universidade da Beira Interior, November 14th to 16th, 2019, Covilhã, Portugal

Resumo

Apesar de todo o trabalho de investigação que tem sido desenvolvido, o cancro continua a ser uma das doenças mais comuns e uma das mais mortíferas em todo o mundo. Num estadio inicial, a remoção cirúrgica do tumor é a abordagem mais aplicada no tratamento deste. Em fases mais avançadas da doença, a quimioterapia e a radioterapia são as terapêuticas mais usadas. No entanto, estes tratamentos apresentam baixa eficácia e induzem toxicidade sistémica, causando diversos efeitos secundários no paciente, tais como perda de cabelo, náuseas, vómitos e fadiga. Estas limitações das terapêuticas utilizadas em meio clínico fazem com que exista uma necessidade urgente em desenvolver novas terapias anticancerígenas caracterizadas por uma maior eficácia e segurança.

Neste contexto, nos últimos anos, as fototerapias mediadas por nanomateriais têm vindo a mostrar resultados muito promissores. Neste tipo de abordagem terapêutica é importante ter em consideração dois aspetos: i) as propriedades físico-químicas dos nanomateriais (por exemplo, tamanho, composição de superfície), e ii) as propriedades óticas do laser (por exemplo, comprimento de onda, intensidade) e do agente fototerapêutico (por exemplo, coeficiente de extinção molar, eficiência fototérmica e dinâmica).

O tamanho, a carga, a forma e a composição do revestimento (corona) das nanopartículas são fatores que influenciam a sua capacidade para atingirem o ambiente tumoral. Por norma, a otimização do tamanho dos nanomateriais é um dos parâmetros mais estudados, de modo a aumentar a sua acumulação no tumor através do efeito de permeabilização e retenção aumentados (do inglês: *Enhanced Permeability and Retention effect*). No entanto, recentemente foi descrito um fenómeno que ocorre espontaneamente na vasculatura do tumor denominado por “erupções dinâmicas”. Estas erupções espontâneas facilitam o extravasamento das nanopartículas para o local do tumor. Este novo fenómeno conduziu a uma mudança de paradigma, e atualmente os investigadores estão focados na otimização do revestimento das nanopartículas. O objetivo passa por aumentar o tempo de circulação dos nanomateriais na corrente sanguínea, incrementando assim a probabilidade destes de beneficiarem das erupções dinâmicas, promovendo assim a sua acumulação na zona tumoral.

De modo a melhorar o tempo de circulação sanguínea dos nanomateriais e aumentar a sua acumulação no tumor, estes nanossistemas têm sido revestidos com Polietileno glicol

(PEG). Contudo, recentemente foi descrito que os nanomateriais "PEGuilados" sofrem do fenómeno de eliminação acelerada do sangue (do inglês *Accelerated Blood Clearance*). Logo após a primeira administração dos nanomateriais "PEGuilados" são criados anticorpos anti-PEG. Assim, estes anticorpos vão mediar a rápida eliminação das nanopartículas nas administrações seguintes. Devido à imunogenicidade apresentada por algumas nanoestruturas "PEGuiladas", torna-se crucial desenvolver/avaliar a capacidade de novos revestimentos em melhorar as propriedades biológicas dos nanomateriais.

A eficácia das fototerapias mediadas por nanomateriais depende também das propriedades óticas do laser e do agente foto-responsivo. De facto, a utilização de luz na região do infravermelho próximo (NIR; 750-1000 nm) é de extrema importância, uma vez que esta radiação não interage com os componentes biológicos, tais como a água, a melanina ou o colagénio e ainda apresenta a capacidade de penetrar profundamente nos tecidos (até cerca de 2 cm). Para além disto, a intensidade da luz emitida pelo laser e o tempo de irradiação podem também afetar a performance terapêutica. Desta forma, as fototerapias baseadas em nanomateriais que são responsivos à luz NIR têm-se demonstrado muito promissoras. Após a acumulação dos nanomateriais no tumor, esta zona é irradiada com luz NIR, levando à produção de um aumento de temperatura (terapia fototérmica) e/ou de espécies reativas de oxigénio (terapia fotodinâmica), culminando em danos nas células cancerígenas.

De entre os diversos agentes responsivos à luz NIR, o IR780 destaca-se devido à sua elevada polivalência. Esta pequena molécula apresenta a capacidade de ser usada tanto para terapia fototérmica como para terapia fotodinâmica e, para além disto, ainda apresenta capacidade de ser utilizada em imagiologia, uma vez que emite fluorescência. No entanto, esta heptametina cianina apresenta toxicidade aguda e ainda baixa solubilidade em água, o que impede a sua aplicação direta na terapia do cancro. A encapsulação de IR780 em nanopartículas pode permitir ultrapassar estas desvantagens. Porém, a maioria dos nanomateriais que incorporam IR780 têm sido produzidos usando PEG no seu revestimento. Tendo em conta os estudos recentes que demonstram a imunogenicidade das nanoestruturas "PEGuiladas", é de extrema importância desenvolver novos nanomateriais contendo IR780 que sejam desprovidos de qualquer revestimento à base de PEG.

Assim, o desenvolvimento do plano de trabalhos proposto neste doutoramento teve como principal objetivo validar o potencial de novos materiais à base de metacrilato de sulfobetaína (do inglês: *sulfobetaine methacrylate*, SBMA) e de poli(2-etil-2-oxazolina)

(do inglês: *Poly(2-ethyl-2-oxazoline)*, PEtOx), no revestimento de nanoestruturas contendo IR780 para aplicação na terapia fototérmica do cancro.

Nesta tese são apresentados dois capítulos com trabalho de investigação. No primeiro trabalho de investigação (Capítulo 3), a albumina de soro bovino (do inglês: *Bovine Serum Albumin*, BSA) foi enxertada com SBMA. Este novo polímero anfifílico foi posteriormente combinado com IR780 através da técnica de nanoprecipitação de forma a obterem-se nanopartículas (IR/SBMA-BSA NPs). As nanopartículas produzidas apresentaram um tamanho (≈ 96 nm) e uma carga de superfície (≈ -9 mV) adequados para serem aplicadas na terapia do cancro. A funcionalização de superfície das nanopartículas com SBMA revelou ser bastante importante uma vez que aumentou a estabilidade coloidal em diferentes meios, bem como a sua internalização em células do cancro da mama. Nestas mesmas células, a ação combinada das IR/SBMA-BSA NPs com a luz NIR conseguiu diminuir a viabilidade celular para apenas 12 %.

No segundo trabalho de investigação (Capítulo 4), procedeu-se à preparação de um conjugado de IR780, tendo para tal ligado quimicamente esta molécula ao PEtOx. Este novo conjugado PEtOx-IR780 foi posteriormente combinado com succinato de D-α-tocoferol (TOS) através da técnica de nanoprecipitação, obtendo-se a nanoformulação denominada por PEtOx-IR/TOS NPs. Estas nanopartículas apresentaram um tamanho (≈ 190 nm) e uma carga de superfície (≈ -8 mV) que são compatíveis com aplicações anticancerígenas. As PEtOx-IR/TOS NPs revelaram uma estabilidade coloidal ótima bem como capacidade para serem internalizadas pelas células cancerígenas. Os resultados obtidos demonstraram que a combinação de PEtOx-IR/TOS NPs com luz NIR consegue diminuir a viabilidade de células do cancro da mama (modelos 2D de cultura celular *in vitro*) para 9 %, e nos esferóides heterotípicos de cancro da mama (modelos 3D de cultura celular *in vitro*) a viabilidade diminuiu para apenas 15 %.

Os resultados apresentados nesta tese revelam que os novos nanomateriais à base de IR780 produzidos têm potencial para aplicação em terapia fototérmica do cancro da mama.

Palavras-chave

Cancro;IR780;Terapia Fototérmica;Alternativas ao PEG;Infravermelho Próximo

Abstract

Despite all the efforts that have been done, cancer remains as one of the most common and deadliest diseases in the whole world. Surgery can be an effective strategy to treat this disease if the cancer is diagnosed at an early stage. In a more advanced stage of this disease, chemotherapy and radiotherapy are the most applied therapeutic strategies. However, these conventional approaches lack efficacy and selectivity towards cancer cells, causing several side effects in the patients such as hair loss, nausea, and severe weakness. These drawbacks of the clinically available therapeutics highlight the urgent need for developing new anticancer approaches with greater efficacy and safety.

To face this challenge, the nanomaterials' mediated phototherapy is one of the most promising strategies. Regarding this therapeutic modality, it is important to consider two main aspects: i) the physicochemical properties of the nanomaterials (*e.g.*, size, corona composition) and ii) the optical properties of the laser (*e.g.*, wavelength, intensity) and of the therapeutic agent (*e.g.*, molar extinction coefficient, photothermal and photodynamic efficiencies).

In what concerns the first point, the nanomaterials' size, charge, shape, and corona composition play an important role in their ability to reach the tumor site. Classically, the optimization of the nanomaterials' size has been intensively pursued to allow these nanostructures to accumulate at the tumor site by exploiting the tumor's leaky vasculature (*i.e.*, to take advantage from the so-called Enhanced Permeability and Retention effect). However, recently it was unveiled that dynamic vents (also known as eruptions) occur spontaneously at the tumor vasculature, facilitating nanostructures extravasation into the tumor site. This new phenomenon led to a paradigm shift, and thus, currently, researchers are focused on the optimization of the nanoparticles' corona for improving their tumor uptake (*i.e.*, to increase their blood circulation time and hence their likelihood to benefit from these dynamic vents).

To improve the nanostructures' blood circulation time and favor their tumor uptake, these nano-systems have been mainly coated with poly(ethylene glycol) (PEG). However, recently it was uncovered that PEGylated nanomaterials suffer from the Accelerated Blood Clearance phenomenon. Therefore, at the time of the first administration of PEGylated nanomaterials, anti-PEG antibodies are created. Then, these anti-PEG antibodies mediate the rapid clearance of the PEGylated nanoparticles in subsequent administrations. Due to the immunogenicity displayed by PEG-based coatings, it is

crucial to develop and validate novel materials capable of improving the nanostructures' biological properties.

The efficacy of nanomaterials-based phototherapies also depends on the optical properties of the laser and of the photoresponsive agent. In this regard, the use of near infrared (NIR; 750-1000 nm) light is of utmost importance since it does not interact significantly with major body components (*e.g.*, water, melanin, collagen) and achieves a high penetration depth (up to about 2 cm). Moreover, the laser power density and irradiation time can also affect the therapeutic outcome. In this way, phototherapies based on NIR light-responsive nanomaterials have been showing promising results. In this type of therapy, after the nanomaterials' tumor uptake, this zone is irradiated with NIR light. Upon interaction with this radiation, the nanomaterials can produce a temperature increase (photothermal therapy) and/or reactive oxygen species (photodynamic therapy), which cause damages on cancer cells.

Among the several NIR light responsive agents, IR780 stands out due to its high versatility. This prototypic heptamethine cyanine has multimodal properties since it can be used for both photothermal therapy and photodynamic therapy as well as for imaging applications (IR780 emits fluorescence in the NIR). However, this small molecule presents acute toxicity and low solubility, hindering its direct application in cancer therapy. In this way, encapsulating IR780 in nanomaterials can be pursued to surpass these disadvantages. However, most of the IR780-based nanomaterials have been produced using PEG in their corona. Considering the recent studies demonstrating the immunogenicity of PEGylated nanostructures, it is of utmost importance to develop new IR780-based nanoparticles that are functionalized with PEG alternatives.

In this way, the main goal of the workplan developed during this Doctoral thesis was to validate the potential of novel materials, based on sulfobetaine methacrylate (SBMA) and Poly(2-ethyl-2-oxazoline) (PEtOx), in the coating of nanostructures incorporating IR780 for application in cancer photothermal therapy.

This thesis includes two chapters presenting research work. In the first research work (Chapter 3), Bovine Serum Albumin (BSA) was grafted with SBMA, for the first time, being this polymer (SBMA-BSA) employed to encapsulate IR780 through the nanoprecipitation technique (IR/SBMA-BSA NPs). The produced nanoparticles presented an ideal size (≈ 96 nm) and surface charge (≈ -9 mV) for cancer-related applications. As importantly, the SBMA functionalization improved the colloidal stability of the nanostructures in different media as well as their uptake by breast cancer cells. In

the phototherapeutic assays, the IR/SBMA-BSA NPs in combination with NIR light could decrease the cancer cells' viability to just 12 %.

In the second research work (Chapter 4), a novel amphiphilic PEtOx-IR780 conjugate was produced. For that, the cyclohexenyl ring of IR780 was chemically attached to thiol-terminated PEtOx (PEtOx-IR conjugate). Afterwards, PEtOx-IR and D-α-tocopheryl succinate (TOS) were combined through the nanoprecipitation technique, yielding PEtOx-IR/TOS NPs. These nanoparticles presented a size (≈ 190 nm) and surface charge (≈ -8 mV) compatible with anticancer applications. As importantly, the PEtOx-IR/TOS NPs also presented an optimal colloidal stability. The PEtOx-IR/TOS NPs could be successfully internalized by cancer cells. In the phototherapeutic assays, the combination of PEtOx-IR/TOS NPs with NIR light could decrease the viability of breast cancer cells (2D *in vitro* cancer models) to 9 %, and the heterotypic breast cancer spheroids' (3D *in vitro* cancer models) viability was also reduced to just 15 %.

Overall, the results obtained in this thesis validate the potential of SBMA-brushes and PEtOx in the coating of IR780-based nanomaterials. Moreover, these novel IR780-based nanomaterials also displayed a good *in vitro* performance, highlighting their potential for cancer photothermal therapy.

Keywords

Cancer, IR780, Photothermal Therapy, PEG-alternatives, Near Infrared

Thesis Overview

This thesis is organized in 5 chapters.

The **first chapter** includes the **global aims** of the work performed during the PhD thesis period. The **second chapter** comprises the **introductory section**, in which the parameters that influence the nanomaterials' phototherapeutic potential are overviewed, with a focus on the nanostructures' physicochemical and optical properties as well as on the laser parameters used to irradiate the nanomaterials.

The third and fourth chapters present the practical works developed during this PhD thesis. **Chapter three** is entitled "IR780 loaded sulfobetaine methacrylate-functionalized albumin nanoparticles aimed for enhanced breast cancer phototherapy" (**research work 1**). In this research work, Bovine Serum Albumin (BSA) was grafted with sulfobetaine methacrylate (SBMA), being this novel polymer employed to prepare IR780 loaded nanomaterials (termed as IR/SBMA-BSA NPs). Afterwards, the physicochemical, optical, and biological properties of the IR/SBMA-BSA NPs were investigated.

Chapter four is named "Poly(2-ethyl-2-oxazoline)-IR780 conjugate nanoparticles for breast cancer phototherapy" (**research work 2**). In this research work, a novel amphiphilic PEtOx-IR780 conjugate was produced and combined with D-α-tocopheryl succinate (TOS) to obtain nanostructures (termed as PEtOx-IR/TOS NPs). The physicochemical and optical features of the PEtOx-IR/TOS NPs were characterized as well as their biological performance in 2D and 3D *in vitro* cancer models.

Finally, the **fifth chapter** comprises the **conclusions** of the research works performed during this thesis, as well as the **future perspectives** related to these research topics.

Index

List of Figures

Abbreviation List

^{1}H NMR	Proton Nuclear Magnetic Resonance
ABC	Accelerated Blood Clearance
ANOVA	Analysis of Variance
BSA	Bovine Serum Albumin
CLSM	Confocal Laser Scanning Microscopy
cRGD	Cyclic Arginine-Glycine-Aspartic Acid
CTAB	Hexadecyltrimethylammonium Bromide
CuS	Copper Sulfide
DLS	Dynamic Light Scattering
DMEM-F12	Dulbecco's Modified Eagle's Medium-F12
DOX	Doxorubicin
DTT	DL-Dithiothreitol
EE	Encapsulation Efficiency
EMA	European Medicines Agency
EPR	Enhanced Permeability and Retention
FBS	Fetal Bovine Serum
FDA	Food and Drug Administration
FTIR	Fourier Transform Infrared Spectroscopy
GO	Graphene Oxide
HA	Hyaluronic Acid
ICG	Indocyanine Green
IR780	2-[2-[2-Chloro-3-[(1,3-dihydro-3,3-dimethyl-1-propyl-2*H*-indol-2-ylidene)ethylidene]-1-cyclohexen-1-yl]ethenyl]-3,3-dimethyl-1-propylindolium iodide
IR783	2-[2-[2-Chloro-3-[2-[1,3-dihydro-3,3-dimethyl-1-(4-sulfobutyl)-2*H*-indol-2-ylidene]-ethylidene]-1-cyclohexen-1-yl]-ethenyl]-3,3-dimethyl-1-(4-sulfobutyl)-3*H*-indolium hydroxide
IR820	2-[2-[2-Chloro-3-[[1,3-dihydro-1,1-dimethyl-3-(4-sulfobutyl)-2*H*-benzo[e]indol-2-ylidene]-ethylidene]-1-cyclohexen-1-yl]-ethenyl]-1,1-dimethyl-3-(4-sulfobutyl)-1*H*-benzo[e]indolium hydroxide

IR/BSA NPs	IR780 loaded BSA nanoparticles
IR/SBMA-BSA NPs	IR780 loaded SBMA-*g*-BSA nanoparticles
MCF-7	Michigan Cancer Foundation-7
NHDF	Normal Human Dermal Fibroblasts
NIR	Near Infrared
ns	Non-significant
PBS	Phosphate Buffered Saline
PDA	Polydopamine
PDI	Polydispersity Index
PDT	Photodynamic Therapy
PEDOT	Poly(3,4-ethylenedioxythiophene)
PEG	Poly(ethylene glycol)
PEtOx-SH	Poly(2-ethyl-2-oxazoline) α-benzyl ω-thiol terminated
PEtOx-IR conjugate	PEtOx-IR780 conjugate
PEtOx-IR NPs	PEtOx-IR Nanoparticles
PEtOx-IR/TOS NPs	TOS-incorporating PEtOx-IR NPs
PI	Propidium Iodide
PLGA	Poly(lactic-*co*-glycolic acid)
PPy	Polypyrrole
PTT	Photothermal Therapy
RES	Reticuloendothelial System
rGO	Reduced GO
SBMA	[2-(methacryloyloxy)ethyl]dimethyl-(3-sulfopropyl)ammonium hydroxide
SBMA-*g*-BSA	BSA grafted with SBMA
S.D.	Standard Deviation
TEM	Transmission Electron Microscopy
TMDCs	Transition Metal Dichalcogenides
TOS	D-α-tocopheryl succinate

Chapter 1: Global Aims

Global Aims

The application of poly(ethylene glycol) (PEG)-based coatings on the nanostructures' surface has been the main strategy pursued to improve their biological properties. However, recent studies have exposed that PEG-based coatings can be immunogenic, triggering the Accelerated Blood Clearance phenomenon. In this way, there is an urgent necessity to develop and validate alternative coatings to functionalize nanoparticles, including those intended for cancer photothermal therapy.

In this way, the global aim of this PhD thesis was to evaluate the potential of novel materials (*i.e.*, PEG alternatives) in the coating of nanostructures incorporating IR780 (2 - [2 - [2 - Chloro - 3 - [(1,3 - dihydro - 3,3 - dimethyl - 1 - propyl - 2*H* - indol - 2 - ylidene)ethylidene] - 1- cyclohexen-1-yl]ethenyl]-3,3-dimethyl-1-propylindolium iodide) aimed for cancer photothermal therapy.

The specific aims of this thesis were:

- Evaluate the potential of sulfobetaine methacrylate (SBMA)- and Poly(2-ethyl-2-oxazoline) (PEtOx)-functionalization in the improvement of IR780-based nanomaterials' colloidal stability and cellular uptake;

- Evaluate the photothermal therapeutic capacity of the produced IR780-based nanoparticles towards breast cancer cells (2D *in vitro* tumor model) and heterotypic breast cancer spheroids (3D *in vitro* tumor model).

Chapter 2: Introduction

2.1. Overview of nanomaterials-based cancer therapy

Cancer remains as one of the most diagnosed and deadliest diseases in the world. According to the statistics of the American Cancer Society, more than 1.9 million new cases will be diagnosed just in the United States in 2022, which will lead to around 609 thousand deaths [1]. In 2020, Europe counted for about 23 % of all cancer cases as well as 20 % of all the cancer deaths [2]. In the particular case of Southern Europe, the cancer mortality in males and females was 126.9 and 76.3 per 100 000 habitants, respectively [2].

Despite the intense research on this topic, the pool of clinically available treatments for this disease has not increased significantly over the years. Surgery can only be applied in early diagnosed cases [3]. In turn, chemotherapy and radiotherapy have multiple drawbacks since these have a low efficacy and induce severe side effects by acting on both cancer and healthy cells [4, 5]. In fact, most patients in these regimens suffer from nausea, hair loss, and infections [4, 5]. In the past years, cancer immunotherapy received a great attention. However, after the initial enthusiasm, it was observed that not every patient is responsive to this approach and that autoimmune side effects are also common [6, 7]. In this way, there is an ever-growing need to develop and implement more effective and selective anticancer approaches.

Recently, phototherapies based on nanomaterials started to gather a lot of interest for cancer therapy [8, 9]. This approach explores the physicochemical properties of the nanomaterials that can drive their tumor accumulation as well as the optical properties of the laser and of the nanostructures, which influence the photoinduced effects. In this regard, researchers have been fine-tuning the nanostructures' size, surface charge, corona composition, and targeting ligand decoration in order to promote their tumor accumulation [10, 11]. Classically, the optimization of the nanomaterials' size has been considered the most important parameter since it would enable the nanostructures' tumor accumulation through the enhanced permeability and retention (EPR) effect [12, 13]. This effect is a consequence of two features of *in vivo* solid tumors: **i)** the tumor's leaky vasculature with fenestrae ranging from 200 - 1200 nm, and **ii)** the tumor zone's impaired lymphatic drainage [14]. By exploiting the EPR effect, nanomaterials with a well-defined size can potentially become accumulated and retained at the tumor site [15]. Recently, another phenomenon that can drive nanoparticles' tumor accumulation was unveiled. It consists of eruptions that occur spontaneously in the tumor-associated blood

vessels (also known as dynamic vents) and that allow the extravasation of large nanoparticle doses into the tumor site [16]. In this way, it is also crucial to optimize the nanostructures' corona to improve their blood circulation time, and hence the likelihood for them to benefit from these dynamic eruptions [16-18].

After the nanostructures' tumor accumulation, this zone is irradiated with laser light. At this stage, the optical properties of the laser light have a decisive role in the possible therapeutic outcome. In this regard, the use of near infrared (NIR) light (750-1000 nm) to irradiate the nanostructures is crucial since this radiation is characterized by having a weak interaction with biological components and a high penetration depth (up to 2 cm) [19]. Furthermore, it is also possible to fine-tune the laser power density (intensity), irradiation time, and on-set of the laser exposure to attain a greater therapeutic outcome [20, 21]. In this way, to be successfully applied in cancer phototherapy, nanomaterials should have a high NIR absorption [19]. Depending on the nanostructures' optical properties, the absorbed NIR light can be converted into heat (photothermal therapy (PTT)), reactive oxygen species (ROS; photodynamic therapy (PDT)), and/or fluorescence (imaging applications) - **Figure 2.1** [22]. The photoinduced heat and ROS can cause damage to cancer cells [23]. In this regard, a final temperature increase to 41 - 45 °C can cause reversible damage to cancer cells by inhibiting DNA replication and repair mechanisms, increasing metabolic stress, and sensitizing cells to the action of other therapeutic agents [10, 24]. On the other hand, when the final temperature attained is above 50 °C, irreversible damages are achieved (dysfunction of the mitochondria, protein denaturation, necrosis) [24]. In turn, the photoinduced ROS can also damage cancer cells by DNA fragmentation, and oxidative stress, among others, which can lead to apoptosis, autophagy, and necrosis [25, 26].

Moreover, the nanostructures' photothermal conversion efficiency and singlet oxygen quantum yields are also important features. Therefore, over the years, several types of nanomaterials with a high NIR absorption were developed (*e.g.,* reduced graphene oxide, nanoparticles loaded with IR780 (2-[2-[2 -Chloro -3-[(1,3 -dihydro-3,3-dimethyl- 1-propyl- 2*H*- indol-2- ylidene)ethylidene]-1-cyclohexen-1-yl]ethenyl]-3,3-dimethyl-1-propylindolium iodide), gold nanomaterials, copper sulfide (CuS) nanoparticles) [22, 27, 28].

In this way, the nanomaterials' mediated PTT/PDT holds a great potential to perform a spatio-temporal controlled anticancer effect [29, 30]. Such ability is strongly influenced by two big factors: the nanostructures' physicochemical properties that drive their tumor

uptake (described in section 2.2), and the laser's and nanostructures' optical properties (discussed in section 2.3) that strongly influence the attained phototherapeutic effects.

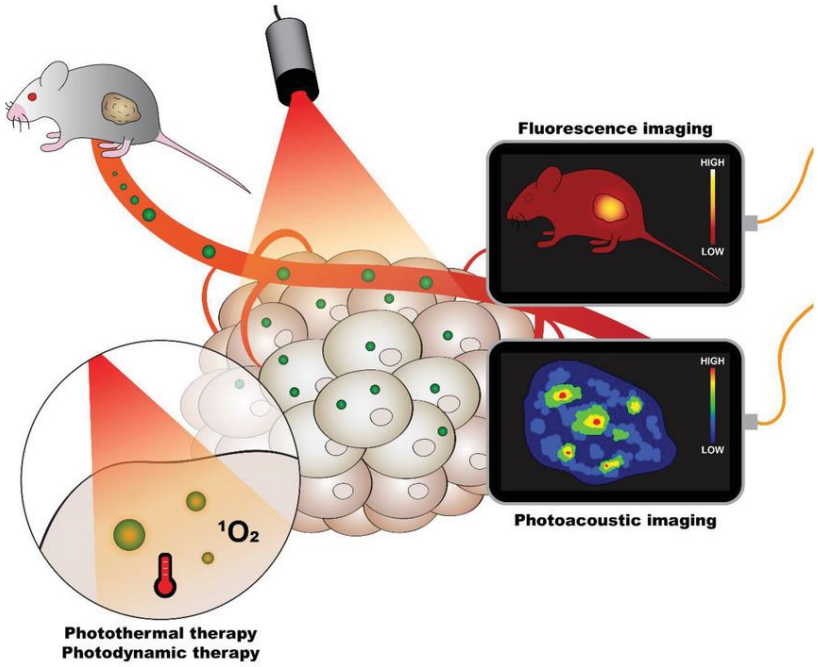

Figure 2.1. Schematic representation of the different therapeutic and imaging modalities that NIR light responsive nanomaterials can perform. Reprinted with permission from [22]. Copyright 2020 Wiley.

2.2. Factors influencing the nanoparticles' tumor accumulation

After intravenous administration of nanoparticles (the most common administration route), these need to surpass several barriers before reaching the tumor zone and become internalized in cancer cells [10]. Initially, during blood circulation, nanoparticles must avoid rapid opsonization and clearance by the immune system [31, 32]. The goal is for the nanoparticles to display a long blood circulation time to increase their probability to extravasate into the tumor tissue by exploiting the EPR effect and the dynamic bursts phenomenon [16, 33, 34]. Then, tumor penetration of nanoparticles has to be achieved and subsequent internalization by the cancer cells. Attaining such milestones is mainly influenced by specific nanoparticles' features such as their size, charge, shape, corona, and the presence of targeting ligands (described in detail in the next subsections). Understanding and modulating these kinetics is crucial to increase the dose of nanoparticles that reaches the tumor, and thus maximize the therapeutic capacity of the nanoparticles (the PTT and PDT generated by the nanoparticles upon NIR laser irradiation are influenced by their concentration at the target site) [35].

2.2.1. Size

The size of the nanoparticles can influence every stage from their intravenous administration up to their internalization in cancer cells [36]. Regarding this parameter, it is particularly important to consider the size of the fenestrae of the tumor vasculature: 200 - 1200 nm [10, 37]. On the other hand, the body's elimination processes are also important. Nanoparticles smaller than 5 nm are easily filtrated by the kidneys [10]. Those with a size lower than 50 nm are easily accumulated in the liver [10]. Moreover, nanoparticles larger than 200 nm can be easily accumulated in the liver and in the spleen [38]. In this way, the ideal nanoparticles size for an improved tumor uptake through the EPR effect, and consequent enhanced therapeutic outcome, is often described as between 100 and 200 nm [10, 39].

Despite these general guidelines, each nanoparticle needs to be evaluated individually in order to analyze which size is the most appropriate for the aimed therapeutic application. For example, Yang *et al*. produced PEGylated gold nanorods with different sizes (the values mentioned are relative to the length of the nanorod) [36]. The nanorods with 70 nm presented a great tumor accumulation (6.74 ID % g^{-1}, after 12 h) than their equivalents with 97, 87, or 60 nm (4.82, 5.47 and 6.19 ID % g^{-1}, respectively). In another work, Zhao *et al*. synthesized polymer-lipidic nanoparticles encapsulating Indocyanine green (ICG) with 39, 68, and 116 nm of size [40]. The nanoparticles with a size of 68 nm showed the highest tumor accumulation and consequently prompted the best therapeutic outcome after NIR irradiation (tumor eradication, while the others only cause tumor growth reduction) (**Figure 2.2**).

2.2.2. Charge

The surface charge of the nanoparticles can influence their blood circulation time, tumor penetration, and cellular internalization [41]. In the literature, the ideal nanoparticles' charge, for cancer PTT/PDT, is within the so-called neutral window, which is considered to be between -10 and +10 mV [10]. This range is defined as optimal since highly negatively or highly positively charged nanomaterials can easily suffer uptake by the reticuloendothelial system (RES) cells and/or be opsonized by serum proteins, impairing their capacity to reach the tumor site [42].

The charge also influences the nanoparticles' interaction with the tumor's extracellular matrix, hence interfering with the nanoparticles' penetration capacity. The tumor's extracellular matrix contains hyaluronic acid (HA) and collagen which are negatively and

positively charged, respectively. In this way, highly charged nanoparticles have a greater probability to interact with these molecules, which is not desirable [42].

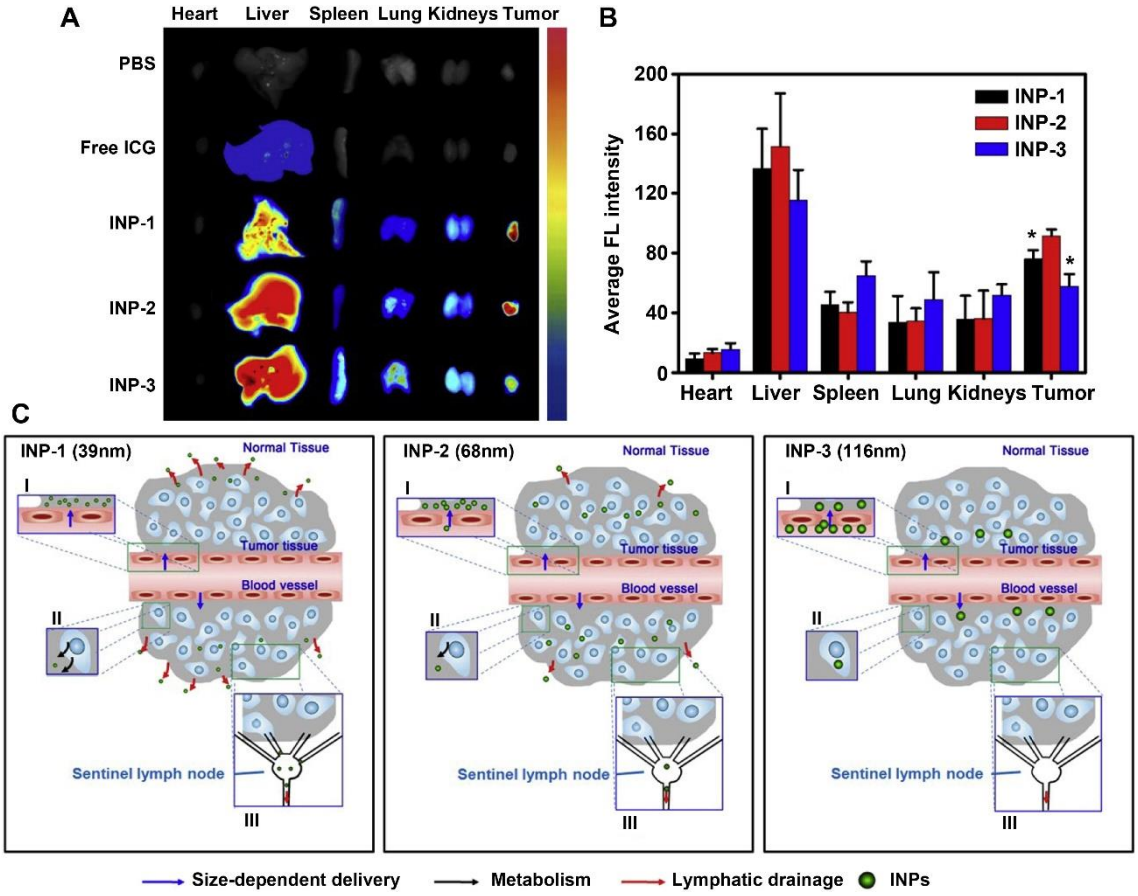

Figure 2.2. Biodistribution of polymer-lipidic nanoparticles encapsulating ICG (INPs) with different sizes after intravenous administration in mice. (A) Fluorescence images of the major organs after 24 h of the injection. (B) Fluorescence (FL) intensity in each major organ after 24 h of nanoparticles administration. $^{*}p < 0.05$ (compared with INP-2). (C) Schematic representation of the factors influencing the tumor accumulation of the INPs. PBS: Phosphate Buffered Saline; INP-1: INPs with a size of 39 nm; INP-2: INPs with a size of 68 nm; INP-3: INPs with a size of 116 nm. Reprinted with permission from [40]. Copyright 2014 Elsevier.

In turn, positively charged nanomaterials are more likely to be internalized by cancer cells due to their interaction with the negative components of the cells' membranes such as sialic acid and phosphatidylserine [43]. Shen *et al.* produced similar nanoparticles with different surface charges (-11.7, +0.2, and +6.4 mV) and observed that the more positively charged ones have a greater internalization in cancer cells [44]. Osaka and colleagues produced magnetite nanoparticles with opposite charges (+9.4 and -8.3 mV) and observed a greater uptake by cancer cells of the positively charged nanoparticles

[45]. Nevertheless, the above-described charge constrains related to the nanoparticles' blood circulation time and tumor penetration still need to be taken into account when these are administered intravenously. In this regard, nanoparticles with charge reversal-features may be appealing since these can be engineered to be neutral during circulation and become positively charged in response to a tumor-microenvironment stimuli (*e.g.*, pH, enzymes) [46-48].

2.2.3. Shape

The shape is another important parameter to consider in the production of nanomaterials for cancer PTT/PDT. This feature mainly affects the nanoparticles' blood circulation time and the cellular internalization [49]. However, there is no consensus among researchers on what concerns the optimal shape for nanomaterials. Nanoparticles can be phagocytosed by macrophages, and some studies have demonstrated that nanorods can resist this process better than spherical-shaped nanoparticles [10, 50]. Arnida *et al.* demonstrated that spherical nanoparticles are 4 times more internalized by macrophages than the nanorods equivalents [51]. Moreover, rod-shaped nanoparticles can flow nearest to the wall of the vessels, augmenting their propensity to go through the fenestrae and consequently achieve tumor accumulation. Zhou *et al.* evaluated the tumor uptake and cellular internalization, demonstrating that rod-shaped nanoparticles have a superior performance than their spherical-shaped equivalents (**Figure 2.3**) [52].

In stark contrast, other reports have shown that spherical nanoparticles present more uptake in cancer cells than non-spherical nanomaterials. Li *et al.* performed molecular simulations to assess the cellular uptake of PEGylated nanoparticles with different shapes [53]. The gathered data suggested that the spherical nanoparticles achieve the highest internalization by cells when compared to cubic, rod, and disk-shaped nanoparticles. Zhao *et al.* analyzed three different shaped (spherical, rod, vesicles) nanoparticles in 2D and 3D *in vitro* cancer models [54]. These authors verified that the spherical nanoparticles have higher cellular internalization and penetration into spheroids.

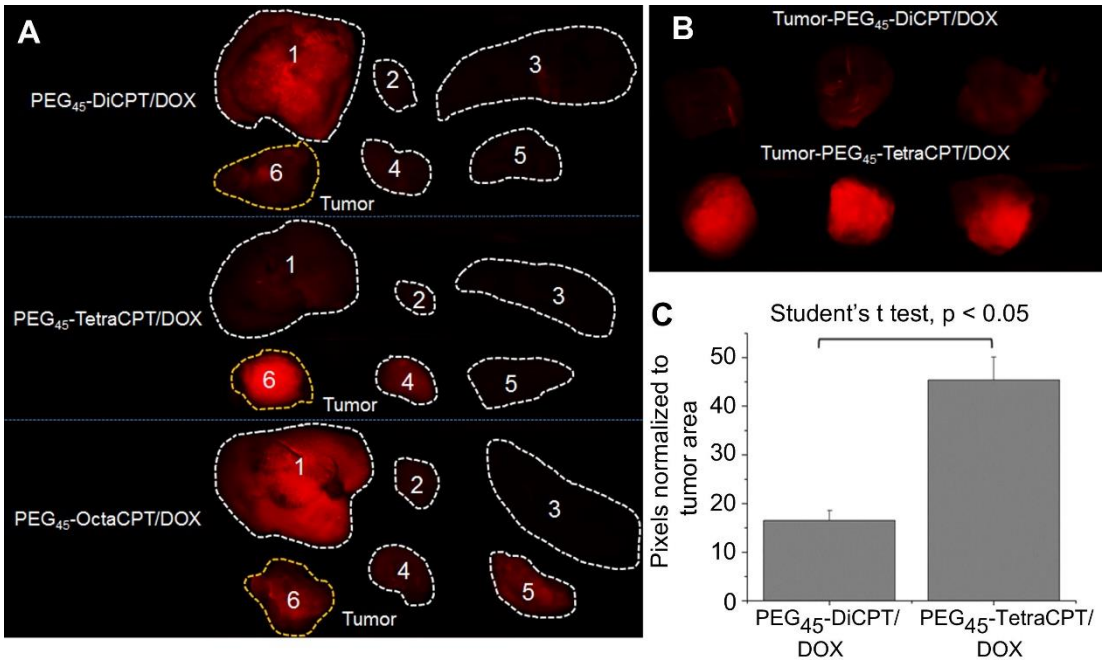

Figure 2.3. Biodistribution of nanoparticles with different shapes after intravenous administration in mice. (A) Fluorescence images in the major organs (1: liver; 2: heart; 3: spleen; 4: kidney; 5: lung; 6: tumor) after 8 h of injection of the nanoparticles. (B) Fluorescence images of the tumors of three mice injected with two different nanoparticles. (C) Pixels of the fluorescence in the tumors normalized to the tumor area. PEG_{45}-DiCPT/DOX: Doxorubicin loaded PEG-di-camptothecin conjugate sphere-shaped nanoparticles; PEG_{45}-TetraCPT/DOX: DOX loaded PEG-tetra-camptothecin conjugate rod-shaped nanoparticles; PEG_{45}-OctaCPT/DOX: DOX loaded PEG-octa-camptothecin conjugate rod-shaped nanoparticles. Reprinted with permission from [52]. Copyright 2013 Elsevier.

2.2.4. Targeting

Nanoparticles can be functionalized with different types of targeting ligands, which can affect their tumor accumulation and cellular internalization [55]. This strategy aims to bind the ligand-functionalized nanoparticles to receptors that are overexpressed in the tumor vasculature (*e.g.,* endoglin, vascular endothelial growth factor receptors, integrins $\alpha_v\beta_3$) or in the cancer cells' membranes (*e.g.,* folate receptor, biotin receptors, CD44) [56-62]. Chen *et al.* produced polydopamine (PDA)-coated mesoporous silica nanoparticles functionalized with HA (binds to CD44), demonstrating that these nanoparticles can be better internalized by cancer cells when compared with their equivalents without HA (**Figure 2.4**) [63]. He *et al.* produced Iron(II) phthalocyanine loaded nanoparticles functionalized with AS1411 (targeting agent for nucleolin), demonstrating an enhanced cell internalization and tumor uptake when compared to non-targeted nanoparticles [64]. Still, it should be noted that the efficacy of this strategy is influenced by the type and density of the ligands as well as by the length of the spacer arm between the nanomaterial and the ligand [65-67]. Moreover, a combination of

different ligands appears to be an appealing strategy to further enhance the therapeutic outcome. For instance, Cai *et al.* synthesized nanoparticles with different densities of folate and cyclic arginine-glycine-aspartic acid (cRGD) and observed that the nanoparticles with 75 % of cRGD and 25 % of folate present the greatest cellular uptake [68]. Regarding tumor vasculature targeting, Jenkins and coworkers functionalized gold nanocages with anginex, observing 3 times higher tumor accumulation of these nanoparticles than their equivalents without the targeting moieties [69]. In another work, Hao *et al.* produced PEGylated nanoparticles conjugated with IELLQAR, an E-selectin binding peptide, for targeting the vasculature of the tumor [70].

2.2.5. Corona

The nanoparticles' corona is another crucial property since it strongly influences the nanoparticles' hydrophilicity, stability, and cytocompatibility [42, 71, 72]. When in circulation, the blood proteins tend to adsorb on the nanoparticles' surface, accelerating their opsonization but also changing their properties such as surface charge or size [73]. These events can impair the capacity of the nanoparticles to reach the tumor site [72]. Fortunately, the decoration of the nanoparticles' surface with specific materials can prevent the occurrence of these phenomena [71]. For this purpose, the nanoparticles' corona has been coated with non-fouling hydrophilic polymers (*e.g.*, poly(ethylene glycol) (PEG)) [71]. Such coatings can improve nanoparticles' solubility/colloidal stability as well as prevent protein adsorption, ultimately improving the nanoparticles' blood circulation time and their propensity to reach the tumor site (by exploiting the static and dynamic pores on the tumor vasculature) [10, 73].

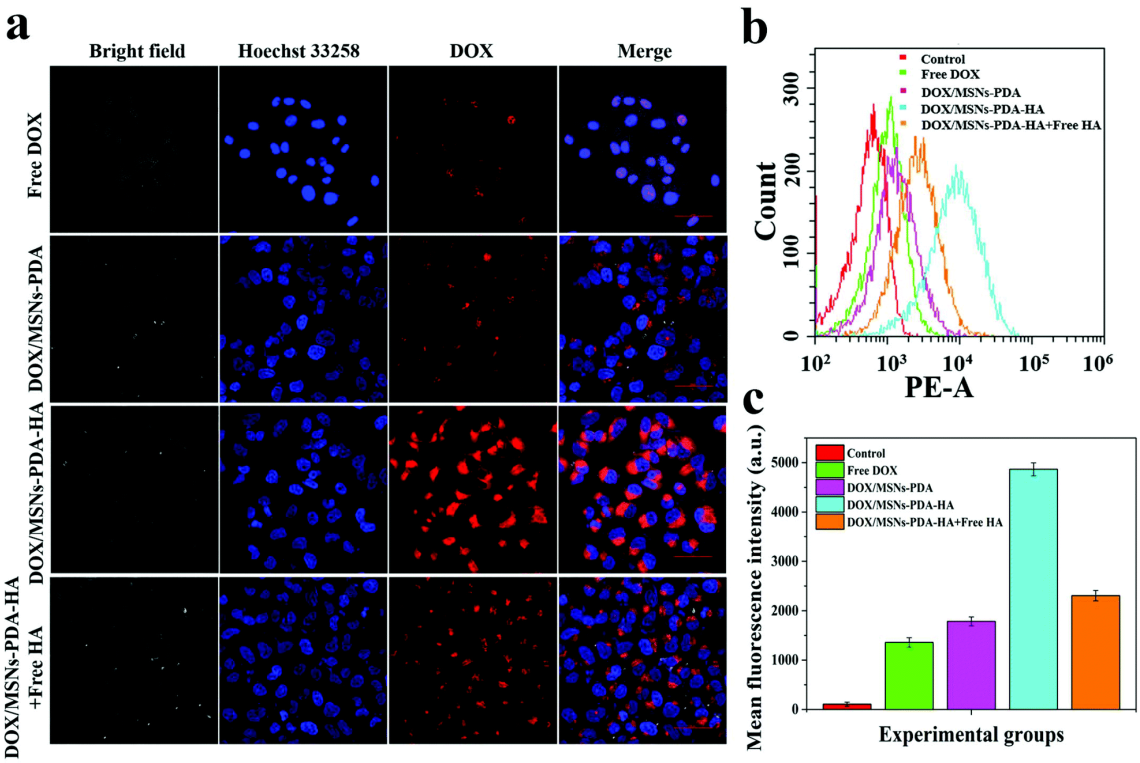

Figure 2.4. Cellular internalization of DOX loaded mesoporous silica nanoparticles (MSNs). (A) Confocal laser scanning microscopy images of cancer cells at 12 h after nanoparticles incubation. Scale bars correspond to 50 μm. (B) Flow cytometry of cancer cells after incubation with the nanoparticles. (C) Fluorescence intensity of nanoparticles in cancer cells. Control corresponds to blank MSNs. DOX/MSNs-PDA: DOX loaded MSNs functionalized with Polydopamine; DOX/MSNs-PDA-HA: DOX loaded MSNs functionalized with PDA and HA; PE-A: Phycoerythrin-Alexa Fluor® 647; a.u.: arbitrary unit. Reprinted with permission from [63]. Copyright 2019 Royal Society of Chemistry.

2.2.6. PEG-coated nanoparticles

The nanoparticles' surface is commonly coated with PEG. By coating nanoparticles with this synthetic polymer, their solubility/hydrophilicity, stability, and biocompatibility are enhanced [74, 75]. As importantly, nanoparticles with PEG in their corona have the capacity to resist protein adsorption and may resist uptake by macrophages, remaining for longer periods of time in the blood flow, thus improving their tumor accumulation [75, 76]. So far, several PEGylated materials have already been approved by the Food and Drug Administration (FDA) and European Medicines Agency (EMA), such as Doxil® and Onivyde® [77].

In this context, Wang *et al.* produced gold nanoparticles with and without PEG functionalization [78]. The nanoparticles without PEG almost did not accumulate in the tumor, while the PEGylated ones had a high tumor uptake of 10 % ID g^{-1}. Interestingly, the non-PEGylated nanoparticles accumulated 1.6 times more in the liver when

compared with the PEGylated nanoparticles. The benefits of PEGylation are also multifactorial, depending on the density and molecular weight of this polymer. Liu *et al.* produced gold nanoparticles functionalized with PEG with different molecular weights (0.55, 1, 2, and 5 kDa) [79]. They observed that nanoparticles with smaller PEG molecular weights (0.55 and 1 kDa) can be better internalized by cancer cells. Patsula *et al.* created magnetic nanoparticles with different PEG densities (0.76, 0.99, and 1.02 PEG nm^{-2}), observing that the nanoformulation with the highest grafting density presented the longest blood circulation time [80].

Despite all of these benefits, some recent studies have unveiled that PEG can be immunogenic [81-84]. Initially, it was uncovered that many healthy people have anti-PEG antibodies (without any treatment with PEGylated nanomaterials) [81, 85]. This phenomenon could be related to the presence of PEG in some cosmetic products (this also explains the greater occurrence of these antibodies in humans when compared to animals) and also due to genetic predisposition [81]. On the other hand, patients without preexisting anti-PEG antibodies demonstrated their production after the first administration of PEGylated nanomaterials [81]. This phenomenon impairs the efficacy of the treatment in the subsequent administrations. After the second administration of PEGylated nanomaterials, due to the complement system activation and the action of the antibodies, these are recognized by the mononuclear phagocyte system [86, 87]. The complement proteins can opsonize the PEGylated nanomaterials leading to their uptake by macrophages [81]. In this way, this event decreases the PEGylated nanoparticles' blood circulation half-life – known as the accelerated blood clearance (ABC) phenomenon [81, 88]. Still, it should be noted that the occurrence and magnitude of the ABC phenomenon depend on several factors such as the timeframe between the first and second administration, the dose in the first administration, the molecular weight and PEG density, and also the type of the nanoparticle used [86].

These issues have motivated the investigation of PEG alternatives to coat the nanoparticles. Namely, zwitterionic polymers and poly(2-oxazoline)s have shown the capacity to mimic the essential properties of PEG, while avoiding its immunogenic behavior (described in sections 2.2.7 and 2.2.8).

2.2.7. Zwitterionic-based nanoparticles

Zwitterionic polymers have been demonstrating to be a promising PEG alternative [89, 90]. These zwitterionic molecules have a neutral charge and have a low toxicity [91, 92]. Currently, poly(carboxybetaine)s and poly(sulfobetaine)s, or polymers engineered with their brushes, are being explored for the coating of nanoparticles [86, 93]. In fact, coating nanoparticles with these agents has improved their solubility, stability, and biocompatibility [94, 95]. As importantly, nanoparticles coated with these zwitterionic polymers display reduced protein adsorption and thus can display a high blood circulation time (half-life, $t_{1/2}$), which in turn favors their tumor uptake [86, 96].

For example, Yang *et al.* studied the protein adsorption on PEGylated nanoparticles and poly(carboxybetaine acrylamide) coated nanoparticles by analyzing their hydrodynamic size overtime when in contact with blood serum [93]. All the formulations remained stable for 72 h in medium with 10 % of blood serum. On the other hand, when incubated in 100 % blood serum (a large amount of proteins), the nanoparticles functionalized with poly(carboxybetaine acrylamide) remained stable, while the PEGylated ones suffered a great increase in their size (from 50 to 350 nm). In another work, Han *et al.* also compared the performance of a model protein coated with PEG and poly(carboxybetaine acrylamide) [97]. The authors observed that the PEGylated protein had a decrease in its blood circulation half-life from the first to the third injection ($t_{1/2}$ decreased from ≈ 16 to ≈ 8 h). The proteins functionalized with the zwitterionic polymers not only presented a greater blood circulation half-life, but this parameter also did not decrease after three injections ($t_{1/2}$ ≈ 27 to 26 h), demonstrating that this zwitterionic-based coating is not affected by the ABC phenomenon. Men *et al.* also studied the behavior of nanoparticles coated with PEG and poly(sulfobetaine methacrylate) [98]. In this regard, the zwitterionic-coated nanoparticles had a tumor uptake of 9.3 and 10.9 % ID g^{-1} at 24 and 48 h post-injection, respectively. In stark contrast, the tumor accumulation of the PEGylated nanoparticles, at the same time points, was only 5.1 and 2.3 % ID g^{-1}, respectively. Interestingly, the liver accumulation of the PEGylated nanoparticles was 4.3 times higher than that of the zwitterionic-coated nanoparticles (**Figure 2.5**). Guo *et al.* prepared poly(amide amine) dendrimers coated with poly(carboxybetaine methacrylamide) with different molecular weights [99]. In this regard, the dendrimers with 30 repetitions of the zwitterionic monomer had the longest blood circulation time when compared to those with 10 and 20 unit repetitions.

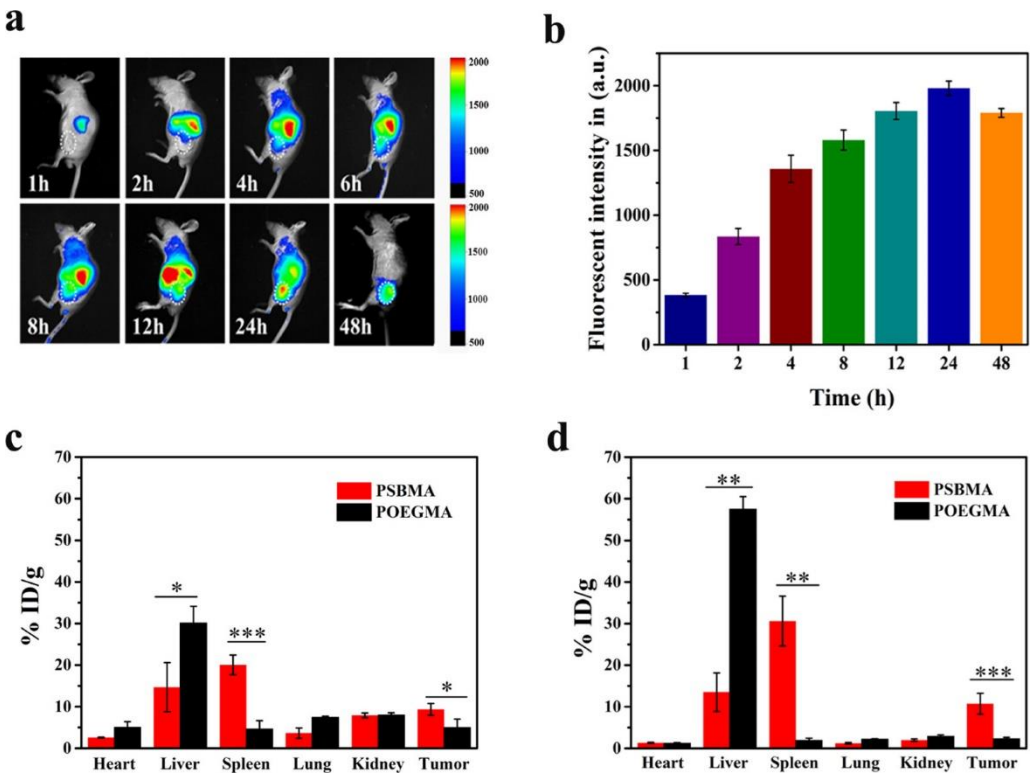

Figure 2.5. Biodistribution of nanoparticles with different corona compositions. (A) Fluorescence images of mice, at different time points, after poly(sulfobetaine methacrylate)-based nanoparticles (PSBMA) administration. (B) Fluorescence intensity of PSBMA-nanoparticles in the tumor. Biodistribution of nanoparticles in major organs after (C) 24 h and (D) 48 h of administration. $^{*}p < 0.05$, $^{**}p < 0.01$, $^{***}p < 0.001$. POEGMA: poly(oligo(ethylene glycol) methacrylate)-based nanoparticles; a.u.: arbitrary unit; % ID/g: percentage of injected dose per gram of tissue. Reprinted with permission from [98]. Copyright 2018 American Chemical Society.

2.2.8. Poly(2-oxazoline)-coated nanoparticles

Poly(2-oxazoline)s, in particular (2-methyl-2-oxazoline)s and poly(2-ethyl-2-oxazoline)s, are also very promising agents to replace PEG in the functionalization of nanoparticles aimed for cancer PTT/PDT [86]. Similar to the molecules described in sections 2.2.6 and 2.2.7, nanoparticles coated with poly(2-oxazoline)s can display an improved hydrophilicity/stability and biocompatibility [100, 101]. As importantly, the coating of nanoparticles with poly(2-oxazoline)s can prevent protein adsorption at their surface during blood circulation, hence improving their blood circulation times [102, 103]. In fact, He *et al.* demonstrated that poly(2-oxazoline)s-coated nanoparticles cannot activate the human complement system [104]. Moreadith *et al.* also unveiled that poly(2-oxazoline)s are non-immunogenic since these do not induce the production of antibodies [105].

Gao *et al.* demonstrated a higher internalization in cancer cells of black phosphorus nanosheets functionalized with poly(2-ethyl-2-oxazoline) when compared to their equivalents coated with PEG [106]. Due to their higher internalization, upon intravenous administration of these formulations and subsequent laser irradiation, the tumor of mice receiving poly(2-oxalozine)-coated nanoparticles had a temperature increase of ≈ 17 °C while the mice administered with the PEGylated nanoparticles had a temperature change of ≈ 10 °C. This data suggests an improved tumor-homing capacity of the poly(2-oxalozine)-coated nanoparticles. Dong *et al.* verified that the incorporation of Paclitaxel in poly(2-oxazoline)-based nanoparticles could improve the blood circulation half-life of this drug from 1.1 to 2.7 h [107]. Consequently, the Paclitaxel loaded poly(2-oxazoline)-based nanoparticles displayed ≈ 6 times higher tumor-uptake (when compared to the free Paclitaxel). Xu and coworkers prepared docetaxel loaded micelles with a surface coating composed of poly(2-methyl-2-oxazoline), verifying their ability to achieve a high tumor uptake and induce tumor regression [108]. Furthermore, Li *et al.* compared the biological performance of mesoporous silica nanoparticles functionalized with poly(2-ethyl-2-oxazoline) and PEG [109]. In this regard, the authors observed that the nanoparticles coated with poly(2-ethyl-2-oxazoline) can penetrate into the interior of artificial *in vitro* tumor models, while those coated with PEG only remained in the periphery. This behavior was attributed to the ability of these poly(2-ethyl-2-oxazoline)-coated nanoformulations to become positively charged at the pH of the tumor microenvironment, hence boosting their penetration capacity. *In vivo*, the poly(2-ethyl-2-oxazoline)-coated nanoparticles displayed the highest tumor uptake and thus promoted the best therapeutic outcome.

Similarly, the molecular weight of poly(2-oxazolines) can also influence the nanoparticles' properties [110, 111]. Pizzi *et al.* compared the biodistribution of nanoparticles coated with poly(2-ethyl-2-oxazoline) with 22, 25, and 108 monomer repetitions [110]. In this regard, the nanoformulations with the highest poly(2-ethyl-2-oxazoline) molecular weight (108 repetitions) displayed the longest blood residency, while those with the lowest molecular weight (22 repetitions) had the highest uptake by the liver and kidneys. Wen *et al.* prepared liposomes coated with poly(2-ethyl-2-oxazoline) with different molecular weights (1, 2, 3, 4, and 5 kDa) [111]. In this regard, the authors observed that the liposomes coated with poly(2-ethyl-2-oxazoline) with 1 and 2 kDa present better pH responsiveness and good stability. Between these formulations, the ones coated with poly(2-ethyl-2-oxazoline) with 2 kDa had the longest blood circulation half-life, which potentiated a greater therapeutic effect.

2.3. Parameters related to the laser light and photoresponsive nanoagents

After reaching the tumoral zone, nanoparticles must interact with external light (usually originated from a laser) in order to exert their photothermal and/or photodynamic effects [10, 19, 112]. Achieving appropriate levels of such effects depends on several factors related to the laser light: i) wavelength, ii) power density, iii) irradiation time, iv) number of irradiations, and iv) onset of the laser exposure [11, 113, 114].

Regarding the wavelength of the laser light, UV light (100-400 nm) can be used for PDT by producing reactive oxygen species when interacting with some nanomaterials such as TiO_2 nanoparticles [115, 116]. However, radiation with this wavelength presents off-target toxicity since it can be absorbed by water or cause DNA damage [117]. Due to these off-target interactions, UV radiation has a poor penetration depth capacity [117]. On the other hand, the use of NIR light (750-1000 nm) can solve these problems. The NIR light presents a low interaction with the body components such as melanin, hemoglobin, or water [22]. Due to this reason, the NIR radiation displays a great penetration capacity (up to 2 cm), making it the preferential choice for PDT and PTT [118]. Therefore, by using NIR light, it is possible to attain a spatio-temporal control over the therapeutic effect [29, 30].

Besides the wavelength of the NIR light, its power density (intensity) is another crucial factor [20, 119-121]. In general, increasing the laser power density can enhance the photothermal and photodynamic effects mediated by the nanoparticles [122, 123]. For instance, Liu and coworkers verified that by increasing the laser power density from 1 to 3 W cm^{-2} (808 nm, 25 min), the temperature increase mediated by Fe(III)-doped poly(aminopyrrole) nanoparticles could increase from ≈ 9.6 °C to ≈ 24.9 °C [124]. A similar outcome can also be attained by using longer irradiation times or through the application of multiple irradiation sessions [21, 124, 125]. Han *et al.* verified that cRGD functionalized Ag_2S nanoparticles could cause tumor growth reduction in mice after one NIR irradiation cycle (808 nm, 2 W cm^{-2}, 10 min) [21]. However, when three NIR irradiation cycles were applied, tumor eradication was attained. By last, controlling the onset of the laser exposure is also fundamental since the irradiation must be coincident with the timepoint in which the nanoparticles have the highest tumor uptake. For instance, Peng *et al.* verified that Fe_3O_4 nanoparticles coated with zwitterionic polymers achieve their maximum tumor accumulation at 4 h post-administration [96]. In this way, for the *in vivo* assays, the mice were irradiated with NIR light (808 nm, 3 W cm^{-2}, 5 min)

after 4 h of the nanoparticles' administration, and tumor eradication was attained. On the other hand, Shao and colleagues produced black phosphorus quantum dots loaded poly(lactic-*co*-glycolic acid) (PLGA) nanoparticles that reached their maximum tumor accumulation at 24 h post administration [126]. In this way, this time point was used for NIR laser irradiation (808 nm, 1 W cm^{-2}, 10 min), leading to tumor eradication in mice.

Apart from the parameters related to the laser light, those that derive from the nanomaterial are also crucial. The nanoparticles' features (size, charge, shape, corona, targeting ligands) that affect their ability to reach the tumor site were already described in section 2.2. On the other hand, the optical properties of the nanoparticles are also crucial. Based on the above, nanoparticles should have a high NIR absorption in order to interact with NIR light. To maximize the attained outcomes, the nanoparticles' maximum absorption in the NIR should also match the exact wavelength of the used NIR radiation (and *vice-versa*) [11, 127, 128]. Finally, the nanoparticles' photothermal conversion efficiency and singlet oxygen quantum yield are also important parameters that determine their potential for PTT and PDT, respectively [22, 129].

In this way, several nanomaterials presenting a high NIR absorption have been developed for application in cancer PTT/PDT: anisotropic gold- and graphene-based nanomaterials, PDA nanoparticles, heptamethine cyanines loaded nanostructures, among others [9, 112, 130, 131].

2.3.1. Graphene-based nanomaterials

A 2D nanomaterial that is widely used for cancer PTT due to its NIR absorption is graphene oxide (GO) [132-134]. GO presents a graphitic structure containing oxygen functional groups (*e.g.,* carboxyl, hydroxyl, epoxy) [133]. For the production of GO, first graphite suffers oxidation forming graphite oxide, followed by exfoliation yielding graphene oxide [135, 136]. A popular method to produce GO is the so-called "improved Hummer's method" which uses a mixture of H_2SO_4, H_3PO_4, and $KMnO_4$ to oxidize graphite [136-138].

Another graphene-based agent with great properties for PTT is reduced graphene oxide (rGO). This material is generally obtained through the chemical reduction of GO, to restore its graphitic lattice [139]. For this process, hydrazine hydrate is usually used, being L-ascorbic acid an environmentally friendly agent that can also reduce GO [139-141]. Both nanomaterials (GO and rGO) have a high superficial area (due to their

2D structure) [142]. In this way, the aromatic lattice of GO and rGO can load diverse therapeutic agents, such as chemo, immune or photodynamic agents [143, 144]. Furthermore, GO and rGO present NIR absorption, being able to produce a photoinduced heat [145, 146]. In this regard, rGO presents a higher NIR absorption than GO, and consequently a greater photothermal capacity [147-149].

Despite their properties, as-synthesized GO and rGO present a subpar cytocompatibility, propensity to aggregate in biological fluids, and a poor accumulation in the tumor zone [149, 150]. In order to surpass these bottlenecks, GO and rGO can be functionalized with biocompatible polymers containing hydrophilic brushes [149, 150]. For instance, Lima-Sousa *et al.* demonstrated that after functionalization with an HA-based amphiphilic polymer, rGO showed better cytocompatibility and stability [140]. In another work, Melo and coworkers verified that the inclusion of Sulfobetaine methacrylate brushes into bovine serum albumin (BSA)-coated GO could endow them with an improved colloidal stability [151]. Jun *et al.* produced folic acid-chitosan functionalized GO that could increase the tumor temperature by about 23.6 °C (808 nm, 2 W cm^{-2}, 5 min), leading to its eradication (**Figure 2.6**) [152].

2.3.2. Anisotropic gold nanoparticles

Gold-based nanomaterials are constituted with one of the less reactive metals known and can resist to oxidation and corrosion [153-155]. These nanoparticles have great optical properties and can be used for drug delivery, imaging, and cancer PTT [153, 156, 157]. This nanomaterial can also absorb light in specific wavelengths and can suffer electron oscillation on its surface, after interaction with light, causing a localized surface plasmon resonance phenomenon [158]. This capacity endows gold nanoparticles with a great conversion of light to heat capacity, greatly depending on their size and shape [158, 159].

Particularly, anisotropic gold nanoparticles (non-symmetrical) can display a shift in their optical absorption to the NIR region, granting them great imaging and phototherapeutic properties [156, 160]. The most used anisotropic gold nanoparticles for PTT are gold nanorods and nanocages [161]. For gold nanorods production, first hexadecyltrimethylammonium bromide (CTAB) with small gold nanospheres (called seeds) are allowed to react [156, 162]. Then, more CTAB, $HAuCl_4$, ascorbic acid (reducing agent), and $AgNO_3$ are added [162, 163]. These reagents are allowed to react slowly until nanorods are produced [162, 163]. Another type of anisotropic material is gold nanocages. For their production, there is a galvanic replacement of a template of

Ag nanocubes [164]. The gold precursor ($HAuCl_4$) is deposited on the surface of the pre-formed Ag cubes. Then, Ag is removed, yielding the gold nanocages [164, 165].

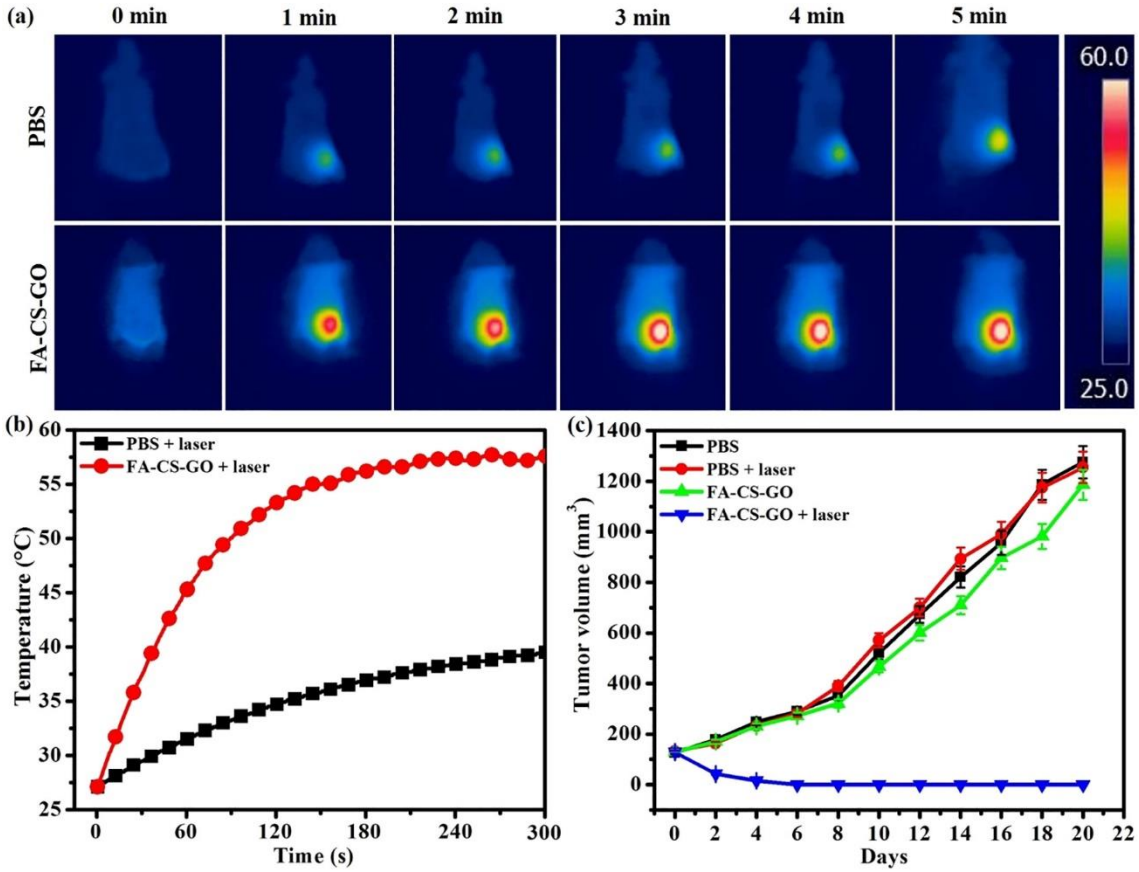

Figure 2.6. Photothermal effect mediated folic acid-chitosan functionalized GO (FA-CS-GO). (A) Thermal images of tumor-bearing mice after nanoparticles administration and NIR irradiation (808 nm, 2 W cm^{-2}, 1 to 5 min). (B) Temperature variation curves attained in the tumor of mice. (C) Tumor growth curves of mice exposed to different treatments. PBS: Phosphate Buffered Saline; laser: NIR laser irradiation (808 nm, 2 W cm^{-2}, 5 min). Reprinted with permission from [152]. Copyright 2020 Elsevier.

There are other promising shapes for PTT, such as gold nanostars or gold nanotriangles [166, 167]. Still, all of these types of gold nanoparticles need functionalization for surpassing some limitations such as poor colloidal stability, low loading capacity, photodegradability, and weak tumor-homing capacity [157]. To address these limitations, the functionalization of gold nanostructures with thiolated hydrophilic polymers is the most popular strategy [168, 169]. Another approach is to cover these anisotropic gold nanoparticles with a mesoporous silica shell [170, 171].

For instance, Huang *et al.* functionalized gold nanorods with a thiol-terminated zwitterionic polymer (poly(L-Glu-*co*-Lys acid)) [172]. After functionalization, the authors observed an improved tumor accumulation. This improved accumulation led to a greater photoinduced heat in the tumor region (approximately 17 °C, after irradiation for 10 min, 808 nm, 2 W cm^{-2}), consequently leading to tumor regression. In contrast, the non-functionalized gold nanorods only led to tumor growth reduction (due to their poor tumor uptake and inferior photothermal heating in the tumor zone). Moreira *et al.* verified that by coating doxorubicin (DOX) loaded mesoporous silica shell-coated gold nanorods with poly(2-ethyl-2-oxazoline), their ability to deliver this drug to cancer cells improved by 1.5-fold [173]. *In vitro*, the chemo-PTT mediated by this nano-system was capable of decreasing the cancer cells' viability to just ≈ 4 % (808 nm, 1.7 W cm^{-2}, 5 min). Jeon *et al.* produced PEGylated liposomes containing gold aggregates that displayed a high tumor uptake, and that with two NIR laser irradiation cycles (808 nm, 2.5 W cm^{-2}, 5 min), could induce tumor growth reduction [174]. Chen *et al.* produced cRGD-functionalized gold nanostars containing DOX [175]. These nanoparticles produced a tumor-confined photoinduced heat of about 10 °C (765 nm, 1 W cm^{-2}, 10 min) and successfully became internalized by cancer cells (about 3.2 times higher internalization than non-functionalized nanostars). In this way, the gold nanostars-cRGD-DOX plus NIR light caused the strongest tumor growth reduction in tumor-bearing mice, while gold nanostars alone (without cRGD nor DOX) plus NIR light barely reduced the tumor growth when compared to control.

2.3.3. CuS nanoparticles

CuS nanoparticles are produced by the polyol method, in which Cu precursors (CuO, CuCl) and S precursors (Na_2S, CH_4N_2S) react in ethylene glycol (a glycol solvent) [176-178]. By varying parameters such as temperature, time of reaction, and type of precursors, it is possible to produce CuS nanoparticles of different sizes or shapes (CuS nanospheres, nanorods, nanotubes) [176, 179]. These nanoparticles can absorb in the NIR region, causing a temperature increase (PTT) [180, 181]. Due to their small size, the CuS nanoparticles are generally rapidly removed by renal filtration [182]. CuS nanoparticles also present a poor colloidal stability, weak tumor accumulation, and lack of selectivity for cancer cells [179]. Thus, functionalizing these nanoparticles with polymers and/or targeting ligands that would improve their accumulation in the tumor is essential to enhance their therapeutic outcome [183, 184].

Li *et al.* functionalized mesoporous silica coated CuS nanoparticles with cRGD and TAT peptides [183]. Upon NIR laser irradiation (980 nm, 1.5 W cm^{-2}, 5 min,), these targeted nanoparticles mediated a temperature variation of almost 30 °C. In i*n vivo* studies, such hyperthermic effect led to tumor eradication in mice due to their preferential accumulation in the tumor. Jang *et al.* produced CuS nanoparticles coated with fucoidan for combinatorial chemo-PTT [185]. In this system, the fucoidan acts as a coating and anti-tumoral agent. When combined with NIR light (808 nm, 2 W cm^{-2}, 5 min), the CuS nanoparticles prompted a significant tumor growth reduction. In contrast, the chemo-PTT action of fucoidan-CuS nanoparticles led to tumor eradication. In a different approach, Cai and coworkers produced PEGylated hollow CuS nanoparticles loading Ku-60019 and functionalized with TGF-β antibodies [186]. These nanoparticles can successfully accumulate in the tumor, causing a temperature increase of about 20 °C (808 nm, 0.3 W cm^{-2}, 5 min). After 6 administration/laser irradiation sessions, the combined hyperthermic effect and chemotherapeutic effect mediated by these nanostructures led to tumor regression. Niu *et al.* produced chitosan-coated mesoporous silica nanoparticles that incorporated DOX and CuS nanoparticles [187]. *In vivo*, this nano-system could produce a temperature increase of ≈ 26 °C upon NIR laser irradiation (808 nm, 1 W cm^{-2}, 5 min), being its chemo-PTT capable of prompting tumor regression.

2.3.4. Transition Metal Dichalcogenide nanoparticles

Transition Metal Dichalcogenide (TMDCs) nanoparticles are 2D nanosheets based on the combination of a transition metal (one layer) between two layers of selenium, tellurium, or sulfur [188, 189]. This type of nanomaterials can absorb light in the NIR region with a high photothermal conversion capacity and also have a large surface area available for loading agents [190-195]. The TMDCs nanosheets can be produced by the Liquid Phase Exfoliation method in which multiple layers of a material are converted into an individual one, being dispersed in order to avoid aggregation of these individual sheets [196]. Subentry, these sheets are thinned and exfoliated through sonication [196, 197]. TMDCs sheets can also be synthesized through Chemical Vapor Deposition [198]. In this method, a precursor such as Ti or W is injected into a chamber under vacuum and high temperatures [199]. The metals are deposited on the substrate, and their size, morphology, and number of layers, can be tuned by the parameters of the process [198, 199]. However, as-synthesized TMDCs nanosheets present low colloidal stability, subpar biocompatibility, and poor tumor-homing capacity [200, 201]. Such drawbacks can be addressed by functionalizing TMDCs nanosheets with hydrophilic

polymers such as PEG [195, 201, 202]. For instance, Liu *et al.* functionalized MoS_2 nanosheets with PEG, verifying their ability to increase the tumor's temperature by 18 °C upon NIR laser irradiation (808 nm, 0.78 W cm^{-2}, 5 min) and consequently prompt tumor regression [195]. On the other hand, Cheng *et al.* produced PEGylated WS_2 nanoparticles that could generate a tumor-confined photoinduced heat to 65 °C, leading to tumor eradication (808 nm, 0.8 W cm^{-2}, 5 min) [202]. Liu's research group produced PEGylated $NbTe_2$ nanosheets loading integrated stress response inhibitors [119]. These nanosheets could increase the tumor temperature to about 53 °C, upon NIR laser irradiation (808 nm, 1.5 W cm^{-2}, 6 min). Moreover, the chemo-PTT mediated by this nano-system was capable of inducing tumor regression while the sole action of nanomaterials' PTT only caused tumor growth reduction (**Figure 2.7**). Yu and colleagues synthesized MoS_2 coated with a zwitterionic polymer based on carboxybetaine methacrylate, which presented a blood circulation half-life of almost 8 h, a high tumor uptake, and the ability to induce tumor regression after NIR laser irradiation (808 nm, 2 W cm^{-2}, 10 min) [203]. Moreover, Zhou *et al.* demonstrated that PEGylated MoS_2 nanoparticles incorporating Eu^{3+} are cytocompatible, but with the interaction with NIR light (808 nm, 1 W cm^{-2}, 5 min), these cause a temperature increase of about 37 °C that diminishes the viability of cancer cells to ≈ 27 % [204].

2.3.5. Polydopamine nanoparticles

PDA nanoparticles, generally produced by polymerizing dopamine in a basic solution, have also a high photothermal conversion efficiency [205-207]. The catechol-based surface of this type of nanomaterial allows the conjugation of drugs or their functionalization with hydrophilic polymers [208, 209]. The latter is crucial to improve PDA nanoparticles' colloidal stability and tumor-uptake [210-213].

For instance, Du *et al.* produced PDA nanoparticles incorporating a Cisplatin prodrug and coated with β-cyclodextrins [214]. These nanoparticles could reach the tumor after intravenous injection, generating a localized temperature increase to about 51 °C upon laser exposure (808 nm, 1 W cm^{-2}, 5 min). The chemo-PTT mediated by these nanoparticles led to tumor eradication. Li and coworkers prepared DOX loaded PEGylated PDA nanoparticles immobilized with RGD [215]. These nanoparticles could effectively accumulate in the tumor and increase its temperature to about 52 °C after NIR irradiation (808 nm, 2 W cm^{-2}, 5 min). This hyperthermic effect combined with the action of DOX led to tumor eradication. Ma *et al.* prepared calcium carbonate-PDA nanostructures that were loaded with DOX and passivated with a lipidic coating

containing PEG [216]. This nanoformulation had a high tumor-homing capacity, generating a local hyperthermia to about 44 °C (785 nm, 0.5 W cm^{-2}, 20 min), that with the assistance of DOX's action, mediated tumor's growth reduction.

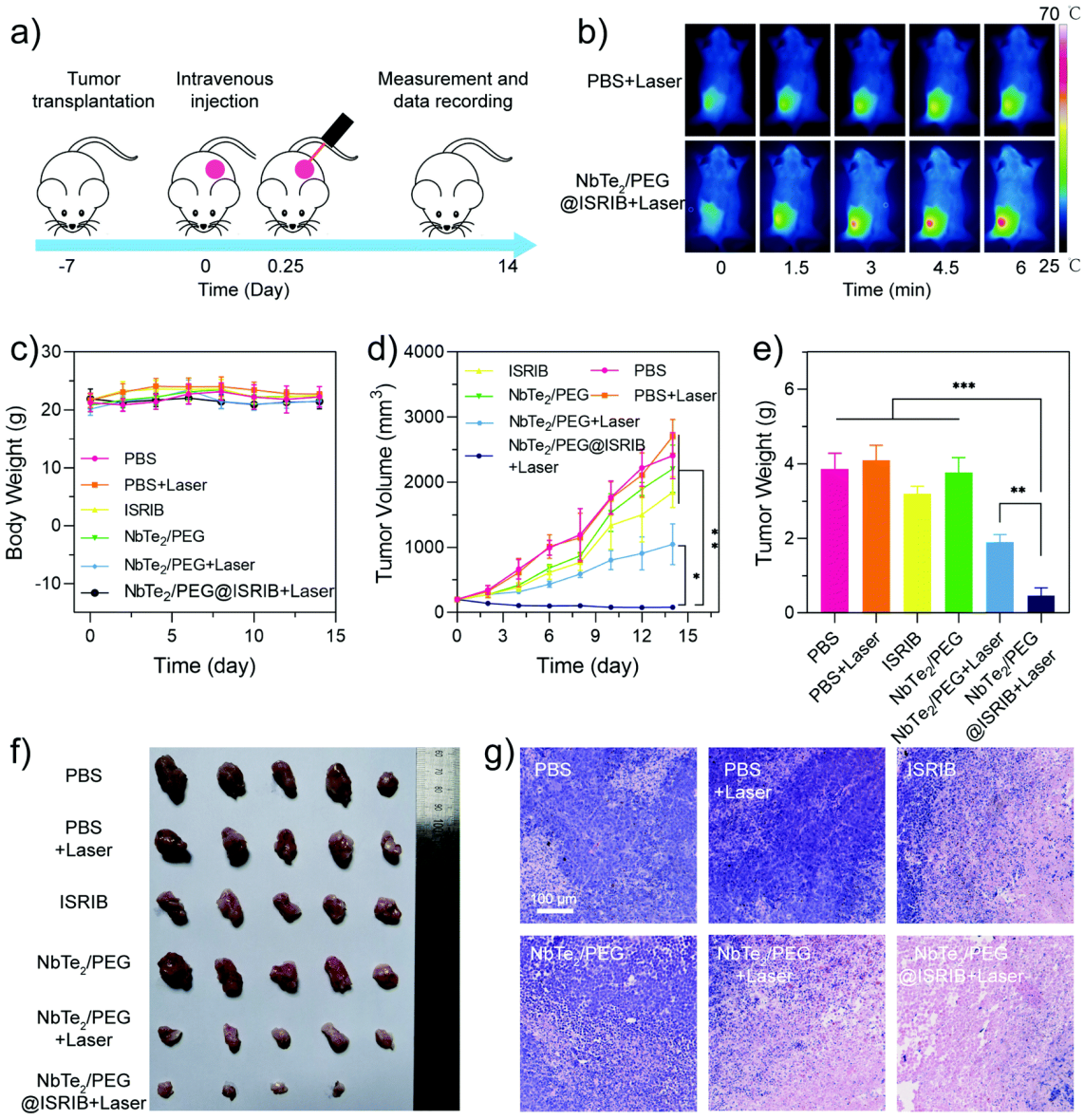

Figure 2.7. Photothermal effect mediated by PEGylated $NbTe_2$ nanosheets ($NbTe_2$/PEG). (A) Schematic representation of the PTT treatment. (B) Thermal images of tumor-bearing mice after nanoparticles administration and NIR irradiation (808 nm, 1.5 W cm^{-2}, 6 min). (C) Body weight variations of mice after treatment. (D) Tumor growth curves of mice exposed to the different treatments. (E) Weight of the tumors after the different treatments. *$p < 0.05$, **$p < 0.01$, ***$p < 0.001$ (F) Optical images of the removed tumors at the end point of the study. (G) Hematoxylin and Eosin staining of the tumor tissues. Scale bar corresponds to 100 μm. $NbTe_2$/PEG@ISRIB: PEGylated $NbTe_2$ nanosheets loading integrated stress response inhibitors; laser: NIR laser irradiation (808 nm, 1.5 W cm^{-2}, 6 min). Reprinted with permission from [119]. Copyright 2021 Royal Society of Chemistry.

2.3.6. Polypyrrole nanoparticles

Polypyrrole (PPy) nanoparticles have a strong NIR absorption and are easily synthesized [123, 217]. For their production, a simple polymerization process of the pyrrole monomer is performed [217-219]. Afterwards, the PPy nanoparticles are functionalized in order to attain the desired biological features [122, 220]. Yang *et al.* functionalized PPy nanoparticles with poly(vinyl alcohol) that can attain a temperature variation of about 35 °C upon NIR laser exposure (808 nm, 0.5 W cm^{-2}, 5 min), thus eradicating the tumor in mice [122]. Liang *et al.* produced PEGylated PPy nanoparticles that could generate a temperature increase of approximately 35 °C, upon NIR laser irradiation (808 nm, 1.5 W cm^{-2}, 10 min), leading to tumor growth inhibition in mice [221]. Lu and coworkers produced PPy nanoparticles coated with fucoidan [220]. *In vivo*, these nanostructures could generate a localized photoinduced heat (NIR laser, 1.25 W cm^{-2}, 5 min) that elevated tumor's temperature to 56 °C. The combined action of this hyperthermic effect and fucoidan's action led to tumor eradication. Burnouf *et al.* prepared platelet-coated poly(ethyleneimine)-PPy nanoparticles, verifying *in vivo* their ability to produce a photoinduced heat to about 55 °C (808 nm, 2 W cm^{-2}, 10 min) [222]. By applying twice this administration and NIR irradiation protocol, tumor eradication was attained.

2.3.7. PEDOT-based nanoparticles

Poly(3,4-ethylenedioxythiophene) (PEDOT) nanoparticles are produced by oxidative polymerization of EDOT monomers and are great candidates to be used in PTT but present low solubility, and tumor homing-capacity [223-226]. Fortunately, such limitations can be addressed through their coating [226, 227]. Cheng *et al.* PEGylated PEDOT:PSS nanoparticles in order to increase their blood circulation time and tumor uptake [227]. *In vivo*, these nanoparticles generated a localized photoinduced heat to ≈ 51 °C that was sufficiently high to prompt tumor eradication (808 nm, 0.5 W cm^{-2}, 5 min). In another work, Liu *et al.* prepared poly(*N*-isopropylacrylamide-*co*-acrylic acid) coated PEDOT nanoparticles that could generate a tumor-confined temperature increase to about 47 °C, leading to tumor regression (808 nm, 0.8 W cm^{-2}, 6 min) (**Figure 2.8**) [20]. Odda and colleagues coated α-Fe_2O_3 nanoparticles with a PEDOT shell [228]. Due to this PEDOT coating, the nanostructures' photoinduced heat increased by about 1.52-fold (808 nm, 1 W cm^{-2}, 10 min).

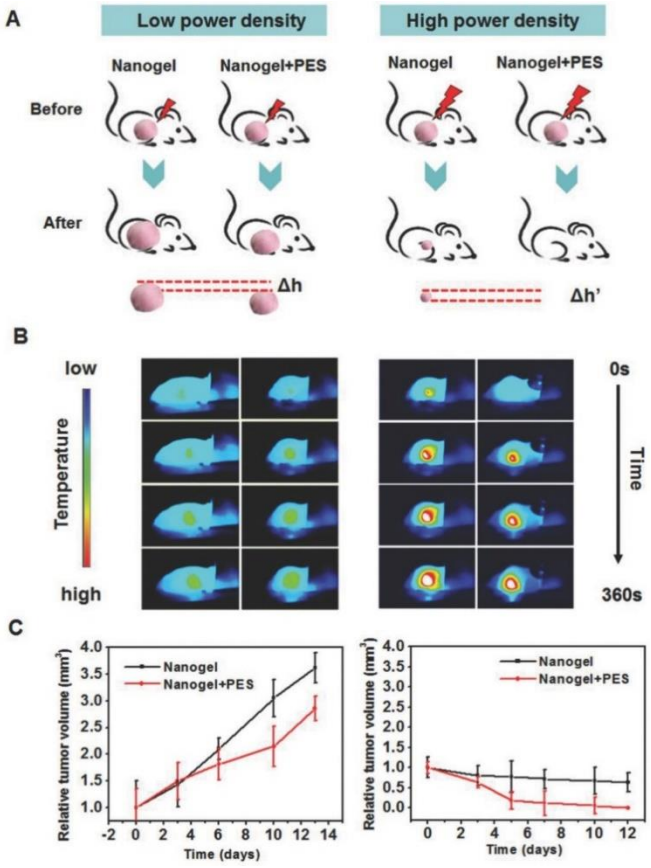

Figure 2.8. Photothermal effect mediated by PEDOT-based nanogels. (A) Schematic representation of the PTT procedure. (B) Thermal images of tumor-bearing mice after nanoparticles administration and NIR irradiation (808 nm, 6 min) with low power density (left; 0.3 W cm^{-2}) and high power density (right; 0.8 W cm^{-2}). (C) Tumor growth curves of mice exposed to different nanoparticles and irradiated with a low power density (left; 0.3 W cm^{-2}) and at a high power density (right; 0.8 W cm^{-2}). Nanogel: poly(*N*-isopropylacrylamide-*co*-acrylic acid) coated PEDOT nanoparticles; Nanogel+PES: poly(*N*-isopropylacrylamide-*co*-acrylic acid) coated PEDOT nanoparticles plus phenylethynesulfonamide (heat shock protein 70 inhibitor). Reprinted with permission from [20]. Copyright 2016 Wiley.

2.3.8. Polyaniline nanoparticles

Polyaniline nanoparticles are NIR-responsive photothermal agents that are produced through the oxidative polymerization of the aniline monomer [229, 230]. Despite their good photothermal conversion efficiency, these nanoparticles also lack colloidal stability and present a subpar compatibility and tumor-homing capacity [231, 232]. Similarly to the other conductive polymer-based nanoparticles (PPy and PEDOT nanoparticles), such drawbacks can be overcome through their functionalization [231, 232]. Jiang *et al.* produced HA-polyaniline nanoparticles that successfully improve their solubility in water compared with as-synthesized polyaniline nanoparticles [232]. The HA-polyaniline nanoparticles could cause a temperature variation of ≈ 40 °C upon NIR

exposure (808 nm, 2 W cm^{-2}, 10 min). After administration in mice and irradiation of the tumor zone (808 nm, 0.64 W cm^{-2}, 5 min), the eradication of the tumor mass could almost be attained. Furthermore, Zhou *et al.* produced polyaniline nanoparticles coated with Pluronic F127 polymer [233]. Upon NIR exposure (808 nm, 0.5 W cm^{-2}, 5 min), these nanoparticles could increase the temperature by about 20 °C and cause tumor regression in *in vivo* studies (20 min irradiation). Moreover, Zhang *et al.* prepared DOX loaded PEGylated mesoporous polyaniline nanoparticles [120]. *In vitro*, these nanoparticles could increase the temperature to about 65 °C after NIR irradiation (808 nm, 1.5 W cm^{-2}, 5 min). When cancer cells were incubated with PEGylated mesoporous polyaniline nanoparticles plus NIR light (808 nm, 1.5 W cm^{-2}, 6 min; nanomaterials' PTT) and DOX loaded PEGylated mesoporous polyaniline nanoparticles (nanomaterials' chemotherapy), their viability remained at 28.6 and 39.4 %, respectively. In turn, the action of DOX loaded PEGylated mesoporous polyaniline nanoparticles plus NIR light decreased the cancer cells' viability to just 9 %, demonstrating their potential for chemo-PTT. In other research study, Fu and coworkers produced polyaniline nanoparticles passivated with L-cysteine [121]. *In vivo*, this nano-system generated a tumor-confined hyperthermia to about 52 °C (808 nm, 1.6 W cm^{-2}, 10 min) that led to tumor growth reduction.

2.3.9. ICG-based nanomaterials

ICG is a NIR-responsive heptamethine cyanine with photothermal, photodynamic, and imaging capabilities that is approved by FDA and EMA [234, 235]. For its application in cancer PTT, this small molecule is loaded into the hydrophobic core of nanoparticles [234]. In this way, the preparation of ICG loaded nanoparticles is a straightforward process when compared to those inorganic photothermal agents described above (*e.g.,* graphene derivatives, anisotropic gold nanoparticles). In fact, the encapsulation of ICG in nanomaterials is crucial to improve its blood circulation time (non-encapsulated ICG is rapidly excreted by renal filtration), tumor uptake, and selectivity towards cancer cells [236, 237]. For instance, Yoon *et al.* produced PEG-based liposomes encapsulating ICG that can produce a tumor-confined temperature increase of about 13 °C (808 nm, 0.6 mW cm^{-2}, 20 min), leading to tumor eradication [238]. An and coworkers verified that the incorporation of ICG in BSA nanoparticles could greatly improve its tumor uptake (when compared to free ICG) [239]. The BSA-ICG nanoparticles could generate a photoinduced temperature increase of ≈ 25 °C, and *in vivo,* were able to severely reduce the tumor growth (808 nm, 1 W cm^{-2}, 10 min). Moreover, Wang and

colleagues produced PEG-ICG conjugate-based nanoparticles loaded with L-arginine (acts as a nitric oxide donor) [240]. These nanostructures displayed a good tumor-homing capacity, producing a localized photoinduced to about 45 °C (808 nm, 1 W cm^{-2}, 5 min). The combination of the hyperthermic effect and nitric oxide gas therapy led to tumor eradication.

Despite this potential, ICG loaded nanoparticles still present some limitations that are intrinsic to the ICG molecule such as low photostability, weak fluorescence and ROS quantum yields, and subpar photothermal capacity [22, 241]. To address these limitations, ICG analogs (also known as prototypic heptamethine cyanines) are currently being explored for cancer PTT/PDT (discussed in the next section).

2.3.10. Prototypic heptamethine cyanine loaded nanoparticles

Prototypic Heptamethine Cyanines (*i.e.*, ICG analogs) have also been demonstrating promising results for cancer therapy [22]. Similar to ICG, these also have a multimodal character, enabling their use for PTT, PDT, and fluorescence imaging [242, 243]. As importantly, the prototypic heptamethine cyanines (*e.g.*, **IR783** (2-[2-[2-Chloro-3-[2-[1,3 - dihydro - 3,3 - dimethyl - 1 - (4 - sulfobutyl) - 2*H* - indol - 2 - ylidene] - ethylidene]- 1 - cyclohexen-1-yl] - ethenyl]- 3, 3 - dimethyl- 1- (4-sulfobutyl)-3*H*-indolium hydroxide), **IR780**, **IR820** (2-[2-[2-Chloro-3-[[1,3-dihydro-1,1-dimethyl-3-(4-sulfobutyl)-2*H*-benzo[e]indol-2 -ylidene] - ethylidene]- 1 -cyclohexen - 1-yl]-ethenyl]-1,1-dimethyl-3-(4-sulfobutyl)-1*H*-benzo[e]indolium hydroxide)) present far greater optical properties than ICG, namely a greater NIR absorption and better singlet oxygen/fluorescence quantum yield [244-246]. Still, these molecules have low solubility, photostability and blood circulation time, compromising their direct application for cancer therapy [247-249].

In general, the limitations of the prototypic heptamethine cyanines can be overcome through their incorporation in nanomaterials with proper physicochemical features [241]. Lv *et al.* produced PEGylated liposomes incorporating IR783 that presented a 5-fold higher tumor uptake than free IR783 [247]. By decorating these IR783 loaded PEGylated liposomes with cRGD, their tumor homing capacity was greatly improved, being 4 and 15 times greater than that presented by the IR783 loaded PEGylated liposomes and free IR783. Owing to this improved tumor uptake, the cRGD-functionalized PEGylated liposomes mediated the highest photoinduced heat (808 nm, 0.5 W cm^{-2}, 5 min), leading to the most promising therapeutic outcome (tumor

growth reduction). Valcourt and coworkers verified that the incorporation of IR820 into PLGA nanoparticles is essential to preserve their optical properties for up to 30 days (free IR820 suffered degradation during this period) [250]. *In vivo*, these nanostructures were able to reach the tumor, producing a localized photoinduced heat to about 44 °C (808 nm, 1.5 W cm^{-2}, 5 min) that caused tumor regression. Shi *et al.* produced poly(vinyl alcohol)-coated PLGA nanoparticles loading IR820 and chloroquine (autophagy inhibitor) [251]. After laser exposure (808 nm, 1 W cm^{-2}, 7 min), the combined action of the tumor-confined hyperthermia (45 °C) and chloroquine's action led to tumor regression.

Besides IR783 and IR820, IR780 is another prototypic heptamethine cyanine that has been receiving a great interest due to its far greater NIR absorption and fluorescence/singlet oxygen quantum yields [252-254]. This molecule suffers from the same drawbacks (low solubility and short blood circulation time) but its incorporation into nanostructures overcomes such limitations [255, 256]. For instance, Lin *et al.* produced PEGylated human serum albumin nanoparticles loading IR780 and superparamagnetic iron oxide nanoparticles [257], verifying that the tumor uptake of this nanoformulation was far superior to that displayed by free IR780. Afterwards, the tumor zone was exposed to several NIR irradiations (808 nm, 1 W cm^{-2}, 5 min, 5 cycles of irradiation), and the nanostructures' phototherapeutic effect led to tumor regression. Zhu *et al.* also verified that the incorporation of IR780 into PEGylated nanoparticles (that also contained DOX) could increase the tumor uptake of this agent [258]. Moreover, after nanoparticles administration and NIR irradiation (808 nm, 1.6 W cm^{-2}, 3 min, 2 cycles), the chemo-PTT mediated by this nano-system led to a reduction in the tumor's growth.

Song and coworkers produced Folate-functionalized PEGylated liposomes encapsulating IR780 [259]. When compared to their PEGylated equivalents and free IR780, the Folate-functionalized PEGylated liposomes presented a 2- and 5-fold greater tumor uptake, respectively. Due to this improved tumor uptake, the targeted IR780 liposomes produced a photoinduced heat to 50.5 °C (808 nm, 1 W cm^{-2}, 10 min), leading to tumor eradication (**Figure 2.9**).

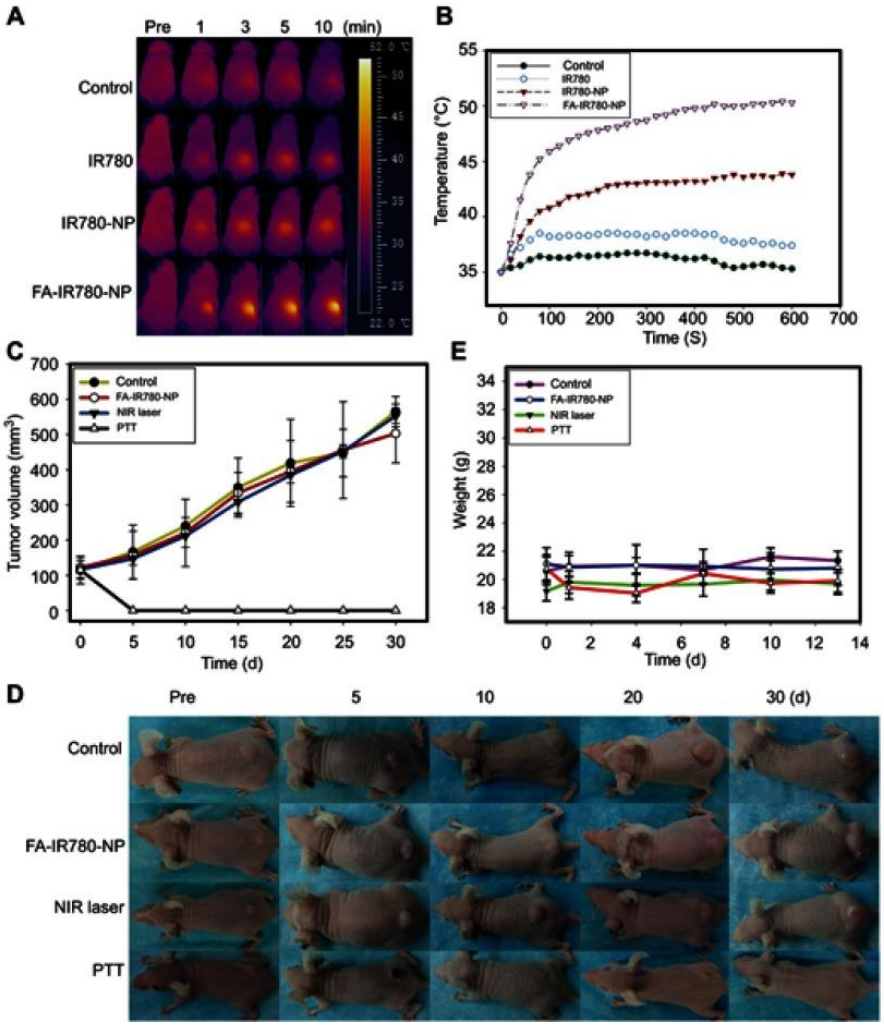

Figure 2.9. Photothermal effect *in vivo* mediated by Folate-functionalized PEGylated liposomes encapsulating IR780 (FA-IR780-NP). (A) Thermal images of tumor-bearing mice after nanoparticles administration and NIR irradiation (808 nm, 1 W cm^{-2}, 10 min), and (B) respective temperature variation curves. (C) Tumor growth curves of mice exposed to the different treatments. (D) Images of the tumor bearing-mice for 30 days. (E) Body weight variations of mice after the different treatments. IR780-NP: PEGylated liposomes encapsulating IR780; NIR laser: (808 nm, 1 W cm^{-2}, 10 min); PTT: FA-IR780-NP plus NIR laser. Reprinted with permission from [259]. Copyright 2019 Dove press.

Potara and coworkers also prepared folic acid-chitosan functionalized PEGylated nanostructures incorporating IR780 [260]. The targeted nanostructures achieved a greater uptake in cancer cells, and thus their photothermal effect (9 °C of temperature increase; 785 nm, 0.17 W cm^{-2}, 5 min) outperformed their non-targeted equivalents.

Lu *et al.* produced PEGylated liposomes encapsulating IR780, which display a high photostability, even after multiple irradiation cycles, unlike free IR780 [261]. *In vivo*, after three NIR laser irradiation cycles (808 nm, 1 W cm^{-2}, 5 min), tumor growth reduction was attained.

These results demonstrate the applicability of IR780-based nanomaterials in cancer PTT. Still, most nanomaterials were decorated with PEG, which is not ideal considering the growing evidence on the immunogenicity of this polymer (described in section 2.2.6). Therefore, developing and validating the potential of IR780-based nanostructures coated with alternative polymers, such as zwitterionic brushes or poly(2-oxazoline), is important to push their translation.

2.4. References

[1] R.L. Siegel, K.D. Miller, H.E. Fuchs, A. Jemal, Cancer statistics, 2022, Ca-Cancer J. Clin., 72 (2022) 7-33.

[2] H. Sung, J. Ferlay, R.L. Siegel, M. Laversanne, I. Soerjomataram, A. Jemal, F. Bray, Global cancer statistics 2020: GLOBOCAN estimates of incidence and mortality worldwide for 36 cancers in 185 countries, Ca-Cancer J. Clin., 71 (2021) 209-249.

[3] D.J. Tandberg, B.C. Tong, B.G. Ackerson, C.R. Kelsey, Surgery versus stereotactic body radiation therapy for stage I non–small cell lung cancer: A comprehensive review, Cancer, 124 (2018) 667-678.

[4] I. Uddin, Chemotherapy induced nausea and vomiting in patient suffering from sigmoid colon cancer (case report), Journal of Pathology Research Reviews & Reports, 119 (2020) 1-2.

[5] Y.-Q. Liu, X.-L. Wang, D.-H. He, Y.-X. Cheng, Protection against chemotherapy- and radiotherapy-induced side effects: A review based on the mechanisms and therapeutic opportunities of phytochemicals, Phytomedicine, 80 (2021) 153402.

[6] S.M. Ferrari, P. Fallahi, G. Elia, F. Ragusa, I. Ruffilli, A. Patrizio, M.R. Galdiero, E. Baldini, S. Ulisse, G. Marone, Autoimmune endocrine dysfunctions associated with cancer immunotherapies, Int. J. Mol. Sci., 20 (2019) 2560.

[7] M. Tocut, R. Brenner, G. Zandman-Goddard, Autoimmune phenomena and disease in cancer patients treated with immune checkpoint inhibitors, Autoimmun. Rev., 17 (2018) 610-616.

[8] H. Ma, M. Xue, Recent advances in photothermal applications of two-dimensional nanomaterials: photothermal therapy and beyond, J. Mater. Chem. A, 9 (2021) 17569-17591.

[9] N. Fernandes, C.F. Rodrigues, A.F. Moreira, I.J. Correia, Overview of the application of inorganic nanomaterials in cancer photothermal therapy, Biomater. Sci., 8 (2020) 2990-3020.

[10] D. de Melo-Diogo, C. Pais-Silva, D.R. Dias, A.F. Moreira, I.J. Correia, Strategies to improve cancer photothermal therapy mediated by nanomaterials, Adv. Healthcare Mater., 6 (2017) 1700073.

[11] A.S.C. Gonçalves, C.F. Rodrigues, A.F. Moreira, I.J. Correia, Strategies to improve the photothermal capacity of gold-based nanomedicines, Acta Biomater., 116 (2020) 105-137.

[12] S. Goel, C.A. Ferreira, P. Dogra, B. Yu, C.J. Kutyreff, C.M. Siamof, J.W. Engle, T.E. Barnhart, V. Cristini, Z. Wang, Size-optimized Ultrasmall porous silica nanoparticles depict vasculature-based differential targeting in triple negative breast cancer, Small, 15 (2019) 1903747.

[13] H. Kang, S. Rho, W.R. Stiles, S. Hu, Y. Baek, D.W. Hwang, S. Kashiwagi, M.S. Kim, H.S. Choi, Size-dependent EPR effect of polymeric nanoparticles on tumor targeting, Adv. Healthcare Mater., 9 (2020) 1901223.

[14] J. Fang, W. Islam, H. Maeda, Exploiting the dynamics of the EPR effect and strategies to improve the therapeutic effects of nanomedicines by using EPR effect enhancers, Adv. Drug Delivery Rev., 157 (2020) 142-160.

[15] J. Wu, The enhanced permeability and retention (EPR) effect: the significance of the concept and methods to enhance its application, J. Pers. Med., 11 (2021) 771.

[16] Y. Matsumoto, J.W. Nichols, K. Toh, T. Nomoto, H. Cabral, Y. Miura, R.J. Christie, N. Yamada, T. Ogura, M.R. Kano, Y. Matsumura, N. Nishiyama, T. Yamasoba, Y.H. Bae, K. Kataoka, Vascular bursts enhance permeability of tumour blood vessels and improve nanoparticle delivery, Nat. Nanotechnol., 11 (2016) 533-538.

[17] C.F. Rodrigues, N. Fernandes, D. de Melo-Diogo, I.J. Correia, A.F. Moreira, Cell-derived Vesicles for the Nanoparticles' Coating: Biomimetic Approaches for Enhanced Blood Circulation and Cancer Therapy, Adv. Healthcare Mater., n/a (2022) 2201214.

[18] K. Igarashi, H. Cabral, T. Hong, Y. Anraku, F. Mpekris, T. Stylianopoulos, T. Khan, A. Matsumoto, K. Kataoka, Y. Matsumoto, Vascular Bursts Act as a Versatile Tumor Vessel Permeation Route for Blood-Borne Particles and Cells, Small, 17 (2021) 2103751.

[19] S. Wen, X. Miao, G.-C. Fan, T. Xu, L.-P. Jiang, P. Wu, C. Cai, J.-J. Zhu, Aptamer-Conjugated Au Nanocage/SiO2 Core–Shell Bifunctional Nanoprobes with High Stability and Biocompatibility for Cellular SERS Imaging and Near-Infrared Photothermal Therapy, ACS Sens., 4 (2019) 301-308.

[20] D. Liu, L. Ma, Y. An, Y. Li, Y. Liu, L. Wang, J. Guo, J. Wang, J. Zhou, Thermoresponsive Nanogel-Encapsulated PEDOT and HSP70 Inhibitor for Improving the Depth of the Photothermal Therapeutic Effect, Adv. Funct. Mater., 26 (2016) 4749-4759.

[21] R. Han, Y. Xiao, Q. Yang, M. Pan, Y. Hao, X. He, J. Peng, Z. Qian, Ag2S nanoparticle-mediated multiple ablations reinvigorates the immune response for enhanced cancer photo-immunotherapy, Biomaterials, 264 (2021) 120451.

[22] M.M. Leitão, D. de Melo-Diogo, C.G. Alves, R. Lima-Sousa, I.J. Correia, Prototypic heptamethine cyanine incorporating nanomaterials for cancer phototheragnostic, Adv. Healthcare Mater., 9 (2020) 1901665.

[23] Y.J. Hou, X.X. Yang, R.Q. Liu, D. Zhao, C.X. Guo, A.C. Zhu, M.N. Wen, Z. Liu, G.F. Qu, H.X. Meng, Pathological Mechanism of Photodynamic Therapy and Photothermal Therapy Based on Nanoparticles, Int. J. Nanomed., 15 (2020) 6827-6838.

[24] K.F. Chu, D.E. Dupuy, Thermal ablation of tumours: biological mechanisms and advances in therapy, Nat. Rev. Cancer, 14 (2014) 199-208.

[25] E.C. Aniogo, B.P.A. George, H. Abrahamse, Role of Bcl-2 Family Proteins in Photodynamic Therapy Mediated Cell Survival and Regulation, Molecules, 25 (2020) 5308.

[26] D.L. Sai, J. Lee, D.L. Nguyen, Y.-P. Kim, Tailoring photosensitive ROS for advanced photodynamic therapy, Exp. Mol. Med., 53 (2021) 495-504.

[27] M. Zhou, M. Tian, C. Li, Copper-Based Nanomaterials for Cancer Imaging and Therapy, Bioconjugate Chem., 27 (2016) 1188-1199.

[28] N. Gupta, R. Malviya, Understanding and advancement in gold nanoparticle targeted photothermal therapy of cancer, Biochim. Biophys. Acta, Rev. Cancer, 1875 (2021) 188532.

[29] C.G. Alves, D. de Melo-Diogo, R. Lima-Sousa, I.J. Correia, IR780 loaded sulfobetaine methacrylate-functionalized albumin nanoparticles aimed for enhanced breast cancer phototherapy, Int. J. Pharm., 582 (2020) 119346.

[30] J. Li, R. Jiang, Q. Wang, X. Li, X. Hu, Y. Yuan, X. Lu, W. Wang, W. Huang, Q. Fan, Semiconducting polymer nanotheranostics for NIR-II/Photoacoustic imaging-guided photothermal initiated nitric oxide/photothermal therapy, Biomaterials, 217 (2019) 119304.

[31] A. Ahmed, S. Sarwar, Y. Hu, M.U. Munir, M.F. Nisar, F. Ikram, A. Asif, S.U. Rahman, A.A. Chaudhry, I.U. Rehman, Surface-modified polymeric nanoparticles for drug delivery to cancer cells, Expert Opin. Drug Delivery, 18 (2021) 1-24.

[32] E. Alphandéry, Biodistribution and targeting properties of iron oxide nanoparticles for treatments of cancer and iron anemia disease, Nanotoxicology, 13 (2019) 573-596.

[33] Y. Inoue, Y. Matsumoto, K. Toh, K. Miyano, H. Cabral, K. Igarashi, S. Iwasaki, K. Kataoka, T. Yamasoba, Manipulating dynamic tumor vessel permeability to enhance polymeric micelle accumulation, J. Controlled Release, 329 (2021) 63-75.

[34] H. Kang, S. Rho, W.R. Stiles, S. Hu, Y. Baek, D.W. Hwang, S. Kashiwagi, M.S. Kim, H.S. Choi, Size-Dependent EPR Effect of Polymeric Nanoparticles on Tumor Targeting, Adv. Healthcare Mater., 9 (2020) 1901223.

[35] Y. Liu, J.R. Ashton, E.J. Moding, H. Yuan, J.K. Register, A.M. Fales, J. Choi, M.J. Whitley, X. Zhao, Y. Qi, Y. Ma, G. Vaidyanathan, M.R. Zalutsky, D.G. Kirsch, C.T. Badea, T. Vo-Dinh, A Plasmonic Gold Nanostar Theranostic Probe for In Vivo Tumor Imaging and Photothermal Therapy, Theranostics, 5 (2015) 946-960.

[36] H. Yang, H. He, Z. Tong, H. Xia, Z. Mao, C. Gao, The impact of size and surface ligand of gold nanorods on liver cancer accumulation and photothermal therapy in the second near-infrared window, J. Colloid Interface Sci., 565 (2020) 186-196.

[37] P. Makvandi, M. Ghomi, M. Ashrafizadeh, A. Tafazoli, T. Agarwal, M. Delfi, J. Akhtari, E.N. Zare, V.V.T. Padil, A. Zarrabi, N. Pourreza, W. Miltyk, T.K. Maiti, A review on advances in graphene-derivative/polysaccharide bionanocomposites: Therapeutics, pharmacogenomics and toxicity, Carbohydr. Polym., 250 (2020) 116952.

[38] H. Li, K. Jin, M. Luo, X. Wang, X. Zhu, X. Liu, T. Jiang, Q. Zhang, S. Wang, Z. Pang, Size Dependency of Circulation and Biodistribution of Biomimetic Nanoparticles: Red Blood Cell Membrane-Coated Nanoparticles, Cells, 8 (2019) 881.

[39] X. Yu, H. Wu, H. Hu, Z. Dong, Y. Dang, Q. Qi, Y. Wang, S. Du, Y. Lu, Zein nanoparticles as nontoxic delivery system for maytansine in the treatment of non-small cell lung cancer, Drug Delivery, 27 (2020) 100-109.

[40] P. Zhao, M. Zheng, C. Yue, Z. Luo, P. Gong, G. Gao, Z. Sheng, C. Zheng, L. Cai, Improving drug accumulation and photothermal efficacy in tumor depending on size of ICG loaded lipid-polymer nanoparticles, Biomaterials, 35 (2014) 6037-6046.

[41] X. Duan, Y. Li, Physicochemical Characteristics of Nanoparticles Affect Circulation, Biodistribution, Cellular Internalization, and Trafficking, Small, 9 (2013) 1521-1532.

[42] R. Zein, W. Sharrouf, K. Selting, Physical Properties of Nanoparticles That Result in Improved Cancer Targeting, J. Oncol., 2020 (2020) 5194780.

[43] M. Saadat, F. Zahednezhad, P. Zakeri-Milani, H. Reza Heidari, J. Shahbazi-Mojarrad, H. Valizadeh, Drug Targeting Strategies Based on Charge Dependent Uptake of Nanoparticles into Cancer Cells, J. Pharm. Pharm. Sci., 22 (2019) 191-220.

[44] T. Shen, S. Guan, Z. Gan, G. Zhang, Q. Yu, Polymeric Micelles with Uniform Surface Properties and Tunable Size and Charge: Positive Charges Improve Tumor Accumulation, Biomacromolecules, 17 (2016) 1801-1810.

[45] T. Osaka, T. Nakanishi, S. Shanmugam, S. Takahama, H. Zhang, Effect of surface charge of magnetite nanoparticles on their internalization into breast cancer and umbilical vein endothelial cells, Colloids Surf., B, 71 (2009) 325-330.

[46] G. Yang, L. Xu, J. Xu, R. Zhang, G. Song, Y. Chao, L. Feng, F. Han, Z. Dong, B. Li, Z. Liu, Smart Nanoreactors for pH-Responsive Tumor Homing, Mitochondria-Targeting, and Enhanced Photodynamic-Immunotherapy of Cancer, Nano Lett., 18 (2018) 2475-2484.

[47] L. Dai, K. Li, M. Li, X. Zhao, Z. Luo, L. Lu, Y. Luo, K. Cai, Size/Charge Changeable Acidity-Responsive Micelleplex for Photodynamic-Improved PD-L1 Immunotherapy with Enhanced Tumor Penetration, Adv. Funct. Mater., 28 (2018) 1707249.

[48] Y. Li, H.Y. Yang, T. Thambi, J.-H. Park, D.S. Lee, Charge-convertible polymers for improved tumor targeting and enhanced therapy, Biomaterials, 217 (2019) 119299.

[49] N.P. Truong, M.R. Whittaker, C.W. Mak, T.P. Davis, The importance of nanoparticle shape in cancer drug delivery, Expert Opin. Drug Delivery, 12 (2015) 129-142.

[50] S. Nejati, E. Mohseni Vadeghani, S. Khorshidi, A. Karkhaneh, Role of particle shape on efficient and organ-based drug delivery, Eur. Polym. J., 122 (2020) 109353.

[51] M. Arnida, A. Ray, C. Peterson, H. Ghandehari, Geometry and surface characteristics of gold nanoparticles influence their biodistribution and uptake by macrophages, Eur. J. Pharm. Biopharm., 77 (2011) 417-423.

[52] Z. Zhou, X. Ma, E. Jin, J. Tang, M. Sui, Y. Shen, E.A. Van Kirk, W.J. Murdoch, M. Radosz, Linear-dendritic drug conjugates forming long-circulating nanorods for cancer-drug delivery, Biomaterials, 34 (2013) 5722-5735.

[53] Y. Li, M. Kröger, W.K. Liu, Shape effect in cellular uptake of PEGylated nanoparticles: comparison between sphere, rod, cube and disk, Nanoscale, 7 (2015) 16631-16646.

[54] J. Zhao, H. Lu, S. Wong, M. Lu, P. Xiao, M.H. Stenzel, Influence of nanoparticle shapes on cellular uptake of paclitaxel loaded nanoparticles in 2D and 3D cancer models, Polym. Chem., 8 (2017) 3317-3326.

[55] A. Gonda, N. Zhao, J.V. Shah, H.R. Calvelli, H. Kantamneni, N.L. Francis, V. Ganapathy, Engineering Tumor-Targeting Nanoparticles as Vehicles for Precision Nanomedicine, Med One, 4 (2019) e190021.

[56] F. Chen, W. Cai, Tumor Vasculature Targeting: A Generally Applicable Approach for Functionalized Nanomaterials, Small, 10 (2014) 1887-1893.

[57] C. Ollauri-Ibáñez, B. Ayuso-Íñigo, M. Pericacho, Hot and Cold Tumors: Is Endoglin (CD105) a Potential Target for Vessel Normalization?, Cancers, 13 (2021) 1552.

[58] F. Khodabakhsh, P. Merikhian, M.R. Eisavand, L. Farahmand, Crosstalk between MUC1 and VEGF in angiogenesis and metastasis: a review highlighting roles of the MUC1 with an emphasis on metastatic and angiogenic signaling, Cancer Cell Int., 21 (2021) 1-11.

[59] M. Fernández, F. Javaid, V. Chudasama, Advances in targeting the folate receptor in the treatment/imaging of cancers, Chem. Sci., 9 (2018) 790-810.

[60] K.R. Kampen, Membrane proteins: the key players of a cancer cell, J. Membr. Biol., 242 (2011) 69-74.

[61] Y. He, C. Xue, Y. Yu, J. Chen, X. Chen, F. Ren, Z. Ren, G. Cui, R. Sun, CD44 is overexpressed and correlated with tumor progression in gallbladder cancer, Cancer Manage. Res., 10 (2018) 3857–3865.

[62] Y. Liu, Y.J. Kim, N. Siriwon, J.A. Rohrs, Z. Yu, P. Wanga, Combination drug delivery via multilamellar vesicles enables targeting of tumor cells and tumor vasculature, Biotechnol. Bioeng., 115 (2018) 1403-1415.

[63] C. Chen, W. Tang, D. Jiang, G. Yang, X. Wang, L. Zhou, W. Zhang, P. Wang, Hyaluronic acid conjugated polydopamine functionalized mesoporous silica nanoparticles for synergistic targeted chemo-photothermal therapy, Nanoscale, 11 (2019) 11012-11024.

[64] Y. He, M. Wang, M. Fu, X. Yuan, Y. Luo, B. Qiao, J. Cao, Z. Wang, L. Hao, G. Yuan, Iron (II) phthalocyanine loaded and AS1411 aptamer targeting nanoparticles: a nanocomplex for dual modal imaging and photothermal therapy of breast cancer, Int. J. Nanomed., 15 (2020) 5927.

[65] J.H. Lee, A. Sahu, C. Jang, G. Tae, The effect of ligand density on in vivo tumor targeting of nanographene oxide, J. Controlled Release, 209 (2015) 219-228.

[66] Z. Liu, W. Cai, L. He, N. Nakayama, K. Chen, X. Sun, X. Chen, H. Dai, In vivo biodistribution and highly efficient tumour targeting of carbon nanotubes in mice, Nat. Nanotechnol., 2 (2007) 47-52.

[67] R. Bazak, M. Houri, S. El Achy, S. Kamel, T. Refaat, Cancer active targeting by nanoparticles: a comprehensive review of literature, J. Cancer Res. Clin. Oncol., 141 (2015) 769-784.

[68] X. Cai, A. Bandla, C.K. Chuan, G. Magarajah, L.-D. Liao, D.B.L. Teh, B.K. Kennedy, N.V. Thakor, B. Liu, Identifying glioblastoma margins using dual-targeted organic

nanoparticles for efficient in vivo fluorescence image-guided photothermal therapy, Mater. Horiz., 6 (2019) 311-317.

[69] S.V. Jenkins, D.A. Nedosekin, B.J. Shaulis, T. Wang, A. Jamshidi-Parsian, E.D. Pollock, J. Chen, R.P. Dings, R.J. Griffin, Enhanced photothermal treatment efficacy and normal tissue protection via vascular targeted gold nanocages, Nanotheranostics, 3 (2019) 145-155.

[70] T. Hao, Y. Fu, Y. Yang, S. Yang, J. Liu, J. Tang, K.A. Ridwan, Y. Teng, Z. Liu, J. Li, N. Guo, P. Yu, Tumor vasculature-targeting PEGylated peptide-drug conjugate prodrug nanoparticles improve chemotherapy and prevent tumor metastasis, Eur. J. Med. Chem., 219 (2021) 113430.

[71] F.S. Mozar, E.H. Chowdhury, Impact of PEGylated Nanoparticles on Tumor Targeted Drug Delivery, Curr. Pharm. Des., 24 (2018) 3283-3296.

[72] P. Sabourian, G. Yazdani, S.S. Ashraf, M. Frounchi, S. Mashayekhan, S. Kiani, A. Kakkar, Effect of Physico-Chemical Properties of Nanoparticles on Their Intracellular Uptake, Int. J. Mol. Sci., 21 (2020) 8019.

[73] X. Bai, J. Wang, Q. Mu, G. Su, In vivo Protein Corona Formation: Characterizations, Effects on Engineered Nanoparticles' Biobehaviors, and Applications, Front. Bioeng. Biotechnol., 9 (2021) 2296-4185

[74] Z. Ashikbayeva, D. Tosi, D. Balmassov, E. Schena, P. Saccomandi, V. Inglezakis, Application of Nanoparticles and Nanomaterials in Thermal Ablation Therapy of Cancer, Nanomaterials, 9 (2019) 1195.

[75] Z. Hussain, S. Khan, M. Imran, M. Sohail, S.W.A. Shah, M. de Matas, PEGylation: a promising strategy to overcome challenges to cancer-targeted nanomedicines: a review of challenges to clinical transition and promising resolution, Drug Delivery Transl. Res., 9 (2019) 721-734.

[76] C. Teng, Z. Chai, Z. Yuan, L. Ren, C. Lin, Z. Yan, W. He, C. Qin, L. Yang, X. Han, L. Yin, Desirable PEGylation for improving tumor selectivity of hyaluronic acid-based nanoparticles via low hepatic captured, long circulation times and CD44 receptor-mediated tumor targeting, Nanomed.: Nanotechnol. Biol. Med., 24 (2020) 102105.

[77] R. Taléns-Visconti, O. Díez-Sales, J.V. de Julián-Ortiz, A. Nácher, Nanoliposomes in Cancer Therapy: Marketed Products and Current Clinical Trials, Int. J. Mol. Sci., 23 (2022) 4249.

[78] R. Wang, J. Deng, D. He, E. Yang, W. Yang, D. Shi, Y. Jiang, Z. Qiu, T.J. Webster, Y. Shen, PEGylated hollow gold nanoparticles for combined X-ray radiation and

photothermal therapy in vitro and enhanced CT imaging in vivo, Nanomed.: Nanotechnol. Biol. Med., 16 (2019) 195-205.

[79] H. Liu, T.L. Doane, Y. Cheng, F. Lu, S. Srinivasan, J.-J. Zhu, C. Burda, Control of Surface Ligand Density on PEGylated Gold Nanoparticles for Optimized Cancer Cell Uptake, Part. Part. Syst. Charact., 32 (2015) 197-204.

[80] V. Patsula, D. Horák, J. Kučka, H. Macková, V. Lobaz, P. Francová, V. Herynek, T. Heizer, P. Páral, L. Šefc, Synthesis and modification of uniform PEG-neridronate-modified magnetic nanoparticles determines prolonged blood circulation and biodistribution in a mouse preclinical model, Sci. Rep., 9 (2019) 1-12.

[81] N. d'Avanzo, C. Celia, A. Barone, M. Carafa, L. Di Marzio, H.A. Santos, M. Fresta, Immunogenicity of polyethylene glycol based nanomedicines: mechanisms, clinical implications and systematic approach, Adv. Ther., 3 (2020) 1900170.

[82] X. Wan, J. Zhang, W. Yu, L. Shen, S. Ji, T. Hu, Effect of protein immunogenicity and PEG size and branching on the anti-PEG immune response to PEGylated proteins, Process Biochem., 52 (2017) 183-191.

[83] R. Saadati, S. Dadashzadeh, Z. Abbasian, H. Soleimanjahi, Accelerated Blood Clearance of PEGylated PLGA Nanoparticles Following Repeated Injections: Effects of Polymer Dose, PEG Coating, and Encapsulated Anticancer Drug, Pharm. Res., 30 (2013) 985-995.

[84] A. Chanan-Khan, J. Szebeni, S. Savay, L. Liebes, N. Rafique, C. Alving, F. Muggia, Complement activation following first exposure to pegylated liposomal doxorubicin (Doxil®): possible role in hypersensitivity reactions, Ann. Oncol., 14 (2003) 1430-1437.

[85] M. Estapé Senti, C.A. de Jongh, K. Dijkxhoorn, J.J.F. Verhoef, J. Szebeni, G. Storm, C.E. Hack, R.M. Schiffelers, M.H. Fens, P. Boross, Anti-PEG antibodies compromise the integrity of PEGylated lipid-based nanoparticles via complement, J. Controlled Release, 341 (2022) 475-486.

[86] T.T. Hoang Thi, E.H. Pilkington, D.H. Nguyen, J.S. Lee, K.D. Park, N.P. Truong, The importance of poly (ethylene glycol) alternatives for overcoming PEG immunogenicity in drug delivery and bioconjugation, Polymers, 12 (2020) 298.

[87] R. Rampado, S. Crotti, P. Caliceti, S. Pucciarelli, M. Agostini, Recent Advances in Understanding the Protein Corona of Nanoparticles and in the Formulation of “Stealthy” Nanomaterials, Front. Bioeng. Biotechnol., 8 (2020).

[88] M. Mohamed, A.S. Abu Lila, T. Shimizu, E. Alaaeldin, A. Hussein, H.A. Sarhan, J. Szebeni, T. Ishida, PEGylated liposomes: immunological responses, Sci. Technol. Adv. Mater., 20 (2019) 710-724.

[89] J.A. Gnoatto, A.M. Morás, J. Vitor de Oliveira, E. Arndt, A. Dallegrave, A.C. Borba da Cunha, D.J. Moura, J.H. Zimnoch dos Santos, PEGylated and zwitterated silica nanoparticles as doxorubicin carriers applied in a breast cancer cell line: Effects on protein corona formation, J. Drug Delivery Sci. Technol., 71 (2022) 103325.

[90] R. Li, M. Elsabahy, Y. Song, H. Wang, L. Su, R.A. Letteri, S. Khan, G.S. Heo, G. Sun, Y. Liu, K.L. Wooley, Functional, Degradable Zwitterionic Polyphosphoesters as Biocompatible Coating Materials for Metal Nanostructures, Langmuir, 35 (2019) 1503-1512.

[91] M. Harijan, M. Singh, Zwitterionic polymers in drug delivery: A review, J. Mol. Recognit., 35 (2022) e2944.

[92] Z. Xiong, M. Shen, X. Shi, Zwitterionic Modification of Nanomaterials for Improved Diagnosis of Cancer Cells, Bioconjugate Chem., 30 (2019) 2519-2527.

[93] W. Yang, L. Zhang, S. Wang, A.D. White, S. Jiang, Functionalizable and ultra stable nanoparticles coated with zwitterionic poly(carboxybetaine) in undiluted blood serum, Biomaterials, 30 (2009) 5617-5621.

[94] G. Zhao, X. Dong, Y. Sun, Self-assembled curcumin–poly (carboxybetaine methacrylate) conjugates: potent nano-inhibitors against amyloid β-protein fibrillogenesis and cytotoxicity, Langmuir, 35 (2018) 1846-1857.

[95] J. Xiang, Y. Bai, Y. Huang, S. Lang, J. Li, Y. Ji, B. Peng, G. Liu, A zwitterionic silver nanoparticle-incorporating injectable hydrogel with a durable and efficient antibacterial effect for accelerated wound healing, J. Mater. Chem. B, (2022).

[96] S. Peng, B. Ouyang, Y. Men, Y. Du, Y. Cao, R. Xie, Z. Pang, S. Shen, W. Yang, Biodegradable zwitterionic polymer membrane coating endowing nanoparticles with ultra-long circulation and enhanced tumor photothermal therapy, Biomaterials, 231 (2020) 119680.

[97] Y. Han, Z. Yuan, P. Zhang, S. Jiang, Zwitterlation mitigates protein bioactivity loss in vitro over PEGylation, Chem. Sci., 9 (2018) 8561-8566.

[98] Y. Men, S. Peng, P. Yang, Q. Jiang, Y. Zhang, B. Shen, P. Dong, Z. Pang, W. Yang, Biodegradable zwitterionic nanogels with long circulation for antitumor drug delivery, ACS Appl. Mater. Interfaces, 10 (2018) 23509-23521.

[99] X. Guo, S. Li, J. Tian, S. Chen, G. Ma, H. Xiao, Z. Liu, L. Wang, X. Jiang, Long-circulation zwitterionic dendrimer nanodrugs for phototherapy of tumors, Colloids Surf., B, 217 (2022) 112681.

[100] K. Knop, R. Hoogenboom, D. Fischer, U.S. Schubert, Poly(ethylene glycol) in Drug Delivery: Pros and Cons as Well as Potential Alternatives, Angew. Chem., Int. Ed., 49 (2010) 6288-6308.

[101] Z. Chen, R.M. Visalakshan, J. Guo, F. Wei, L. Zhang, L. Chen, Z. Lin, K. Vasilev, Y. Xiao, Plasma deposited poly-oxazoline nanotextured surfaces dictate osteoimmunomodulation towards ameliorative osteogenesis, Acta Biomater., 96 (2019) 568-581.

[102] S. Deodhar, A.K. Dash, Long circulating liposomes: challenges and opportunities, Ther. Delivery, 9 (2018) 857-872.

[103] O. Koshkina, D. Westmeier, T. Lang, C. Bantz, A. Hahlbrock, C. Würth, U. Resch-Genger, U. Braun, R. Thiermann, C. Weise, M. Eravci, B. Mohr, H. Schlaad, R.H. Stauber, D. Docter, A. Bertin, M. Maskos, Tuning the Surface of Nanoparticles: Impact of Poly(2-ethyl-2-oxazoline) on Protein Adsorption in Serum and Cellular Uptake, Macromol. Biosci., 16 (2016) 1287-1300.

[104] Z. He, X. Wan, A. Schulz, H. Bludau, M.A. Dobrovolskaia, S.T. Stern, S.A. Montgomery, H. Yuan, Z. Li, D. Alakhova, M. Sokolsky, D.B. Darr, C.M. Perou, R. Jordan, R. Luxenhofer, A.V. Kabanov, A high capacity polymeric micelle of paclitaxel: Implication of high dose drug therapy to safety and in vivo anti-cancer activity, Biomaterials, 101 (2016) 296-309.

[105] R.W. Moreadith, T.X. Viegas, M.D. Bentley, J.M. Harris, Z. Fang, K. Yoon, B. Dizman, R. Weimer, B.P. Rae, X. Li, C. Rader, D. Standaert, W. Olanow, Clinical development of a poly(2-oxazoline) (POZ) polymer therapeutic for the treatment of Parkinson's disease – Proof of concept of POZ as a versatile polymer platform for drug development in multiple therapeutic indications, Eur. Polym. J., 88 (2017) 524-552.

[106] N. Gao, C. Xing, H. Wang, L. Feng, X. Zeng, L. Mei, Z. Peng, pH-Responsive Dual Drug-Loaded Nanocarriers Based on Poly (2-Ethyl-2-Oxazoline) Modified Black Phosphorus Nanosheets for Cancer Chemo/Photothermal Therapy, Front. Pharmacol., 10 (2019).

[107] S. Dong, S. Ma, H. Chen, Z. Tang, W. Song, M. Deng, Nucleobase-crosslinked poly(2-oxazoline) nanoparticles as paclitaxel carriers with enhanced stability and ultra-high drug loading capacity for breast cancer therapy, Asian J. Pharm. Sci., 17 (2022) 571-582.

[108] M. Xu, C. Yao, W. Zhang, S. Gao, H. Zou, J. Gao, Anti-Cancer Activity Based on the High Docetaxel Loaded Poly (2-Oxazoline) s Micelles, Int. J. Nanomed., 16 (2021) 2735–2749.

[109] Z. Li, Y. Yang, H. Wei, X. Shan, X. Wang, M. Ou, Q. Liu, N. Gao, H. Chen, L. Mei, X. Zeng, Charge-reversal biodegradable MSNs for tumor synergetic chemo/photothermal and visualized therapy, J. Controlled Release, 338 (2021) 719-730.

[110] D. Pizzi, A.M. Mahmoud, T. Klein, J.P. Morrow, J. Humphries, Z.H. Houston, N.L. Fletcher, C.A. Bell, K.J. Thurecht, K. Kempe, Poly(2-ethyl-2-oxazoline) bottlebrushes: How nanomaterial dimensions can influence biological interactions, Eur. Polym. J., 151 (2021) 110447.

[111] L. Wen, S. Huang, W. Du, C. Zhu, H. Xu, Effects of the molecular weight and molar ratio of poly (2-ethyl-2-oxazoline)-based lipid on the pH sensitivity, stability, and antitumor efficacy of liposomes, Drug Dev. Ind. Pharm., 46 (2020) 283-295.

[112] J. Wang, X. Wu, P. Shen, J. Wang, Y. Shen, Y. Shen, T.J. Webster, J. Deng, Applications of Inorganic Nanomaterials in Photothermal Therapy Based on Combinational Cancer Treatment, Int. J. Nanomed., 15 (2020) 1903-1914.

[113] H. Wang, J. Chang, M. Shi, W. Pan, N. Li, B. Tang, A Dual-Targeted Organic Photothermal Agent for Enhanced Photothermal Therapy, Angew. Chem., Int. Ed., 58 (2019) 1057-1061.

[114] P. Gao, H. Wang, Y. Cheng, Strategies for efficient photothermal therapy at mild temperatures: Progresses and challenges, Chin. Chem. Lett., 33 (2022) 575-586.

[115] R. Yin, T. Dai, P. Avci, A.E.S. Jorge, W.C.M.A. de Melo, D. Vecchio, Y.-Y. Huang, A. Gupta, M.R. Hamblin, Light based anti-infectives: ultraviolet C irradiation, photodynamic therapy, blue light, and beyond, Curr. Opin. Pharmacol., 13 (2013) 731-762.

[116] Z. Shah, S. Nazir, K. Mazhar, R. Abbasi, I.M. Samokhvalov, PEGylated doped- and undoped-TiO2 nanoparticles for photodynamic Therapy of cancers, Photodiagn. Photodyn. Ther., 27 (2019) 173-183.

[117] Y. Tang, G. Wang, NIR light-responsive nanocarriers for controlled release, J. Photochem. Photobiol., C, 47 (2021) 100420.

[118] C. Song, Y. Li, T. Li, Y. Yang, Z. Huang, J.M. de la Fuente, J. Ni, D. Cui, Long-Circulating Drug-Dye-Based Micelles with Ultrahigh pH-Sensitivity for Deep Tumor Penetration and Superior Chemo-Photothermal Therapy, Adv. Funct. Mater., 30 (2020) 1906309.

[119] H. Liu, H. Chen, X. Liu, L. Mo, C. Chen, Z. Guo, Z. Liu, Dual-responsive ultrathin 1T-phase niobium telluride nanosheet-based delivery systems for enhanced chemo-photothermal therapy, J. Mater. Chem. B, 9 (2021) 8109-8120.

[120] Y. Zhang, F. Fang, Y. Chen, M. Li, L. Li, W. Li, J. Zhang, Hollow mesoporous polyaniline nanoparticles with high drug payload and robust photothermal capability for cancer combination therapy, Chin. J. Chem. Eng., 38 (2021) 221-228.

[121] L. Fu, S. Yang, S. Jiang, X. Zhou, Z. Sha, C. He, One-step synthesis of multifunctional nanoparticles for CT/PA imaging guided breast cancer photothermal therapy, Colloids Surf., B, 201 (2021) 111630.

[122] K. Yang, H. Xu, L. Cheng, C. Sun, J. Wang, Z. Liu, In Vitro and In Vivo Near-Infrared Photothermal Therapy of Cancer Using Polypyrrole Organic Nanoparticles, Adv. Mater., 24 (2012) 5586-5592.

[123] Q. Zou, J. Huang, X. Zhang, One-Step Synthesis of Iodinated Polypyrrole Nanoparticles for CT Imaging Guided Photothermal Therapy of Tumors, Small, 14 (2018) 1803101.

[124] H. Liu, M. Zhang, H. Jin, K. Tao, C. Tang, Y. Fan, S. Liu, Y. Liu, Y. Hou, H. Zhang, Fe(III)-Doped Polyaminopyrrole Nanoparticle for Imaging-Guided Photothermal Therapy of Bladder Cancer, ACS Biomater. Sci. Eng., 8 (2022) 502-511.

[125] Y. Wang, K.C.L. Black, H. Luehmann, W. Li, Y. Zhang, X. Cai, D. Wan, S.-Y. Liu, M. Li, P. Kim, Z.-Y. Li, L.V. Wang, Y. Liu, Y. Xia, Comparison Study of Gold Nanohexapods, Nanorods, and Nanocages for Photothermal Cancer Treatment, ACS Nano, 7 (2013) 2068-2077.

[126] J. Shao, H. Xie, H. Huang, Z. Li, Z. Sun, Y. Xu, Q. Xiao, X.-F. Yu, Y. Zhao, H. Zhang, Biodegradable black phosphorus-based nanospheres for in vivo photothermal cancer therapy, Nat. Commun., 7 (2016) 1-13.

[127] C.G. Alves, D. de Melo-Diogo, R. Lima-Sousa, E.C. Costa, I.J. Correia, Hyaluronic acid functionalized nanoparticles loaded with IR780 and DOX for cancer chemo-photothermal therapy, Eur. J. Pharm. Biopharm., 137 (2019) 86-94.

[128] D. Kim, H. Kim, Optimization of Photothermal Therapy Treatment Effect under Various Laser Irradiation Conditions, Int. J. Mol. Sci., 23 (2022) 5928.

[129] Y. Ren, Y. Yan, H. Qi, Photothermal conversion and transfer in photothermal therapy: From macroscale to nanoscale, Adv. Colloid Interface Sci., 308 (2022) 102753.

[130] H.S. Jung, P. Verwilst, A. Sharma, J. Shin, J.L. Sessler, J.S. Kim, Organic molecule-based photothermal agents: an expanding photothermal therapy universe, Chem. Soc. Rev., 47 (2018) 2280-2297.

[131] Y. Wang, H.-M. Meng, Z. Li, Near-infrared inorganic nanomaterial-based nanosystems for photothermal therapy, Nanoscale, 13 (2021) 8751-8772.

[132] S. Li, C. Cao, J. Gao, K. Li, J. Kang, D. Wu, Y. Kong, Dual stimuli-responsive nanoplatform based on core-shell structured graphene oxide/mesoporous silica@alginate, Int. J. Biol. Macromol., 175 (2021) 209-216.

[133] X. Wei, P. Li, H. Zhou, X. Hu, D. Liu, J. Wu, Y. Wang, Engineering of gemcitabine coated nano-graphene oxide sheets for efficient near-infrared radiation mediated in vivo lung cancer photothermal therapy, J. Photochem. Photobiol., B, 216 (2021) 112125.

[134] B.S. Dash, Y.-J. Lu, H.-A. Chen, C.-C. Chuang, J.-P. Chen, Magnetic and GRPR-targeted reduced graphene oxide/doxorubicin nanocomposite for dual-targeted chemo-photothermal cancer therapy, Mater. Sci. Eng., C, 128 (2021) 112311.

[135] X. Chen, Z. Qu, Z. Liu, G. Ren, Mechanism of Oxidization of Graphite to Graphene Oxide by the Hummers Method, ACS Omega, 7 (2022) 23503-23510.

[136] J. Chen, B. Yao, C. Li, G. Shi, An improved Hummers method for eco-friendly synthesis of graphene oxide, Carbon, 64 (2013) 225-229.

[137] D.C. Marcano, D.V. Kosynkin, J.M. Berlin, A. Sinitskii, Z. Sun, A. Slesarev, L.B. Alemany, W. Lu, J.M. Tour, Improved Synthesis of Graphene Oxide, ACS Nano, 4 (2010) 4806-4814.

[138] G. Santamaría-Juárez, E. Gómez-Barojas, E. Quiroga-González, E. Sánchez-Mora, M. Quintana-Ruiz, J.D. Santamaría-Juárez, Safer modified Hummers' method for the synthesis of graphene oxide with high quality and high yield, Mater. Res. Express, 6 (2020) 125631.

[139] Y. Hu, D. Sun, J. Ding, L. Chen, X. Chen, Decorated reduced graphene oxide for photo-chemotherapy, J. Mater. Chem. B, 4 (2016) 929-937.

[140] R. Lima-Sousa, D. de Melo-Diogo, C.G. Alves, E.C. Costa, P. Ferreira, R.O. Louro, I.J. Correia, Hyaluronic acid functionalized green reduced graphene oxide for targeted cancer photothermal therapy, Carbohydr. Polym., 200 (2018) 93-99.

[141] R. Al-Gaashani, A. Najjar, Y. Zakaria, S. Mansour, M.A. Atieh, XPS and structural studies of high quality graphene oxide and reduced graphene oxide prepared by different chemical oxidation methods, Ceram. Int., 45 (2019) 14439-14448.

[142] G. Behbudi, Mini review of Graphene Oxide for medical detection and applications, Adv. Appl. NanoBio-Technol., 1 (2020) 63-66.

[143] J. Rico, M. Castaño-Soto, N. Lopez-Arango, Y. Hernandez, Influence of C=O groups on the optical extinction coefficient of graphene exfoliated in liquid phase, J. Phys.: Condens. Matter, 34 (2021) 105701.

[144] C. Xiong, Q. Yang, W. Dang, M. Li, B. Li, J. Su, Y. Liu, W. Zhao, C. Duan, L. Dai, Fabrication of eco-friendly carbon microtubes@ nitrogen-doped reduced graphene oxide hybrid as an excellent carbonaceous scaffold to load MnO2 nanowall (PANI nanorod) as bifunctional material for high-performance supercapacitor and oxygen reduction reaction catalyst, J. Power Sources, 447 (2020) 227387.

[145] S. Roy, A. Sarkar, A. Jaiswal, Poly (allylamine hydrochloride)-functionalized reduced graphene oxide for synergistic chemo-photothermal therapy, Nanomedicine, 14 (2019) 255-274.

[146] W.-J. Chiu, Y.-C. Chen, C.-C. Huang, L. Yang, J. Yu, S.-W. Huang, C.-H. Lin, Iron Hydroxide/Oxide-Reduced Graphene Oxide Nanocomposite for Dual-Modality Photodynamic and Photothermal Therapy In Vitro and In Vivo, Nanomaterials, 11 (2021) 1947.

[147] K. Yang, J. Wan, S. Zhang, B. Tian, Y. Zhang, Z. Liu, The influence of surface chemistry and size of nanoscale graphene oxide on photothermal therapy of cancer using ultra-low laser power, Biomaterials, 33 (2012) 2206-2214.

[148] S. Pei, H.-M. Cheng, The reduction of graphene oxide, Carbon, 50 (2012) 3210-3228.

[149] B.S. Dash, G. Jose, Y.-J. Lu, J.-P. Chen, Functionalized Reduced Graphene Oxide as a Versatile Tool for Cancer Therapy, Int. J. Mol. Sci., 22 (2021) 2989.

[150] A.D. Sontakke, M.K. Purkait, A brief review on graphene oxide Nanoscrolls: Structure, Synthesis, characterization and scope of applications, Chem. Eng. J., 420 (2021) 129914.

[151] B.L. Melo, R. Lima-Sousa, C.G. Alves, P. Ferreira, A.F. Moreira, I.J. Correia, D.d. Melo-Diogo, Sulfobetaine methacrylate-albumin-coated graphene oxide incorporating IR780 for enhanced breast cancer phototherapy, Nanomedicine, 16 (2021) 453-464.

[152] S.W. Jun, P. Manivasagan, J. Kwon, V.T. Nguyen, S. Mondal, C.D. Ly, J. Lee, Y.-H. Kang, C.-S. Kim, J. Oh, Folic acid–conjugated chitosan-functionalized graphene oxide for highly efficient photoacoustic imaging-guided tumor-targeted photothermal therapy, Int. J. Biol. Macromol., 155 (2020) 961-971.

[153] J.B. Vines, J.-H. Yoon, N.-E. Ryu, D.-J. Lim, H. Park, Gold Nanoparticles for Photothermal Cancer Therapy, Front. Chem., 7 (2019) 2296-2646

[154] A.V. Simakin, M.E. Astashev, I.V. Baimler, O.V. Uvarov, V.V. Voronov, M.V. Vedunova, M.A. Sevost'yanov, K.N. Belosludtsev, S.V. Gudkov, The Effect of Gold Nanoparticle Concentration and Laser Fluence on the Laser-Induced Water Decomposition, J. Phys. Chem. B, 123 (2019) 1869-1880.

[155] I.O. Silva, R. Ladchumananandasivam, J.H.O. Nascimento, K.K.O. Silva, F.R. Oliveira, A.P. Souto, H.P. Felgueiras, A. Zille, Multifunctional chitosan/gold nanoparticles coatings for biomedical textiles, Nanomaterials, 9 (2019) 1064.

[156] J.E. Ortiz-Castillo, R.C. Gallo-Villanueva, M.J. Madou, V.H. Perez-Gonzalez, Anisotropic gold nanoparticles: A survey of recent synthetic methodologies, Coord. Chem. Rev., 425 (2020) 213489.

[157] W. Yang, H. Liang, S. Ma, D. Wang, J. Huang, Gold nanoparticle based photothermal therapy: Development and application for effective cancer treatment, Sustainable Mater. Technol., 22 (2019) e00109.

[158] W. Yang, B. Xia, L. Wang, S. Ma, H. Liang, D. Wang, J. Huang, Shape effects of gold nanoparticles in photothermal cancer therapy, Mater. Today Sustain., 13 (2021) 100078.

[159] V. Amendola, R. Pilot, M. Frasconi, O.M. Maragò, M.A. Iatì, Surface plasmon resonance in gold nanoparticles: a review, J. Phys.: Condens. Matter, 29 (2017) 203002.

[160] C. Kohout, C. Santi, L. Polito, Anisotropic gold nanoparticles in biomedical applications, Int. J. Mol. Sci., 19 (2018) 3385.

[161] Y. Liu, B.M. Crawford, T. Vo-Dinh, Gold nanoparticles-mediated photothermal therapy and immunotherapy, Immunotherapy, 10 (2018) 1175-1188.

[162] S. Ishtiaq, K.U. Shah, T. Ur-Rehman, F. Ud-Din, Gold nanorods: New generation drug delivery platform, Met. Nanopart. Drug Delivery Diagn. Appl., (2020) 59-84.

[163] S.E. Lohse, C.J. Murphy, The Quest for Shape Control: A History of Gold Nanorod Synthesis, Chem. Mater., 25 (2013) 1250-1261.

[164] S.E. Skrabalak, J. Chen, Y. Sun, X. Lu, L. Au, C.M. Cobley, Y. Xia, Gold nanocages: synthesis, properties, and applications, Acc. Chem. Res., 41 (2008) 1587-1595.

[165] X. Li, H. Liu, J. Yang, S.-Z. Qiao, X.-W. Du, Pure gold nanocages by galvanic replacement reaction of magnesium nanoparticles, RSC Adv., 4 (2014) 1185-1188.

[166] T.T.V. Phan, S.-H. Ahn, J. Oh, Chitosan-mediated facile green synthesis of size-controllable gold nanostars for effective photothermal therapy and photoacoustic imaging, Eur. Polym. J., 118 (2019) 492-501.

[167] C.M. Otero, G.B. Simal, M.F. Scocozza, A. Rubert, C.A. Grillo, L. Hannibal, G. Lavorato, M.A. Huergo, D.H. Murgida, C. Vericat, Optimized Biocompatible Gold Nanotriangles with NIR Absorption for Photothermal Applications, ACS Appl. Nano Mater., 5 (2022) 341-350.

[168] S.J. Amina, B. Guo, A Review on the Synthesis and Functionalization of Gold Nanoparticles as a Drug Delivery Vehicle, Int. J. Nanomed., 15 (2020) 9823-9857.

[169] P. Singh, S. Pandit, V.R.S.S. Mokkapati, A. Garg, V. Ravikumar, I. Mijakovic, Gold Nanoparticles in Diagnostics and Therapeutics for Human Cancer, Int. J. Mol. Sci., 19 (2018) 1979.

[170] A.F. Moreira, C.F. Rodrigues, C.A. Reis, E.C. Costa, I.J. Correia, Gold-core silica shell nanoparticles application in imaging and therapy: A review, Microporous Mesoporous Mater., 270 (2018) 168-179.

[171] A. García, B. González, C. Harvey, I. Izquierdo-Barba, M. Vallet-Regí, Effective reduction of biofilm through photothermal therapy by gold core@ shell based mesoporous silica nanoparticles, Microporous Mesoporous Mater., 328 (2021) 111489.

[172] S.-h. Huang, S. Peng, Q.-y. Wang, Q.-h. Hu, R.-q. Zhang, L. Liu, Q. Liu, J. Lin, Q.-h. Zhou, Gold nanorods conjugated with biocompatible zwitterionic polypeptide for combined chemo-photothermal therapy of cervical cancer, Colloids Surf., B, 207 (2021) 112014.

[173] A.F. Moreira, C.F. Rodrigues, C.A. Reis, E.C. Costa, P. Ferreira, I.J. Correia, Development of poly-2-ethyl-2-oxazoline coated gold-core silica shell nanorods for cancer chemo-photothermal therapy, Nanomedicine, 13 (2018) 2611-2627.

[174] M. Jeon, G. Kim, W. Lee, S. Baek, H.N. Jung, H.-J. Im, Development of theranostic dual-layered Au-liposome for effective tumor targeting and photothermal therapy, J. Nanobiotechnol., 19 (2021) 1-16.

[175] H. Chen, X. Zhang, S. Dai, Y. Ma, S. Cui, S. Achilefu, Y. Gu, Multifunctional Gold Nanostar Conjugates for Tumor Imaging and Combined Photothermal and Chemo-therapy, Theranostics, 3 (2013) 633-649.

[176] L. Wang, Synthetic methods of CuS nanoparticles and their applications for imaging and cancer therapy, RSC Adv., 6 (2016) 82596-82615.

[177] F. Castillón-Barraza, M. Farías, J. Coronado-López, M. Encinas-Romero, M. Pérez-Tello, R. Herrera-Urbina, A. Posada-Amarillas, Synthesis and characterization of copper sulfide nanoparticles obtained by the polyol method, Adv. Sci. Lett., 4 (2011) 596-601.

[178] A. Yuliandini, A.B.D. Nandiyanto, Engineering and Economic Perspective in The Production of Cu Nano, Berkala Sainstek, 8 (2020) 15-19.

[179] S. Goel, F. Chen, W. Cai, Synthesis and Biomedical Applications of Copper Sulfide Nanoparticles: From Sensors to Theranostics, Small, 10 (2014) 631-645.

[180] J. Li, Q. Cheng, L. Yue, C. Gao, J. Wei, Y. Ding, Y. Wang, Y. Zheng, R. Wang, Macrophage-hitchhiking supramolecular aggregates of CuS nanoparticles for enhanced tumor deposition and photothermal therapy, Nanoscale Horiz., 6 (2021) 907-912.

[181] L. Wang, X. Xu, X. Mu, Q. Han, J. Liu, J. Feng, P. Zhang, Q. Yuan, Fe-doped copper sulfide nanoparticles for in vivo magnetic resonance imaging and simultaneous photothermal therapy, Nanotechnology, 30 (2019) 415101.

[182] G. Liang, X. Jin, H. Qin, D. Xing, Glutathione-capped, renal-clearable CuS nanodots for photoacoustic imaging and photothermal therapy, J. Mater. Chem. B, 5 (2017) 6366-6375.

[183] N. Li, Q. Sun, Z. Yu, X. Gao, W. Pan, X. Wan, B. Tang, Nuclear-Targeted Photothermal Therapy Prevents Cancer Recurrence with Near-Infrared Triggered Copper Sulfide Nanoparticles, ACS Nano, 12 (2018) 5197-5206.

[184] H. Wu, P. Jia, Y. Zou, J. Jiang, Cascade targeting tumor mitochondria with CuS nanoparticles for enhanced photothermal therapy in the second near-infrared window, Biomater. Sci., 9 (2021) 5209-5217.

[185] B. Jang, M.S. Moorthy, P. Manivasagan, L. Xu, K. Song, K.D. Lee, M. Kwak, J. Oh, J.-O. Jin, Fucoidan-coated CuS nanoparticles for chemo-and photothermal therapy against cancer, Oncotarget, 9 (2018) 12649–12661.

[186] H. Cai, X. Dai, X. Guo, L. Zhang, K. Cao, F. Yan, B. Ji, Y. Liu, Ataxia telangiectasia mutated inhibitor-loaded copper sulfide nanoparticles for low-temperature photothermal therapy of hepatocellular carcinoma, Acta Biomater., 127 (2021) 276-286.

[187] S. Niu, X. Zhang, G.R. Williams, J. Wu, F. Gao, Z. Fu, X. Chen, S. Lu, L.-M. Zhu, Hollow Mesoporous Silica Nanoparticles Gated by Chitosan-Copper Sulfide Composites as Theranostic Agents for the Treatment of Breast Cancer, Acta Biomater., 126 (2021) 408-420.

[188] S.A. Han, R. Bhatia, S.-W. Kim, Synthesis, properties and potential applications of two-dimensional transition metal dichalcogenides, Nano Convergence, 2 (2015) 17.

[189] L. Mei, X. Gao, Z. Gao, Q. Zhang, X. Yu, A.L. Rogach, Z. Zeng, Size-selective synthesis of platinum nanoparticles on transition-metal dichalcogenides for the hydrogen evolution reaction, Chem. Commun., 57 (2021) 2879-2882.

[190] J. Luo, M. Fan, L. Xiong, Q. Hao, M. Jiang, Q. He, C. Su, 1T-Phase Dirac Semimetal PdTe2 Nanoparticles for Efficient Photothermal Therapy in the NIR-II Biowindow, ACS Appl. Mater. Interfaces, 13 (2021) 27963-27971.

[191] L. Cai, L. Dong, X. Sha, S. Zhang, S. Liu, X. Song, M. Zhao, Q. Wang, K. Xu, J. Li, Exfoliation and in situ functionalization of MoS2 nanosheets for MRI-guided combined low-temperature photothermal therapy and chemotherapy, Mater. Des., 210 (2021) 110020.

[192] H. Liu, Z. Liu, X. Liu, H. Zhong, L. Mo, C. Chen, Z. Guo, B. Ye, Facile synthesis of tannic acid modified NbTe2 nanosheets for effective photothermal ablation of bacterial pathogens, Colloid Interface Sci. Commun., 41 (2021) 100383.

[193] J. Kim, H. Kim, W.J. Kim, Single-Layered MoS2–PEI–PEG Nanocomposite-Mediated Gene Delivery Controlled by Photo and Redox Stimuli, Small, 12 (2016) 1184-1192.

[194] C. Lin, H. Hao, L. Mei, M. Wu, Metal-free two-dimensional nanomaterial-mediated photothermal tumor therapy, Smart Mater. Struct., 1 (2020) 150-167.

[195] T. Liu, S. Shi, C. Liang, S. Shen, L. Cheng, C. Wang, X. Song, S. Goel, T.E. Barnhart, W. Cai, Z. Liu, Iron Oxide Decorated MoS2 Nanosheets with Double PEGylation for Chelator-Free Radiolabeling and Multimodal Imaging Guided Photothermal Therapy, ACS Nano, 9 (2015) 950-960.

[196] S.K. Lee, D. Chu, J. Yoo, E.K. Kim, Formation of transition metal dichalcogenides thin films with liquid phase exfoliation technique and photovoltaic applications, Sol. Energy Mater. Sol. Cells, 184 (2018) 9-14.

[197] J. Zhang, T. Ji, H. Jin, Z. Wang, M. Zhao, D. He, G. Luo, B. Mao, Mild Liquid-Phase Exfoliation of Transition Metal Dichalcogenide Nanosheets for Hydrogen Evolution, ACS Appl. Nano Mater., 5 (2022) 8020-8028.

[198] J. You, M.D. Hossain, Z. Luo, Synthesis of 2D transition metal dichalcogenides by chemical vapor deposition with controlled layer number and morphology, Nano Convergence, 5 (2018) 26.

[199] S. Wang, J.-K. Huang, M. Li, A. Azam, X. Zu, L. Qiao, J. Yang, S. Li, Growth of high-quality monolayer transition metal dichalcogenide nanocrystals by chemical vapor

deposition and their photoluminescence and electrocatalytic properties, ACS Appl. Mater. Interfaces, 13 (2021) 47962-47971.

[200] N. Joshi, T. Hayasaka, Y. Liu, H. Liu, O.N. Oliveira, L. Lin, A review on chemiresistive room temperature gas sensors based on metal oxide nanostructures, graphene and 2D transition metal dichalcogenides, Microchim. Acta, 185 (2018) 213.

[201] L. Gong, L. Yan, R. Zhou, J. Xie, W. Wu, Z. Gu, Two-dimensional transition metal dichalcogenide nanomaterials for combination cancer therapy, J. Mater. Chem. B, 5 (2017) 1873-1895.

[202] L. Cheng, J. Liu, X. Gu, H. Gong, X. Shi, T. Liu, C. Wang, X. Wang, G. Liu, H. Xing, W. Bu, B. Sun, Z. Liu, PEGylated WS2 Nanosheets as a Multifunctional Theranostic Agent for in vivo Dual-Modal CT/Photoacoustic Imaging Guided Photothermal Therapy, Adv. Mater., 26 (2014) 1886-1893.

[203] Y. Yu, B. Chi, L. Lin, Z. Yang, Q. He, Z. Xu, C. Yi, J. Wang, Microwave-assisted preparation of paramagnetic zwitterionic amphiphilic copolymer hybrid molybdenum disulfide for T1-weighted magnetic resonance imaging-guided photothermal therapy, J. Mater. Chem. B, 6 (2018) 6391-6398.

[204] S. Zhou, X. Jiao, Y. Jiang, Y. Zhao, P. Xue, Y. Liu, J. Liu, Engineering Eu3+-incorporated MoS2 nanoflowers toward efficient photothermal/photodynamic combination therapy of breast cancer, Appl. Surf. Sci., 552 (2021) 149498.

[205] Y. Wu, Y. Huang, C. Tu, F. Wu, G. Tong, Y. Su, L. Xu, X. Zhang, S. Xiong, X. Zhu, A mesoporous polydopamine nanoparticle enables highly efficient manganese encapsulation for enhanced MRI-guided photothermal therapy, Nanoscale, 13 (2021) 6439-6446.

[206] J. Lu, L. Cai, Y. Dai, Y. Liu, F. Zuo, C. Ni, M. Shi, J. Li, Polydopamine-Based Nanoparticles for Photothermal Therapy/Chemotherapy and their Synergistic Therapy with Autophagy Inhibitor to Promote Antitumor Treatment, Chem. Rec., 21 (2021) 781-796.

[207] B.F. Grześkowiak, D. Maziukiewicz, A. Kozłowska, A. Kertmen, E. Coy, R. Mrówczyński, Polyamidoamine Dendrimers Decorated Multifunctional Polydopamine Nanoparticles for Targeted Chemo- and Photothermal Therapy of Liver Cancer Model, Int. J. Mol. Sci., 22 (2021) 738.

[208] Q. Lyu, N. Hsueh, C.L.L. Chai, The Chemistry of Bioinspired Catechol(amine)-Based Coatings, ACS Biomater. Sci. Eng., 5 (2019) 2708-2724.

[209] Y. Wang, Y. Xiong, J. Qu, J. Qu, S. Li, Selective sensing of hydroquinone and catechol based on multiwalled carbon nanotubes/polydopamine/gold nanoparticles composites, Sens. Actuators, B, 223 (2016) 501-508.

[210] N.N. Mahmoud, H. Aqabani, S. Hikmat, R. Abu-Dahab, Colloidal Stability and Cytotoxicity of Polydopamine-Conjugated Gold Nanorods against Prostate Cancer Cell Lines, Molecules, 26 (2021) 1299.

[211] R. Yegappan, V. Selvaprithiviraj, A. Mohandas, R. Jayakumar, Nano polydopamine crosslinked thiol-functionalized hyaluronic acid hydrogel for angiogenic drug delivery, Colloids Surf., B, 177 (2019) 41-49.

[212] Y. Li, W. Hong, H. Zhang, T.T. Zhang, Z. Chen, S. Yuan, P. Peng, M. Xiao, L. Xu, Photothermally triggered cytosolic drug delivery of glucose functionalized polydopamine nanoparticles in response to tumor microenvironment for the GLUT1-targeting chemo-phototherapy, J. Controlled Release, 317 (2020) 232-245.

[213] J. Feng, Z. Xu, P. Dong, W. Yu, F. Liu, Q. Jiang, F. Wang, X. Liu, Stimuli-responsive multifunctional metal–organic framework nanoparticles for enhanced chemo-photothermal therapy, J. Mater. Chem. B, 7 (2019) 994-1004.

[214] X.-F. Du, Y. Li, J. Long, W. Zhang, D. Wang, C.-R. Li, M.-X. Zhao, Y. Lai, Fabrication of cisplatin-loaded polydopamine nanoparticles via supramolecular self-assembly for photoacoustic imaging guided chemo-photothermal cancer therapy, Appl. Mater. Today, 23 (2021) 101019.

[215] Y. Li, C. Jiang, D. Zhang, Y. Wang, X. Ren, K. Ai, X. Chen, L. Lu, Targeted polydopamine nanoparticles enable photoacoustic imaging guided chemo-photothermal synergistic therapy of tumor, Acta Biomater., 47 (2017) 124-134.

[216] X. Ma, C. Wang, Z. Dong, C. Hu, L. Feng, Lipid-coated CaCO 3-PDA nanoparticles as a versatile nanocarrier to enable pH-responsive dual modal imaging-guided combination cancer therapy, J. Mater. Chem. B, 10 (2022) 4096-4104.

[217] B. Guo, J. Zhao, C. Wu, Y. Zheng, C. Ye, M. Huang, S. Wang, One-pot synthesis of polypyrrole nanoparticles with tunable photothermal conversion and drug loading capacity, Colloids Surf., B, 177 (2019) 346-355.

[218] V.M. Ovando-Medina, R.D. Peralta, E. Mendizábal, H. Martínez-Gutiérrez, T.E. Lara-Ceniceros, R. Ledezma-Rodríguez, Synthesis of polypyrrole nanoparticles by oil-in-water microemulsion polymerization with narrow size distribution, Colloid Polym. Sci., 289 (2011) 759-765.

[219] J.Y. Hong, H. Yoon, J. Jang, Kinetic study of the formation of polypyrrole nanoparticles in water-soluble polymer/metal cation systems: a light-scattering analysis, Small, 6 (2010) 679-686.

[220] K.-Y. Lu, P.-R. Jheng, L.-S. Lu, L. Rethi, F.-L. Mi, E.-Y. Chuang, Enhanced anticancer effect of ROS-boosted photothermal therapy by using fucoidan-coated polypyrrole nanoparticles, Int. J. Biol. Macromol., 166 (2021) 98-107.

[221] X. Liang, Y. Li, X. Li, L. Jing, Z. Deng, X. Yue, C. Li, Z. Dai, PEGylated polypyrrole nanoparticles conjugating gadolinium chelates for dual-modal MRI/photoacoustic imaging guided photothermal therapy of cancer, Adv. Funct. Mater., 25 (2015) 1451-1462.

[222] T. Burnouf, P.-R. Jheng, Y.-H. Chen, L. Rethi, L. Rethi, L.-S. Lu, Y.-C. Ho, E.-Y. Chuang, Near-infrared-driven photoablation of lung cancer tumors utilizing biomimetic platelet-polyethyleneimine-polypyrrole drug-free nanoparticles, Mater. Des., 215 (2022) 110481.

[223] D. Mantione, I. Del Agua, A. Sanchez-Sanchez, D. Mecerreyes, Poly(3,4-ethylenedioxythiophene) (PEDOT) Derivatives: Innovative Conductive Polymers for Bioelectronics, Polymers, 9 (2017) 354.

[224] N. Paradee, A. Sirivat, Synthesis of poly (3, 4-ethylenedioxythiophene) nanoparticles via chemical oxidation polymerization, Polym. Int., 63 (2014) 106-113.

[225] G.L. Ong, T.S. Ong, S.L. Yap, D.-J. Liaw, T.Y. Tou, S.S. Yap, C.H. Nee, A brief review of nanoparticles-doped PEDOT:PSS nanocomposite for OLED and OPV, Nanotechnol. Rev., 11 (2022) 1870-1889.

[226] H. Gong, Cheng, L., Xiang, J., Xu, H., Feng, L., Shi, X. and Liu, Z., Near-Infrared Absorbing Polymeric Nanoparticles as a Versatile Drug Carrier for Cancer Combination Therapy, Adv. Funct. Mater., 23 (2013) 6059-6067.

[227] L. Cheng, K. Yang, Q. Chen, Z. Liu, Organic Stealth Nanoparticles for Highly Effective in Vivo Near-Infrared Photothermal Therapy of Cancer, ACS Nano, 6 (2012) 5605-5613.

[228] A.H. Odda, T.-Y. Cheang, H.F. Alesary, L. Liu, X. Qian, N. Ullah, G. Wang, Y. Pan, A.-W. Xu, A multifunctional α-Fe2O3@PEDOT core–shell nanoplatform for gene and photothermal combination anticancer therapy, J. Mater. Chem. B, 10 (2022) 1453-1462.

[229] M. Ayad, G. El-Hefnawy, S. Zaghlol, Facile synthesis of polyaniline nanoparticles; its adsorption behavior, Chem. Eng. J., 217 (2013) 460-465.

[230] J.-G. Shin, C.-S. Park, E.Y. Jung, B.J. Shin, H.-S. Tae, Synthesis of a polyaniline nanoparticle using a solution plasma process with an Ar gas bubble channel, Polymers, 11 (2019) 105.

[231] M. Beygisangchin, S. Abdul Rashid, S. Shafie, A.R. Sadrolhosseini, H.N. Lim, Preparations, properties, and applications of polyaniline and polyaniline thin films—A review, Polymers, 13 (2021) 2003.

[232] B.-P. Jiang, L. Zhang, Y. Zhu, X.-C. Shen, S.-C. Ji, X.-Y. Tan, L. Cheng, H. Liang, Water-soluble hyaluronic acid–hybridized polyaniline nanoparticles for effectively targeted photothermal therapy, J. Mater. Chem. B, 3 (2015) 3767-3776.

[233] J. Zhou, Z. Lu, X. Zhu, X. Wang, Y. Liao, Z. Ma, F. Li, NIR photothermal therapy using polyaniline nanoparticles, Biomaterials, 34 (2013) 9584-9592.

[234] C.-W. Ting, Y.-H. Chou, S.-Y. Huang, W.-H. Chiang, Indocyanine green-carrying polymeric nanoparticles with acid-triggered detachable PEG coating and drug release for boosting cancer photothermal therapy, Colloids Surf., B, 208 (2021) 112048.

[235] R. Ma, N. Alifu, Z. Du, S. Chen, Y. Heng, J. Wang, L. Zhu, C. Ma, X. Zhang, Indocyanine green-based theranostic nanoplatform for NIR fluorescence image-guided chemo/photothermal therapy of cervical cancer, Int. J. Nanomed., 16 (2021) 4847.

[236] C. Fleck, H. Bräunlich, Relation between renal and hepatic excretion of drugs: II. Age-dependence of phenol red excretion in comparison with those of p-aminohippurate and indocyanine green, Exp. Pathol., 29 (1986) 235-247.

[237] Y. Liu, S. Chen, J. Sun, S. Zhu, C. Chen, W. Xie, J. Zheng, Y. Zhu, L. Xiao, L. Hao, Folate-targeted and oxygen/indocyanine green-loaded lipid nanoparticles for dual-mode imaging and photo-sonodynamic/photothermal therapy of ovarian cancer in vitro and in vivo, Mol. Pharmaceutics, 16 (2019) 4104-4120.

[238] H.-J. Yoon, H.-S. Lee, J.-Y. Lim, J.-H. Park, Liposomal indocyanine green for enhanced photothermal therapy, ACS Appl. Mater. Interfaces, 9 (2017) 5683-5691.

[239] F. An, Z. Yang, M. Zheng, T. Mei, G. Deng, P. Guo, Y. Li, R. Sheng, Rationally assembled albumin/indocyanine green nanocomplex for enhanced tumor imaging to guide photothermal therapy, J. Nanobiotechnol., 18 (2020) 1-11.

[240] K. Wang, L. Jiang, L. Qiu, Near infrared light triggered ternary synergistic cancer therapy via L-arginine-loaded nanovesicles with modification of PEGylated indocyanine green, Acta Biomater., 140 (2022) 506-517.

[241] C.G. Alves, R. Lima-Sousa, D. de Melo-Diogo, R.O. Louro, I.J. Correia, IR780 based nanomaterials for cancer imaging and photothermal, photodynamic and combinatorial therapies, Int. J. Pharm., 542 (2018) 164-175.

[242] A. Fernandez-Fernandez, R. Manchanda, T. Lei, D.A. Carvajal, Y. Tang, S.Z.R. Kazmi, A.J. McGoron, Comparative study of the optical and heat generation properties of IR820 and indocyanine green, Mol. Imaging, 11 (2012).

[243] K. Huang, M. Gao, L. Fan, Y. Lai, H. Fan, Z. Hua, IR820 covalently linked with self-assembled polypeptide for photothermal therapy applications in cancer, Biomater. Sci., 6 (2018) 2925-2931.

[244] E. Cooper, P.J. Choi, W.A. Denny, J. Jose, M. Dragunow, T.I.-H. Park, The Use of Heptamethine Cyanine Dyes as Drug-Conjugate Systems in the Treatment of Primary and Metastatic Brain Tumors, Front. Oncol, 11 (2021).

[245] P. Li, Y. Liu, W. Liu, G. Li, Q. Tang, Q. Zhang, F. Leng, F. Sheng, C. Hu, W. Lai, Y. Liu, M. Zhou, J. Huang, H. Zhou, R. Zhang, Y. Zhao, IR-783 inhibits breast cancer cell proliferation and migration by inducing mitochondrial fission, Int. J. Oncol., 55 (2019) 415-424.

[246] N. Kaur, Mimansa, A. Aditya, A. Shanavas, Glycol chitosan stabilized bimolecular nanoparticles for chemo photothermal killing of breast cancer cells, Biomed. Eng. Adv., 3 (2022) 100040.

[247] J. Lv, H. Li, M. Yang, X. Li, J. Gao, Z. Yuan, IR783 Encapsulated in TR-Conjugated Liposomes for Enhancing NIR Imaging-Guided Photothermal and Photodynamic Therapy**, ChemistrySelect, 7 (2022) e202202560.

[248] P. Kumar, R. Srivastava, IR 820 stabilized multifunctional polycaprolactone glycol chitosan composite nanoparticles for cancer therapy, RSC Adv., 5 (2015) 56162-56170.

[249] Y. Jiang, C. Huang, Y. Luan, Lactosylated IR820/DOX Co-Assembled Nanodrug for Synergetic Antitumour Therapy, Int. J. Nanomed., 15 (2020) 4431-4440.

[250] D.M. Valcourt, M.N. Dang, E.S. Day, IR820-loaded PLGA nanoparticles for photothermal therapy of triple-negative breast cancer, J. Biomed. Mater. Res., Part A, 107 (2019) 1702-1712.

[251] M. Shi, Y. Liu, J. Huang, Z. Chen, C. Ni, J. Lu, Y. Zhang, Z. Liu, J. Bai, Multifunctional theranostic nanoplatform loaded with autophagy inhibitor for enhanced photothermal cancer therapy under mild near-infrared irradiation, Biomater. Adv., 138 (2022) 212919.

[252] I.L. Lu, T.-I. Liu, H.-C. Lin, S.-H. Chang, C.-L. Lo, W.-H. Chiang, H.-C. Chiu, IR780-loaded zwitterionic polymeric nanoparticles with acidity-induced agglomeration for enhanced tumor retention, Eur. Polym. J., 122 (2020) 109400.

[253] J. Liu, L. Guo, Y. Rao, W. Zheng, D. Gao, J. Zhang, L. Luo, X. Kuang, S. Sukumar, Y. Tu, In situ Injection of pH-and Temperature-Sensitive Nanomaterials Increases Chemo-Photothermal Efficacy by Alleviating the Tumor Immunosuppressive Microenvironment, Int. J. Nanomed., 17 (2022) 2661.

[254] X. Yang, H. Li, C. Qian, Y. Guo, C. Li, F. Gao, Y. Yang, K. Wang, D. Oupicky, M. Sun, Near-infrared light-activated IR780-loaded liposomes for anti-tumor angiogenesis and Photothermal therapy, Nanomed.: Nanotechnol. Biol. Med., 14 (2018) 2283-2294.

[255] M.G.C. Machado, M.A. de Oliveira, E.G. Lanna, R.P. Siqueira, G. Pound-Lana, R.T. Branquinho, V.C.F. Mosqueira, Photodynamic therapy with the dual-mode association of IR780 to PEG-PLA nanocapsules and the effects on human breast cancer cells, Biomed. Pharmacother., 145 (2022) 112464.

[256] T. Zhang, B. Wu, O.U. Akakuru, C. Yao, S. Sun, L. Chen, W. Ren, A. Wu, P. Huang, Hsp90 inhibitor-loaded IR780 micelles for mitochondria-targeted mild-temperature photothermal therapy in xenograft models of human breast cancer, Cancer Lett., 500 (2021) 41-50.

[257] S.-Y. Lin, R.-Y. Huang, W.-C. Liao, C.-C. Chuang, C.-W. Chang, Multifunctional PEGylated albumin/IR780/iron oxide nanocomplexes for cancer photothermal therapy and MR Imaging, Nanotheranostics, 2 (2018) 106-116.

[258] G. Zhu, K. Wang, H. Qin, X. Zhao, W. Chen, L. Xu, W. Cao, H. Guo, Internal cross-linked polymeric nanoparticles with dual sensitivity for combination therapy of muscle-invasive bladder cancer, J. Nanobiotechnol., 18 (2020) 1-13.

[259] J. Song, N. Zhang, L. Zhang, H. Yi, Y. Liu, Y. Li, X. Li, M. Wu, L. Hao, Z. Yang, IR780-loaded folate-targeted nanoparticles for near-infrared fluorescence image-guided surgery and photothermal therapy in ovarian cancer, Int. J. Nanomed., 14 (2019) 2757.

[260] M. Potara, T. Nagy-Simon, M. Focsan, E. Licarete, O. Soritau, A. Vulpoi, S. Astilean, Folate-targeted Pluronic-chitosan nanocapsules loaded with IR780 for near-infrared fluorescence imaging and photothermal-photodynamic therapy of ovarian cancer, Colloids Surf., B, 203 (2021) 111755.

[261] Y.-J. Lu, A.T. S., C.-C. Chuang, J.-P. Chen, Liposomal IR-780 as a Highly Stable Nanotheranostic Agent for Improved Photothermal/Photodynamic Therapy of Brain Tumors by Convection-Enhanced Delivery, Cancers, 13 (2021) 3690.

Chapter 3: IR780 loaded sulfobetaine methacrylate-functionalized albumin nanoparticles aimed for enhanced breast cancer phototherapy

Research Work 1

This chapter is based on the publication: IR780 loaded sulfobetaine methacrylate-functionalized albumin nanoparticles aimed for enhanced breast cancer phototherapy International Journal of Pharmaceutics, 2020, 582: 119346

3.1. Abstract

New insights about nanomaterials' biodistribution revealed their ability to achieve tumor accumulation by taking advantage from the dynamic vents occurring in tumor's vasculature. This paradigm-shift emphasizes the importance of extending nanomaterials' blood circulation time to enhance their tumor uptake. The classic strategy to improve nanomaterials' stability during circulation relies on their functionalization with poly(ethylene glycol) (PEG). However, recent reports have been showing that PEGylated nanomaterials can suffer from the accelerated blood clearance phenomenon, emphasizing the importance of developing novel coatings for functionalizing the nanomaterials. To address this limitation, the modification of natural carriers' surface to enhance their stability appears to be a promising strategy. Herein, sulfobetaine methacrylate (SBMA)-functionalized bovine serum albumin (BSA) was synthesized for the first time to investigate the capacity of this modification to improve the resulting nanoparticles' physicochemical properties, colloidal stability, and *in vitro* performance. This novel polymer was then employed in the formulation of nanoparticles loaded with IR780 for application in breast cancer phototherapy (IR/SBMA-BSA NPs). When compared to their non-functionalized equivalents, the IR/SBMA-BSA NPs presented a neutral surface charge and a higher stability in biologically relevant media. Due to these features, the IR/SBMA-BSA NPs could achieve a 1.9-fold greater uptake by breast cancer cells than IR/BSA NPs. Furthermore, the IR/SBMA-BSA NPs were cytocompatible towards normal cells and reduced breast cancer cells' viability up to 42 %. The phototherapy mediated by IR/SBMA-BSA NPs could further decrease cancer cells' viability to about 12 %. Overall, the IR/SBMA-BSA NPs have enhanced features that propel their application in breast cancer phototherapy.

Keywords: Albumin nanoparticles, Breast cancer, IR780, Photothermal therapy, Polymer functionalization, Zwitterionic coatings

3.2. Introduction

Phototherapies mediated by nanomaterials have been revealing promising results for cancer therapy [1]. This novel therapeutic modality takes advantage from the ability of nanomaterials to passively accumulate at the tumor site [2]. Subsequently, this zone is exposed to NIR (750-1000 nm) light, and the tumor homed nanomaterials absorb it, generating a temperature increase (PTT) and/or reactive oxygen species (ROS; PDT) [3]. Considering that the NIR radiation has minimal/insignificant interactions with the biological components (*e.g*. water, melanin, collagen), the phototherapies mediated by NIR responsive nanomaterials can potentially perform a spatio-temporal controlled therapy with minimal side effects [1].

Despite nanomaterials' potential for cancer treatment, a recent exhaustive literature analysis has disclosed that less than 1 % of the nanoparticles' injected dose reaches the tumor [4]. Such reality may be explained by the fact that nanomaterials' size has been highly considered as a key parameter mediating nanomedicines' tumor uptake. In fact, nanomaterials can accumulate in the tumor zone by extravasating through the leaky tumor vasculature, which has fenestrae with variable sizes (200 - 1200 nm) [1, 5]. However, new insights into nanomaterials' biodistribution revealed that they can also benefit from the dynamic vents (also termed as eruptions) occurring on the tumor vasculature to accomplish tumor accumulation [6]. Based on this new mechanism, researchers have been modulating nanomaterials' surface properties to increase their blood circulation, leading to an improved tumor uptake [6].

The functionalization of nanomaterials' surface with PEG is the classic strategy employed to improve their blood circulation time [7, 8]. In fact, PEGylated nanomaterials exhibiting a long blood circulation can achieve a high tumor uptake [9, 10]. However, several studies have demonstrated that systemically administered PEGylated nanomaterials can induce immunogenic reactions [11, 12]. In brief, at the time of the first intravenous administration of PEG-nanoparticles, anti-PEG antibodies are formed. These anti-PEG antibodies will then mediate the rapid clearance of the PEG-nanoparticles in subsequent administrations, rendering them ineffective since these will not reach the target site [11, 12]. This behavior is known as the accelerated blood clearance (ABC) phenomenon. The magnitude of the ABC phenomenon depends on multiple factors related to the nanomaterials' intrinsic properties (*e.g.,* type of nanomaterial, PEG density, PEG molecular weight) and to their administration protocol (*e.g.,* administration schedule, dose, route) [11-15]. Nevertheless, these findings should still motivate the development of other nanomaterials' functionalization strategies.

To surpass this bottleneck, the use of natural structures, with long blood circulation times, to formulate nanomaterials is an attractive approach. Albumin-based carriers meet this criterion and are also highly biocompatible and easy to prepare [16]. For instance, the coating of porous silicon nanoparticles with albumin increased their blood circulation half-life from about 29 min to 4.4 h [17]. Nevertheless, PEG coated nanomaterials can still display greater blood circulation times ($t_{1/2} \approx 22$ - 34 h) [18, 19]. In this way, the modification of albumin-based carriers' surface to display an improved stability could possibly potentiate their blood circulation time and hence their tumor uptake [20, 21].

In this work, sulfobetaine methacrylate (SBMA)-modified BSA was synthesized for the first time to investigate the capacity of this modification to improve the resulting nanoparticles' physicochemical properties, colloidal stability, and *in vitro* performance. This novel polymer was then employed in the formulation of nanoparticles loaded with IR780 for application in breast cancer phototherapy. SBMA was grafted into albumin since it can reduce protein adsorption [22-24], and thus may possibly enhance nanomaterials' stability during circulation. For instance, Men *et al.* verified that poly(SBMA)-based nanogels can achieve a longer blood circulation half-life than their PEGylated equivalents, leading to an up to 4.65-fold higher tumor uptake (10.7 % *vs.* 2.3 % ID g^{-1} of tumor) [25]. Furthermore, nanomaterials with SBMA brushes are not reported to suffer from the ABC phenomenon [25]. As importantly, the direct conjugation of SBMA into albumin is a simpler process when compared to the polymerization of SBMA on nanomaterials' surface [26, 27]. Then, SBMA-*g*-BSA nanoparticles incorporating a NIR responsive small molecule with photothermal and photodynamic capabilities (IR780) were prepared (IR/SBMA-BSA NPs) using the nanoprecipitation method [3, 28]. The results obtained revealed that IR/SBMA-BSA NPs present a suitable size distribution for application in cancer therapy with an average size of 96.1 ± 8.1 nm and a spherical morphology. When compared to the non-functionalized BSA nanoparticles loaded with IR780 (IR/BSA NPs), the IR/SBMA-BSA NPs presented a neutral surface charge and an increased stability in biologically relevant media. Due to these features, the IR/SBMA-BSA NPs could display a 1.9-fold greater uptake by MCF-7 cells than IR/BSA NPs. The photothermal capacity of IR/SBMA-BSA NPs was also investigated, being verified that the nanostructures generate a temperature increase upon interaction with NIR light. In the cell culture studies, the IR/SBMA-BSA NPs were cytocompatible towards normal cell lines. However, these induced a dose- and time-dependent cytotoxic effect on breast cancer cells. IR/SBMA-BSA NPs therapeutic capacity was further increased when the cells were exposed to NIR radiation.

3.3. Materials and Methods

3.3.1. Materials

IR780 iodide, resazurin, DL-Dithiothreitol (DTT), Dulbecco's Modified Eagle's Medium F12 (DMEM-F12), [2-(methacryloyloxy)ethyl]dimethyl-(3-sulfopropyl)ammonium hydroxide (SBMA), and trypsin were acquired from Sigma-Aldrich (Sintra, Portugal). BSA was obtained from Amresco (Pennsylvania, EUA). Acetone, Triton X-100, and Methanol were bought from Fisher Scientific (Oeiras, Portugal). Michigan Cancer Foundation-7 (MCF-7) cell line was acquired from ATCC (Middlesex, UK) and Normal Human Dermal Fibroblast (NHDF) from Promocell (Heidelberg, Germany). Cell culture plates and T-flasks were purchased from Thermo Fisher Scientific (Porto, Portugal). Fetal Bovine Serum (FBS) was obtained from Biochrom AG (Berlin, Germany). Water used in all experiments was double deionized (0.22 μm filtered, 18.2 M Ω cm).

3.3.2. Methods

3.3.2.1. SBMA-*g*-BSA synthesis and characterization

The synthesis of SBMA-*g*-BSA was performed through a Michael addition by adapting the protocol previously described by Venault and coworkers [29]. In brief, BSA (250 mg) and SBMA (194 mg) were dissolved in water (a molar excess of SBMA to the primary amine and thiol groups of BSA was used). Afterwards, the pH of the solution was adjusted to 12 using NaOH (1 M) and the solution was left to stir at 37 °C for 24 h. Then, this solution was dialyzed (14 kDa molecular weight cut-off) against water for 2 days and the recovered solution was freeze-dried (ScanVac CoolSafe, LaboGene ApS, Lynge, Denmark), yielding SBMA-*g*-BSA. The successful synthesis of SBMA-*g*-BSA was confirmed by Fourier transform infrared spectroscopy (FTIR) using a Nicolet iS10 spectrometer (Thermo Scientific Inc., MA, USA) and by Proton nuclear magnetic resonance (^{1}H NMR) using a Brüker Avance III 400 MHz spectrometer (Brüker Scientific Inc., NY, USA). For the ^{1}H NMR experiments, SBMA, BSA, and SBMA-*g*-BSA were analyzed at 298 K in 9:1 (v/v) H_2O/D_2O. MNova software (Mestrelab Research, SL, Santiago de Compostela, Spain) was used to process and analyze the acquired spectra.

3.3.2.2. Formulation of IR/SBMA-BSA NPs

IR780 loaded SBMA-*g*-BSA nanoparticles (IR/SBMA-BSA NPs) were formulated using the nanoprecipitation technique [30]. Initially, SBMA-*g*-BSA (5 mg) and DTT (386 μg) were added to 5 mL of PBS and then were left to react for 20 min under stirring.

Afterwards, IR780 (250 μg) in acetone (1 mL) was added dropwise to the polymer-DTT solution during 20 min at room temperature. Then, this solution was recovered and dialyzed (14 KDa molecular weight cut-off) against water for 90 min, yielding IR/SBMA-BSA NPs. As a control, IR780 loaded BSA nanoparticles (IR/BSA NPs) were also prepared using the above described method but using BSA instead of SBMA-*g*-BSA.

3.3.2.3. Physicochemical characterization of IR/SBMA-BSA NPs

The size distribution of the produced NPs was determined by Dynamic Light Scattering (DLS) using a ZetaSizer NanoZS (Malvern Instruments Ltd., Worcestershire, UK) at 25 °C. Furthermore, the variation of nanoparticles' size overtime when dispersed in PBS (pH 7.4; 10 mM of Na_2HPO_4) and cell culture medium (DMEM-F12 supplemented with 0, 10, and 20 % (v/v) of FBS) was also analyzed. The zeta potential of the nanoformulations in water, PBS (pH 7.4) at 5 and 10 mM (of Na_2HPO_4) and DMEM-F12 medium with 0, 10, and 20 % (v/v) of FBS was also determined using the ZetaSizer. To evaluate the morphology of the nanoparticles, these were stained with phosphotungstic acid (2 % (w/v)) before being analyzed in a Hitachi-HT7700 Transmission Electron Microscope (TEM, Hitachi Ltd., Tokyo, Japan), operated at an accelerating voltage of 100 kV. Samples' UV-Vis-NIR absorption spectrum was acquired by using an Evolution 201 spectrophotometer (Thermo Scientific Inc.). For this purpose, IR/SBMA-BSA NPs dispersed in water, PBS (pH 7.4; 10 mM of Na_2HPO_4), and cell culture medium with 10 % of FBS were analyzed. The encapsulation efficiency (EE) of IR780 in the IR/SBMA-BSA NPs was determined by analyzing the samples' absorbance at 780 nm in a water:methanol (1:1 (v/v)) solution, using a method previously reported by Alves *et al.* [30]. The photothermal capacity of IR/SBMA-BSA NPs was determined by exposing the nanomaterials to NIR radiation (808 nm, 1.7 W cm^{-2}) and recording the temperature variations using a thermocouple thermometer [31].

3.3.2.4. Cytocompatibility of IR/SBMA-BSA NPs

IR/SBMA-BSA NPs cytocompatibility towards MCF-7 cells and NHDF was assessed using the resazurin method as previously described by Lima-Sousa *et al.* [32]. To perform these assays, cells were cultured in DMEM-F12 medium supplemented with 10 % (v/v) of FBS and 1 % (v/v) of streptomycin/gentamycin in a humified incubator (37 °C; 5 % of CO_2). To evaluate IR/SBMA-BSA NPs cytocompatibility, MCF-7 cells and NHDF were cultured in 96-well plates at a density of 1×10^4 cells per well. After 24 h, cells were incubated with medium containing different concentrations of

IR/SBMA-BSA NPs (0.5 - 5 μg mL^{-1} of IR780 equivalents) during 24 and 48 h. Afterwards, cells were incubated with fresh medium containing 10 % (v/v) of resazurin during 4 h in the dark (37 °C, 5% CO_2). Finally, the fluorescence of resorufin was quantified to assess cells' viability by using excitation and emission wavelengths of 560 and 590 nm, respectively, using a Spectramax Gemini EM spectrofluorometer (Molecular Devices LLC, California, USA). Non treated cells were used as the negative control (K-) while cells treated with ethanol 70 % were used as the positive control (K+).

3.3.2.5. Uptake of IR/SBMA-BSA NPs by MCF-7 cells

The uptake of IR/SBMA-BSA NPs by MCF-7 cells was determined as previously described by Reis *et al.* [33]. In brief, MCF-7 cells (1×10^4 cells/well) were seeded in 96-well plates, and after 24 h, cells were incubated with fresh medium (DMEM-F12 supplemented with 0, 10, or 20 % (v/v) of FBS) containing IR/SBMA-BSA NPs or IR/BSA NPs at a concentration of 1 μg mL^{-1} (of IR780 equivalents) during 4 h. Then, cells were washed with ice-cold Krebs Ringer Buffer in order to remove the non-internalized nanoparticles. Subsequently, cells were incubated with a lysis solution (1 % (v/v) of Triton X-100 in Krebs Buffer) under orbital stirring for 30 min. Finally, the IR780 fluorescence in the cell lysate was quantified in a spectrofluorometer using excitation and emission wavelengths of 780 and 800 nm, respectively. The control was performed with cells only incubated with Krebs Buffer.

3.3.2.6. Phototherapeutic effect mediated by IR780/SBMA-BSA NPs

The phototherapeutic effect mediated by IR/SBMA-BSA NPs was determined as described by Lima-Sousa *et al.* [32]. In brief, MCF-7 cells were seeded in 96-well plates at a density of 1×10^4 cells per well. After 24 h, the medium was replaced by fresh medium containing different concentrations of IR/SBMA-BSA NPs (1, 2, and 5 μg mL^{-1} of IR780 equivalents). After 4 h, the cells were irradiated with NIR light (808 nm, 1.7 W cm^{-2}) for 5 min. After 24 h of incubation, the medium was replaced by fresh medium containing resazurin (10 % (v/v)) and the cells' viability was determined as described above.

3.3.2.7. Statistical analysis

The statistical analysis of two groups was performed using the unpaired *t-student* test. Multiple groups comparison was performed by one-way analysis of variance (ANOVA) with the Student-Newman-Keuls test. A p-value <0.05 was considered statistically

significant. All data are represented as the mean ± standard deviation (S.D.). Data analysis was performed in GraphPad Prism v6.0 (Trial version, GraphPad Software, CA, USA).

3.4. Results and Discussion

3.4.1. Synthesis and characterization of SBMA-*g*-BSA

The synthesis of SBMA-*g*-BSA was performed by a simple method (**Figure 3.1**A). The FTIR spectrum of SBMA showed its S=O stretch (at 1036 and 1235 cm^{-1}) and C=O stretch (at 1715 cm^{-1}) characteristic peaks (Figure 3.1B). In turn, the FTIR spectrum of BSA displayed several peaks belonging to O-H, C-H and C=O vibrations (Figure 3.1B). In the FTIR spectrum of SBMA-*g*-BSA, the characteristic peaks of the BSA functional groups are present as well as the S=O stretch peaks of SBMA (Figure 3.1B and C). Furthermore, the ^{1}H NMR spectrum of SBMA displays a peak at δ ≈ 3.22 ppm corresponding to the -N(C$\mathbf{H_3}$)$_2$- methyl protons - Figure 3.1D. Furthermore, peaks at δ ≈ 3.58 ppm and δ ≈ 2.98 ppm belonging to the -C$\mathbf{H_2}$N(CH$_3$)$_2$- and -C$\mathbf{H_2}$SO$_3$ methylene protons are also present [34]. In turn, the ^{1}H NMR spectrum of SBMA-*g*-BSA presents the characteristic methyl and methylene protons of SBMA (δ ≈ 3.22; 3.58 and 2.98 ppm; Figure 3.1F) as well as those belonging to BSA (Figure 3.1E) [35]. Considering that non-grafted SBMA is removed through dialysis, these results confirm the successful synthesis of SBMA-*g*-BSA.

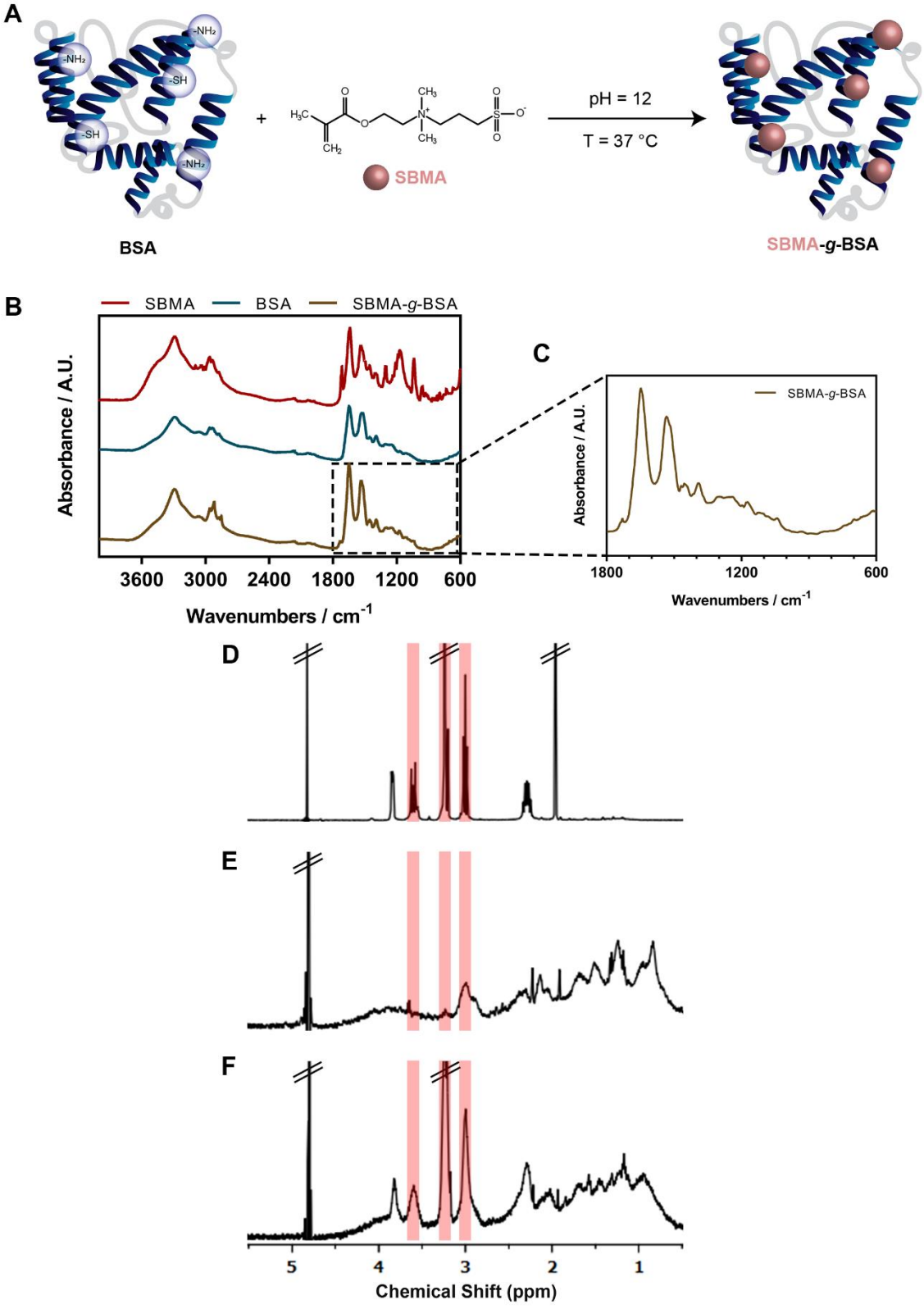

Figure 3.1. Synthesis and characterization of SBMA-*g*-BSA. Schematic representation of the polymer synthesis (A). FTIR spectra of SBMA, BSA, and SBMA-*g*-BSA (B). FTIR spectrum of SBMA-*g*-BSA in the 1800-600 cm^{-1} wavenumber range (C). ^{1}H NMR spectra of SBMA (D), BSA (E) and SBMA-*g*-BSA (F).

3.4.2. Formulation and characterization of IR/SBMA-BSA and IR/BSA NPs

In order to improve the natural carrier properties of BSA, this protein was modified with SBMA yielding SBMA-*g*-BSA (section 3.4.1.). Then, a simple nanoprecipitation method was used to produce IR780 loaded SBMA-*g*-BSA nanoparticles (IR/SBMA-BSA NPs) due to its simplicity and reproducibility (**Figure 3.2**A) [36]. The DLS analysis revealed that IR/SBMA-BSA NPs have an average size of 96.1 ± 8.1 nm and a low PDI of 0.181 (Figure 3.2B; n = 3, batch triplicates).

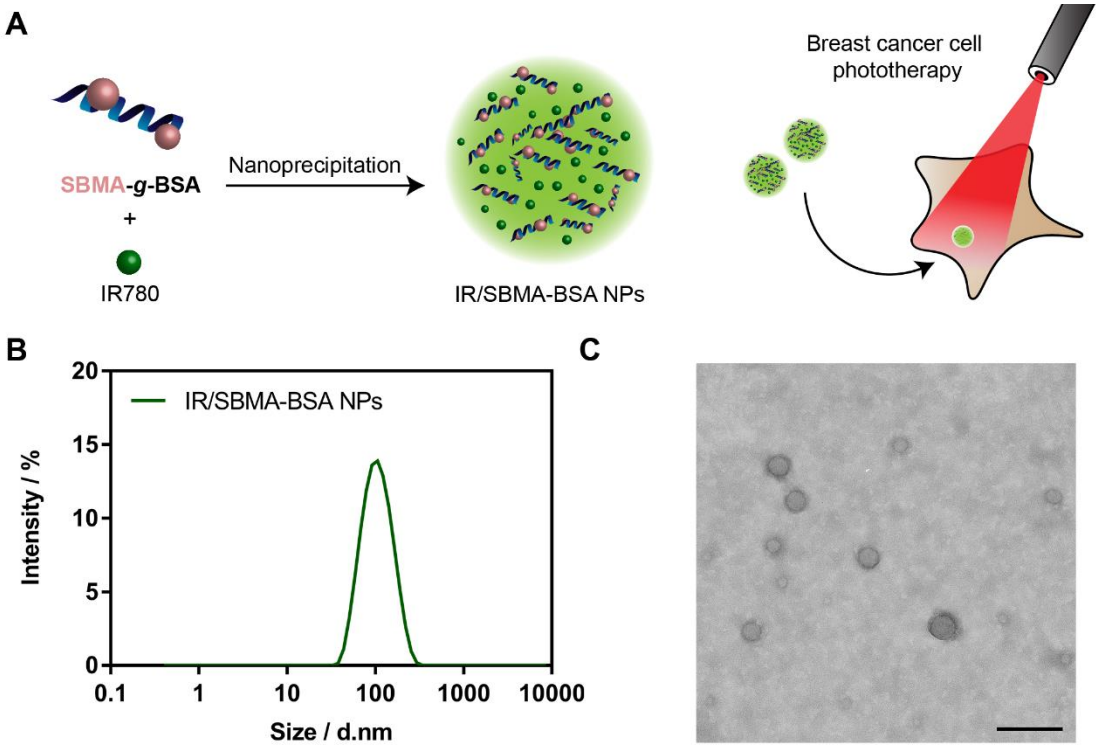

Figure 3.2. Formulation and characterization of IR/SBMA-BSA NPs. Schematic representation of the nanoparticles' formulation and phototherapeutic application (A). DLS size distribution (B) and TEM analysis (C) of IR/SBMA-BSA NPs. Scale bar corresponds to 200 nm.

As control, IR780 loaded BSA nanoparticles (IR/BSA NPs) were also prepared, displaying a similar size to that of IR/SBMA-BSA NPs (**Figure 3.3**A). Such indicates that the SBMA modification does not compromise the nanoparticle-forming capacity of BSA. Furthermore, the size of IR/SBMA-BSA NPs is also in agreement with that previously reported for other BSA-based nanoparticles [37, 38] and it is within the range

considered to be optimal for tumor accumulation [1]. TEM analysis (Figure 3.2C) revealed that IR/SBMA-BSA NPs display a spherical shape, a feature that was also observed in other IR780 loaded nanostructures prepared by the nanoprecipitation method [30, 36, 39]. As importantly, spherical shaped nanomedicines have been associated to an increased uptake by cancer cells [40, 41].

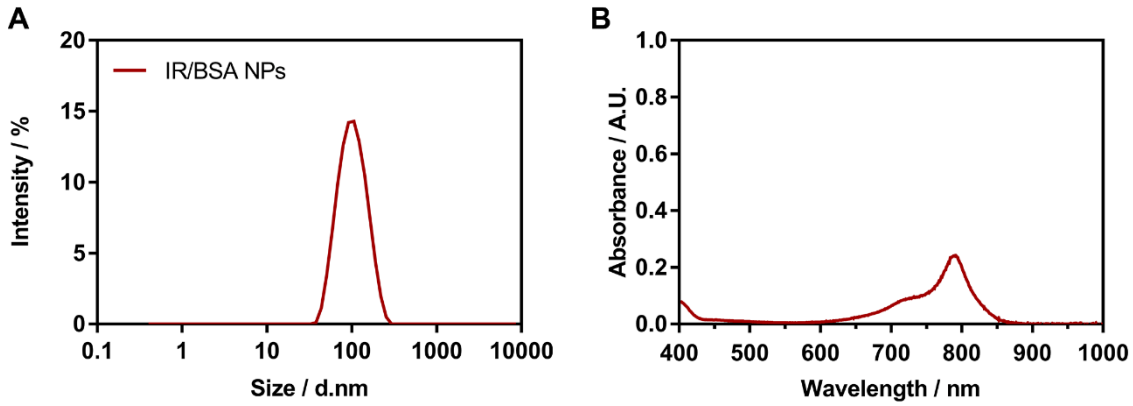

Figure 3.3. Characterization of IR/BSA NPs. DLS size distribution of IR/BSA NPs (A). UV-Vis-NIR spectrum of IR/BSA NPs (at 2.5 μg mL^{-1} of IR780 equivalents) (B).

The zeta potential of IR/SBMA-BSA NPs was determined to be -9.6 ± 0.3 mV, while that of IR/BSA NPs was -12.3 ± 0.4 mV (in PBS 10 mM pH 7.4; n = 3, batch triplicates) – **Table 1**. The solutions' ionic strength can also influence nanoparticles' zeta potential [42]. In this way, the zeta potential of IR/SBMA-BSA NPs and IR/BSA NPs in different media was also determined (Table 1).

Table 1 - Zeta potential of IR/SBMA-BSA NPs and IR/BSA NPs in different media.

Solvent	IR/SBMA-BSA NPs zeta potential (mV)	IR/BSA NPs zeta potential (mV)
Water	-18.83 ± 0.61	-24.75 ± 0.49
PBS 5 mM* (pH 7.4)	-11.30 ± 0.57	-13.87 ± 0.86
PBS 10 mM* (pH 7.4)	-9.60 ± 0.47	-12.33 ± 1.22
Culture medium with 0 % of FBS	-9.78 ± 0.73	-12.23 ± 1.29
Culture medium with 10 % of FBS	-9.04 ± 0.94	-11.73 ± 0.99
Culture medium with 20 % of FBS	-6.34 ± 0.33	-10.17 ± 1.88

*concentration of Na_2HPO_4

As expected, in biologically relevant media, the IR/SBMA-BSA NPs presented a more neutral surface charge when compared to those displayed by IR/BSA NPs (Table 1). The difference in the surface charge of IR/SBMA-BSA NPs can be justified by the SBMA grafting into BSA since SBMA coatings are neutrally charged [29, 43]. As importantly, the zeta potentials of IR/SBMA-BSA NPs are within the so-called neutral charge range (-10 to +10 mV), which has been described as optimal in the literature [1].

IR/SBMA-BSA NPs had an IR780 encapsulation efficiency of 50.7 ± 3.3 %. The encapsulation of IR780 in other polymer-based nanoparticles and micelles also yielded similar results [30, 44]. Moreover, the loading of IR780 into the IR/SBMA-BSA NPs enhanced the water solubility of this NIR dye by 63-fold (from 0.4 to 25.35 $\mu g\ mL^{-1}$) [44]. In this way, the loading of IR780 into the IR/SBMA-BSA NPs addresses the low water solubility of IR780, which is a major drawback of this NIR dye.

Lastly, the stability of the IR/SBMA-BSA NPs overtime in PBS (10 mM pH 7.4; **Figure 3.4**A) and cell culture medium (DMEM-F12 supplemented with 0, 10 or 20 % (v/v) of FBS) was assessed (Figure 3.4B to D). Overall, IR/SBMA-BSA NPs maintained their size distribution overtime when incubated in all the solutions while the size of IR/BSA NPs could suffer stark variations. The size of IR/BSA NPs augmented by 14 % when these were dispersed in PBS (Figure 3.4A). On the other hand, when IR/BSA NPs were dispersed in cell culture medium without FBS, their size remained unaffected (Figure 3.4B). However, IR/BSA NPs dispersed in culture medium with 10 or 20 % of FBS suffered an increase in their size by up to 4-fold (Figure 3.4C and D). Such behavior indicates that IR/BSA NPs may have a weaker stability and that interact with the proteins present in the culture medium. In fact, SBMA coatings can reduce protein adsorption, leading to an improvement in nanomaterials' stability during blood circulation [25, 45]. In this way, the grafting of SBMA into BSA enabled the assembly of IR/SBMA-BSA NPs that display an improved stability.

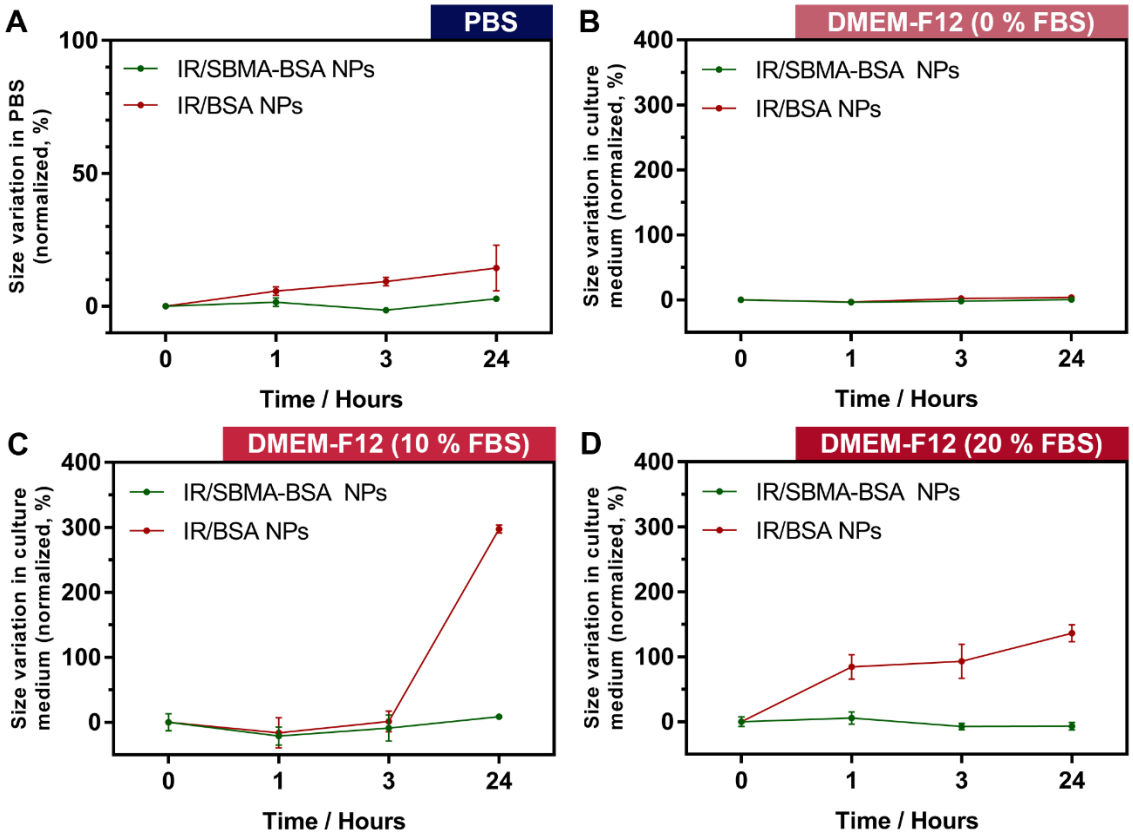

Figure 3.4. Stability of IR/SBMA-BSA and IR/BSA NPs in different media. Size variation of IR/SBMA-BSA and IR/BSA NPs when dispersed in PBS (pH 7.4) at 10 mM (of Na_2HPO_4) (A), in DMEM-F12 medium with 0 % (B), 10 % (C), and 20 % (D) of FBS (v/v). The values of each group were normalized using the respective initial size (t = 0 h). Each bar represents mean ± S.D. (n = 3).

3.4.3. NIR absorption and phototherapeutic capacity of IR/SBMA-BSA NPs

The ability of IR/SBMA-BSA NPs to interact with NIR light was then assessed by evaluating their NIR absorption (**Figure 3.5**A). As expected, free IR780 (dissolved in methanol) presented an absorption peak at 780 nm. The IR/SBMA-BSA NPs had their maximum NIR absorption at 792 nm (Figure 3.5A). This red-shift in IR780 absorption, when encapsulated in SBMA-BSA NPs, occurs due to the hydrophobic interactions established between the NIR dye and the aromatic moieties of the nanocarriers or due to alterations in solvents polarity [36]. Due to this red shift, the IR/SBMA-BSA NPs absorbance at 808 nm is 1.04 times higher than that of free IR780 (at the same concentration of IR780 equivalents). This is of extreme importance since 808 nm laser light is generally used in cancer phototherapy [46-48]. As expected, the UV-Vis-NIR spectrum of IR/BSA NPs was similar to that of IR/SBMA-BSA NPs (Figure 3.3B),

indicating that the SBMA-functionalization does not compromise the ability of these formulations to interact with NIR light.

Furthermore, the IR/SBMA-BSA NPs retained their NIR absorption overtime, even when dispersed in PBS (Figure 3.5B) or in DMEM-F12 supplement with 10 % of FBS (Figure 3.5C). Considering that free IR780 in aqueous solutions loses its optical properties overtime [49], the loading of IR780 into IR/SBMA-BSA NPs can enhance its optical stability.

To confirm their photothermal capacity, IR/SBMA-BSA NPs were irradiated with 808 nm laser light (808 nm, 1.7 W cm^{-2}) and the temperature variations were recorded (Figure 3.5D). Overall, IR/SBMA-BSA NPs produced a concentration- and time-dependent temperature increase when exposed to NIR light. At the maximum concentration tested (20 μg mL^{-1} of IR780 equivalents), the IR/SBMA-BSA NPs induced a temperature increase of about 13 °C after 2 min of irradiation, decreasing slightly afterwards. This phenomenon is attributed to the photodegradation of IR780, which has been extensively reported elsewhere [49, 50]. Still, the temperature variation achieved is sufficiently high to damage cancer cells [1, 51]. As importantly, water exposed to NIR light (control) did not suffer a meaningful temperature variation ($\Delta T < 1.8$ °C). Such is in agreement with the low interaction of 808 nm radiation with water and suggests the ability of IR/SBMA-BSA NPs to produce a therapeutic effect with high spatio-temporal resolution.

For instance, Lu *et al.* prepared IR780 loaded PEGylated zwitterionic nanoparticles that could produce a temperature increase of 10.8 °C after 2 min of irradiation (808 nm, 1.0 W cm^{-2}) at an IR780 concentration of 26.7 μg mL^{-1} [39]. Herein, the IR/SBMA-BSA NPs generated a photoinduced heat of 13.2 °C after 2 min of irradiation (808 nm, 1.7 W cm^{-2}) using 20 μg mL^{-1} of IR780. Together, these results suggest that IR/SBMA-BSA NPs are also promising photothermal agents.

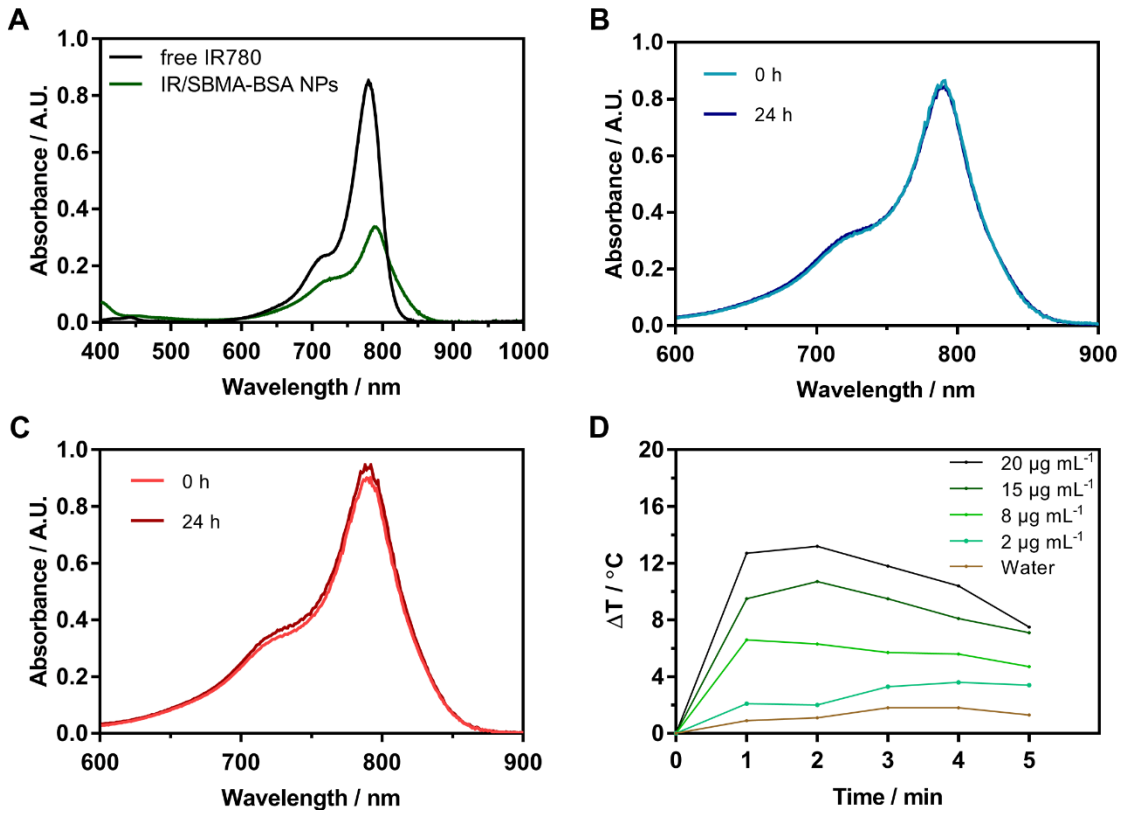

Figure 3.5. Evaluation of the photothermal capacity of IR/SBMA-BSA NPs. UV-Vis-NIR absorption spectra of free IR780 (2.5 µg mL^{-1}; in methanol) and of IR/SBMA-BSA NPs (at 2.5 µg mL^{-1} of IR780 equivalents) (A). UV-Vis-NIR absorption spectra of IR/SBMA-BSA NPs in PBS (B) and in DMEM-F12 medium supplemented with 10 % of FBS (C) after 0 and 24 h of incubation. *In vitro* temperature increase mediated by IR/SBMA-BSA NPs, at different concentrations of IR780 equivalents, upon NIR laser irradiation (808 nm, 1.7 W cm^{-2}) (D).

3.4.4. Cytocompatibility of IR/SBMA-BSA NPs

Before determining the phototherapeutic capacity of IR/SBMA-BSA NPs, their cytocompatibility towards breast cancer (MCF-7) and healthy human (NHDF) cells was assessed (**Figure 3.6**A and B). The IR/SBMA-BSA NPs did not induce cytotoxicity towards NHDF after an incubation period of 24 and 48 h, and up to a concentration of 5 µg mL^{-1} (of IR780 equivalents). In turn, IR/SBMA-BSA NPs produced a dose- and incubation time-dependent cytotoxicity on MCF-7 cells. Such effect may be related to the fact that IR780 predominantly accumulates in the mitochondria of MCF-7 cells and other types of cancer cells when compared to normal cells, thereby inducing a cytotoxic effect [52, 53]. Pais-Silva and Jiang also reported a dose dependent cytotoxicity of IR780 loaded nanostructures towards MCF-7 cells [36, 44].

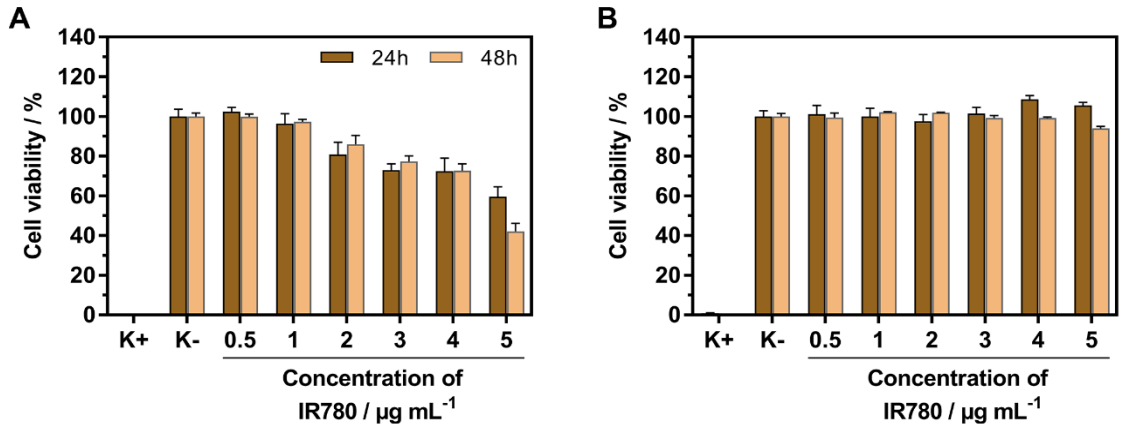

Figure 3.6. Cytocompatibility of IR/SBMA-BSA NPs. Cytocompatibility of IR/SBMA-BSA NPs at different concentrations (of IR780 equivalents) and incubation times (24 and 48 h) towards MCF-7 cells (A) and NHDF (B). K- and K+ were used as negative and positive controls, respectively. Each bar represents the mean ± SD (n = 5).

3.4.5. Uptake of IR/SBMA-BSA NPs by MCF-7 cells and phototherapeutic capacity

Then, the uptake of IR/SBMA-BSA NPs by MCF-7 cells was investigated (**Figure 3.7**A to C) [33, 54]. For this analysis, IR/SBMA-BSA NPs and IR/BSA NPs were incubated using cell culture medium with 0, 10 or 20 % (v/v) of FBS.

When incubated in culture medium without FBS, the IR/SBMA-BSA NPs and IR/BSA NPs presented a similar internalization in MCF-7 cells (Figure 3.7A). In contrast, the uptake studies using culture medium with 10 % of FBS revealed that IR/SBMA-BSA NPs achieve a 1.58 ± 0.32-fold higher internalization in MCF-7 cells when compared to IR/BSA NPs (Figure 3.7B). This differential uptake was even more accentuated when the nanoformulations were incubated using culture medium with 20 % of FBS (Figure 3.7C). In this case, the uptake of IR/SBMA-BSA NPs by cancer cells was 1.89 ± 0.02-fold higher than that of IR/BSA NPs (Figure 3.7C).

In general, neutral- and positively- charged nanomaterials can achieve a higher cellular internalization as a result of interactions with the negatively charged components of cells' membrane [1]. In this way, the improved uptake of IR/SBMA-BSA NPs by MCF-7 cells can be explained by the neutral surface charge of this formulation in the different media (as analyzed in section 3.4.2.). The enhanced colloidal stability of IR/SBMA-BSA NPs can also contribute for their improved uptake (as analyzed in section 3.4.2.). In fact, in culture medium supplemented with FBS, the IR/BSA NPs not only presented a negative

surface charge (Table 1) but also suffered an up to 4-fold increase in their size distribution (Figure 3.4), which may contribute for their lower cellular uptake.

Finally, the phototherapeutic capacity of IR/SBMA-BSA NPs towards MCF-7 cells was investigated. At the concentration of 2 μg mL^{-1} (of IR780 equivalents), the non-irradiated IR/SBMA-BSA NPs could decrease MCF-7 cells' viability to 81 % (Figure 3.7D), while the combined action of IR/SBMA-BSA NPs and NIR light (808 nm, 1.7 W cm^{-2}, 5 min) decreased the cells' viability to 63 %. In contrast, the combination of NIR light and IR/SBMA-BSA NPs, at the concentration of 5 μg mL^{-1}, generated an improved therapeutic effect by further decreasing MCF-7 cells' viability to about 12 %. In these assays, the sole application of the NIR light did not cause cytotoxicity, which is in agreement with the weak interaction of this radiation with biological components [30, 31, 54, 55].

Rajendrakumar *et al.* prepared IR780 loaded poly(12-(methacryloyloxy)dodecyl phosphorylcholine) micelles that, at the concentration of 15 μg mL^{-1} (of IR780 equivalents), could reduce cancer cells' viability to 20 % upon NIR laser irradiation (808 nm, 2.0 W cm^{-2}, 5 min) [56]. In another work, the chemo-phototherapeutic effect mediated by IR780 and DOX loaded hyaluronic acid-based micelles reduced MCF-7 cells' viability to about 20 % (3.5 μg mL^{-1} of IR780; 1.93 μg mL^{-1} of DOX; 808 nm, 1.7 W cm^{-2}, 5 min) [30]. Herein, the phototherapeutic effect (808 nm, 1.7 W cm^{-2}, 5 min) induced by IR/SBMA-BSA NPs decreased MCF-7 cells' viability to 12 % at only 5 μg mL^{-1} (of IR780 equivalents). In this way, IR/SBMA-BSA NPs are promising agents for breast cancer phototherapy.

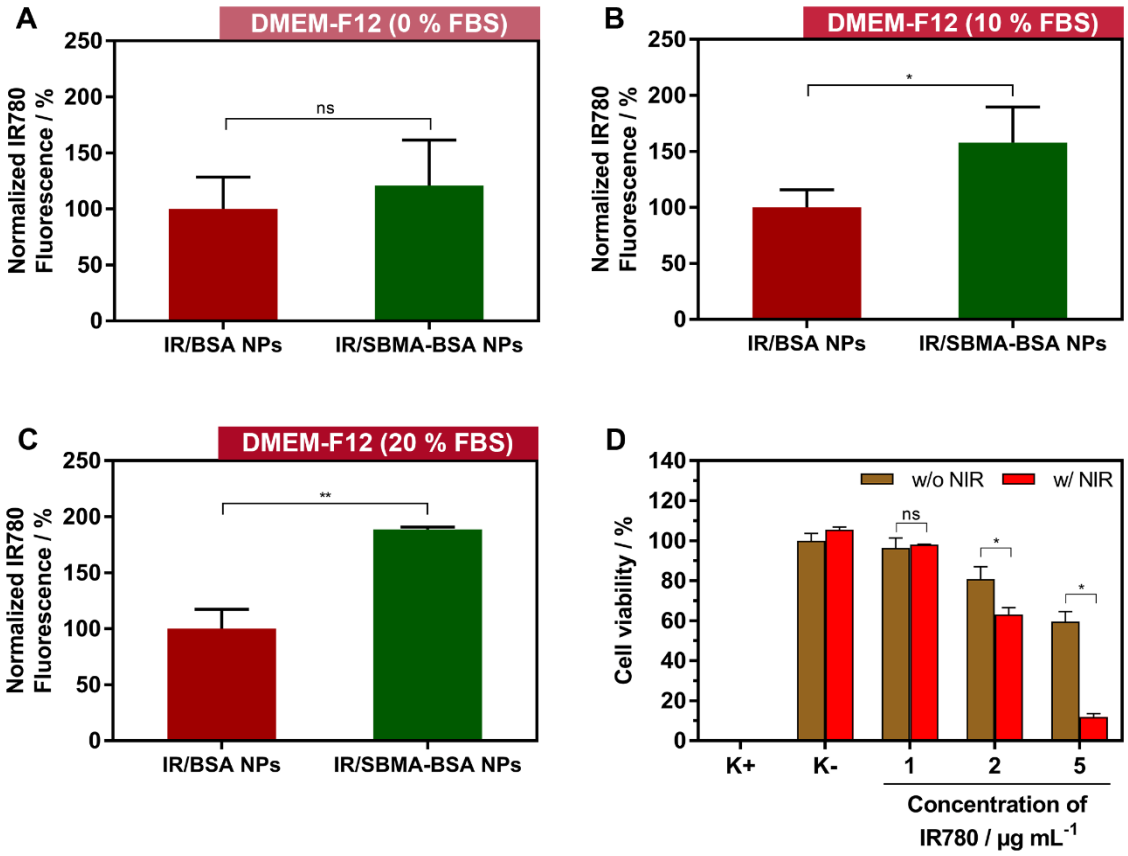

Figure 3.7. *In vitro* biological evaluation of IR/SBMA-BSA NPs. Uptake of IR/SBMA-BSA NPs and IR/BSA NPs by MCF-7 cells when incubated using DMEM-F12 medium with 0 % (A), 10 % (B), and 20 % (C) of FBS (v/v). The fluorescence values were normalized using the fluorescence values obtained for cells incubated with IR/BSA NPs. Evaluation of the therapeutic effect mediated by IR/SBMA-BSA NPs, at different concentrations (of IR780 equivalents), upon NIR laser irradiation (808 nm, 1.7 W cm^{-2}, 5 min) towards MCF-7 cells (D). K- w/o NIR and K+ were used as negative and positive controls, respectively. Each bar represents the mean ± SD (n = 5), $^{*}p < 0.05$.

3.5. Conclusion

In this work, IR780 loaded SBMA functionalized BSA NPs were prepared for the first time for application in breast cancer phototherapy. The IR/SBMA-BSA NPs presented a spherical morphology with a size of 96.1 ± 8.1 nm. When compared to the non-functionalized BSA nanoparticles loaded with IR780 (IR/BSA NPs), the IR/SBMA-BSA NPs presented a neutral surface charge in biologically relevant media, which was attributed to the SBMA-functionalization. The IR/SBMA-BSA NPs also displayed an improved stability when dispersed in PBS and DMEM-F12 supplemented with FBS, while the IR/BSA NPs suffered an up to 4-fold increase in their size. Due to their neutral surface charge and improved colloidal stability, the IR/SBMA-BSA NPs could achieve a 1.9-fold higher uptake by MCF-7 cells when compared to IR/BSA NPs. Furthermore, the IR/SBMA-BSA NPs were cytocompatible towards NHDF, while they

were able to reduce MCF-7 cells' viability up to 42 %, which can be justified by IR780 higher mitochondrial accumulation in cancer cells. The combined action of NIR light and IR/SBMA-BSA NPs could further reduce MCF-7 cells' viability to about 12 %. Overall, the SBMA-functionalized BSA nanoparticles incorporating IR780 have enhanced properties for application in breast cancer phototherapy.

3.6. References

[1] D. de Melo-Diogo, C. Pais-Silva, D.R. Dias, A.F. Moreira, I.J. Correia, Strategies to Improve Cancer Photothermal Therapy Mediated by Nanomaterials, Adv. Healthcare Mater., 6 (2017) 1700073.

[2] E. Blanco, H. Shen, M. Ferrari, Principles of nanoparticle design for overcoming biological barriers to drug delivery, Nat. Biotechnol., 33 (2015) 941-951.

[3] C.G. Alves, R. Lima-Sousa, D. de Melo-Diogo, R.O. Louro, I.J. Correia, IR780 based nanomaterials for cancer imaging and photothermal, photodynamic and combinatorial therapies, Int. J. Pharm. (Amsterdam, Neth.), 542 (2018) 164-175.

[4] S. Wilhelm, A.J. Tavares, Q. Dai, S. Ohta, J. Audet, H.F. Dvorak, W.C.W. Chan, Analysis of nanoparticle delivery to tumours, Nat. Rev. Mater., 1 (2016) 16014.

[5] S.K. Hobbs, W.L. Monsky, F. Yuan, W.G. Roberts, L. Griffith, V.P. Torchilin, R.K. Jain, Regulation of transport pathways in tumor vessels: Role of tumor type and microenvironment, Proc. Natl. Acad. Sci. U. S. A., 95 (1998) 4607-4612.

[6] Y. Matsumoto, J.W. Nichols, K. Toh, T. Nomoto, H. Cabral, Y. Miura, R.J. Christie, N. Yamada, T. Ogura, M.R. Kano, Y. Matsumura, N. Nishiyama, T. Yamasoba, Y.H. Bae, K. Kataoka, Vascular bursts enhance permeability of tumour blood vessels and improve nanoparticle delivery, Nat. Nanotechnol., 11 (2016) 533-538.

[7] H. Otsuka, Y. Nagasaki, K. Kataoka, PEGylated nanoparticles for biological and pharmaceutical applications, Adv. Drug Delivery Rev., 64 (2012) 246-255.

[8] L. Yan, F. Zhao, J. Wang, Y. Zu, Z. Gu, Y. Zhao, A Safe-by-Design Strategy towards Safer Nanomaterials in Nanomedicines, Adv. Mater., 31 (2019) 1805391.

[9] M. Zhou, R. Zhang, M. Huang, W. Lu, S. Song, M.P. Melancon, M. Tian, D. Liang, C. Li, A chelator-free multifunctional [64Cu] CuS nanoparticle platform for simultaneous micro-PET/CT imaging and photothermal ablation therapy, J. Am. Chem. Soc., 132 (2010) 15351-15358.

[10] X. Liu, H. Tao, K. Yang, S. Zhang, S.-T. Lee, Z. Liu, Optimization of surface chemistry on single-walled carbon nanotubes for in vivo photothermal ablation of tumors, Biomaterials, 32 (2011) 144-151.

[11] N. d'Avanzo, C. Celia, A. Barone, L. Di Marzio, H.A. Santos, M. Fresta, Immunogenicity of Polyethylene glycol Based Nanomedicines: Mechanisms, Clinical Implications and Systematic Approach, Advanced Therapeutics, (2019) 1900170.

[12] A.S. Abu Lila, H. Kiwada, T. Ishida, The accelerated blood clearance (ABC) phenomenon: Clinical challenge and approaches to manage, J. Controlled Release, 172 (2013) 38-47.

[13] K. Shiraishi, M. Hamano, H. Ma, K. Kawano, Y. Maitani, T. Aoshi, K.J. Ishii, M. Yokoyama, Hydrophobic blocks of PEG-conjugates play a significant role in the accelerated blood clearance (ABC) phenomenon, J. Controlled Release, 165 (2013) 183-190.

[14] H. Xu, K.Q. Wang, Y.H. Deng, D.W. Chen, Effects of cleavable PEG-cholesterol derivatives on the accelerated blood clearance of PEGylated liposomes, Biomaterials, 31 (2010) 4757-4763.

[15] A.S. Abu Lila, K. Nawata, T. Shimizu, T. Ishida, H. Kiwada, Use of polyglycerol (PG), instead of polyethylene glycol (PEG), prevents induction of the accelerated blood clearance phenomenon against long-circulating liposomes upon repeated administration, Int. J. Pharm. (Amsterdam, Neth.), 456 (2013) 235-242.

[16] F.-F. An, X.-H. Zhang, Strategies for preparing albumin-based nanoparticles for multifunctional bioimaging and drug delivery, Theranostics, 7 (2017) 3667-3689.

[17] B. Xia, W. Zhang, J. Shi, S.-j. Xiao, Engineered stealth porous silicon nanoparticles via surface encapsulation of bovine serum albumin for prolonging blood circulation in vivo, ACS Appl. Mater. Interfaces, 5 (2013) 11718-11724.

[18] G. Prencipe, S.M. Tabakman, K. Welsher, Z. Liu, A.P. Goodwin, L. Zhang, J. Henry, H. Dai, PEG branched polymer for functionalization of nanomaterials with ultralong blood circulation, J. Am. Chem. Soc., 131 (2009) 4783-4787.

[19] Y. Sheng, Y. Yuan, C. Liu, X. Tao, X. Shan, F. Xu, In vitro macrophage uptake and in vivo biodistribution of PLA–PEG nanoparticles loaded with hemoglobin as blood substitutes: effect of PEG content, J. Mater. Sci.: Mater. Med., 20 (2009) 1881-1891.

[20] E. Muro, T. Pons, N. Lequeux, A. Fragola, N. Sanson, Z. Lenkei, B. Dubertret, Small and stable sulfobetaine zwitterionic quantum dots for functional live-cell imaging, J. Am. Chem. Soc., 132 (2010) 4556-4557.

[21] T.G. Shutava, K.S. Livanovich, V.V. Pankov, Synergetic effect of polyethylene glycol-grafted chitosan and bovine serum albumin on colloidal stability of polyelectrolyte nanocapsules, Colloids and Surfaces A: Physicochemical and Engineering Aspects, 539 (2018) 69-79.

[22] Y. Chang, S. Chen, Z. Zhang, S. Jiang, Highly protein-resistant coatings from well-defined diblock copolymers containing sulfobetaines, Langmuir, 22 (2006) 2222-2226.

[23] J. Ladd, Z. Zhang, S. Chen, J.C. Hower, S. Jiang, Zwitterionic polymers exhibiting high resistance to nonspecific protein adsorption from human serum and plasma, Biomacromolecules, 9 (2008) 1357-1361.

[24] S. Peng, B. Ouyang, Y. Men, Y. Du, Y. Cao, R. Xie, Z. Pang, S. Shen, W. Yang, Biodegradable zwitterionic polymer membrane coating endowing nanoparticles with ultra-long circulation and enhanced tumor photothermal therapy, Biomaterials, 231 (2020) 119680.

[25] Y. Men, S. Peng, P. Yang, Q. Jiang, Y. Zhang, B. Shen, P. Dong, Z. Pang, W. Yang, Biodegradable zwitterionic nanogels with long circulation for antitumor drug delivery, ACS Appl. Mater. Interfaces, 10 (2018) 23509-23521.

[26] G.S. Ibrahim, A.M. Isloor, A.M. Asiri, N. Ismail, A.F. Ismail, G.M. Ashraf, Novel, one-step synthesis of zwitterionic polymer nanoparticles via distillation-precipitation polymerization and its application for dye removal membrane, Sci. Rep., 7 (2017) 15889.

[27] S. Lou, X. Zhang, M. Zhang, S. Ji, W. Wang, J. Zhang, C. Li, D. Kong, Preparation of a dual cored hepatoma-specific star glycopolymer nanogel via arm-first ATRP approach, Int. J. Nanomed., 12 (2017) 3653-3664.

[28] M.M. Leitão, D. de Melo-Diogo, C.G. Alves, R. Lima-Sousa, I.J. Correia, Prototypic Heptamethine Cyanine Incorporating Nanomaterials for Cancer Phototheragnostic, Adv. Healthcare Mater., 9 (2020) 1901665.

[29] A. Venault, H.-S. Yang, Y.-C. Chiang, B.-S. Lee, R.-C. Ruaan, Y. Chang, Bacterial resistance control on mineral surfaces of hydroxyapatite and human teeth via surface charge-driven antifouling coatings, ACS Appl. Mater. Interfaces, 6 (2014) 3201-3210.

[30] C.G. Alves, D. de Melo-Diogo, R. Lima-Sousa, E.C. Costa, I.J. Correia, Hyaluronic acid functionalized nanoparticles loaded with IR780 and DOX for cancer chemo-photothermal therapy, Eur. J. Pharm. Biopharm., 137 (2019) 86-94.

[31] D. de Melo-Diogo, C. Pais-Silva, E.C. Costa, R.O. Louro, I.J. Correia, D-α-tocopheryl polyethylene glycol 1000 succinate functionalized nanographene oxide for cancer therapy, Nanomedicine (London, U. K.), 12 (2017) 443-456.

[32] R. Lima-Sousa, D. de Melo-Diogo, C.G. Alves, E.C. Costa, P. Ferreira, R.O. Louro, I.J. Correia, Hyaluronic acid functionalized green reduced graphene oxide for targeted cancer photothermal therapy, Carbohydr. Polym., 200 (2018) 93-99.

[33] C.A. Reis, C.F. Rodrigues, A.F. Moreira, T.A. Jacinto, P. Ferreira, I.J. Correia, Development of gold-core silica shell nanospheres coated with poly-2-ethyl-oxazoline and β-cyclodextrin aimed for cancer therapy, Mater. Sci. Eng. C, 98 (2019) 960-968.

[34] W. Zou, Z. Fan, S. Zhai, S. Wang, B. Xu, Z. Cai, A multifunctional antifog, antifrost, and self-cleaning zwitterionic polymer coating based on poly (SBMA-co-AA), Journal of Coatings Technology and Research, (2020) 1-12.

[35] A. Spence, A.J. Simpson, D.J. Mcnally, B.W. Moran, M.V. McCaul, K. Hart, B. Paull, B.P. Kelleher, The degradation characteristics of microbial biomass in soil, Geochimica et Cosmochimica Acta, 75 (2011) 2571-2581.

[36] C. Pais-Silva, D. de Melo-Diogo, I.J. Correia, IR780-loaded TPGS-TOS micelles for breast cancer photodynamic therapy, Eur. J. Pharm. Biopharm., 113 (2017) 108-117.

[37] B. Kim, C. Lee, E.S. Lee, B.S. Shin, Y.S. Youn, Paclitaxel and curcumin co-bound albumin nanoparticles having antitumor potential to pancreatic cancer, Asian J. Pharm. Sci., 11 (2016) 708-714.

[38] S. Bae, K. Ma, T.H. Kim, E.S. Lee, K.T. Oh, E.-S. Park, K.C. Lee, Y.S. Youn, Doxorubicin-loaded human serum albumin nanoparticles surface-modified with TNF-related apoptosis-inducing ligand and transferrin for targeting multiple tumor types, Biomaterials, 33 (2012) 1536-1546.

[39] I.-L. Lu, T.-I. Liu, H.-C. Lin, S.-H. Chang, C.-L. Lo, W.-H. Chiang, H.-C. Chiu, IR780-loaded zwitterionic polymeric nanoparticles with acidity-induced agglomeration for enhanced tumor retention, Eur. Polym. J., (2019) 109400.

[40] K. Zhang, H. Fang, Z. Chen, J.-S.A. Taylor, K.L. Wooley, Shape effects of nanoparticles conjugated with cell-penetrating peptides (HIV Tat PTD) on CHO cell uptake, Bioconjugate Chem., 19 (2008) 1880-1887.

[41] D.B. Chithrani, Intracellular uptake, transport, and processing of gold nanostructures, Mol. Membr. Biol., 27 (2010) 299-311.

[42] D.S. Nikam, S.V. Jadhav, V.M. Khot, R. Ningthoujam, C.K. Hong, S.S. Mali, S. Pawar, Colloidal stability of polyethylene glycol functionalized Co 0.5 Zn 0.5 Fe 2 O 4 nanoparticles: effect of pH, sample and salt concentration for hyperthermia application, RSC Adv., 4 (2014) 12662-12671.

[43] L. Chen, L. Tan, S. Liu, L. Bai, Y. Wang, Surface modification by grafting of poly (SBMA-co-AEMA)-g-PDA coating and its application in CE, J. Biomater. Sci., Polym. Ed., 25 (2014) 766-785.

[44] C. Jiang, H. Cheng, A. Yuan, X. Tang, J. Wu, Y. Hu, Hydrophobic IR780 encapsulated in biodegradable human serum albumin nanoparticles for photothermal and photodynamic therapy, Acta Biomater., 14 (2015) 61-69.

[45] Z. Dong, J. Mao, M. Yang, D. Wang, S. Bo, X. Ji, Phase behavior of poly (sulfobetaine methacrylate)-grafted silica nanoparticles and their stability in protein solutions, Langmuir, 27 (2011) 15282-15291.

[46] H. Liu, K. Wang, C. Yang, S. Huang, M. Wang, Multifunctional polymeric micelles loaded with doxorubicin and poly(dithienyl-diketopyrrolopyrrole) for near-infrared light-controlled chemo-phototherapy of cancer cells, Colloids Surf., B, 157 (2017) 398-406.

[47] D.K. Kirui, D.A. Rey, C.A. Batt, Gold hybrid nanoparticles for targeted phototherapy and cancer imaging, Nanotechnology, 21 (2010) 105105.

[48] A. Yuan, X. Qiu, X. Tang, W. Liu, J. Wu, Y. Hu, Self-assembled PEG-IR-780-C13 micelle as a targeting, safe and highly-effective photothermal agent for in vivo imaging and cancer therapy, Biomaterials, 51 (2015) 184-193.

[49] K. Wang, Y. Zhang, J. Wang, A. Yuan, M. Sun, J. Wu, Y. Hu, Self-assembled IR780-loaded transferrin nanoparticles as an imaging, targeting and PDT/PTT agent for cancer therapy, Sci. Rep., 6 (2016) 27421.

[50] F. Guo, M. Yu, J. Wang, F. Tan, N. Li, The mitochondria-targeted and IR780-regulated theranosomes for imaging and enhanced photodynamic/photothermal therapy, RSC Adv., 6 (2016) 11070-11076.

[51] D. de Melo-Diogo, E.C. Costa, C.G. Alves, R. Lima-Sousa, P. Ferreira, R.O. Louro, I.J. Correia, POxylated graphene oxide nanomaterials for combination chemo-phototherapy of breast cancer cells, Eur. J. Pharm. Biopharm., 131 (2018) 162-169.

[52] C. Zhang, T. Liu, Y. Su, S. Luo, Y. Zhu, X. Tan, S. Fan, L. Zhang, Y. Zhou, T. Cheng, A near-infrared fluorescent heptamethine indocyanine dye with preferential tumor accumulation for in vivo imaging, Biomaterials, 31 (2010) 6612-6617.

[53] Y. Wang, T. Liu, E. Zhang, S. Luo, X. Tan, C. Shi, Preferential accumulation of the near infrared heptamethine dye IR-780 in the mitochondria of drug-resistant lung cancer cells, Biomaterials, 35 (2014) 4116-4124.

[54] A.F. Moreira, C.F. Rodrigues, C.A. Reis, E.C. Costa, P. Ferreira, I.J. Correia, Development of poly-2-ethyl-2-oxazoline coated gold-core silica shell nanorods for cancer chemo-photothermal therapy, Nanomedicine (London, U. K.), 13 (2018) 2611-2627.

[55] C.F. Rodrigues, C.A. Reis, A.F. Moreira, P. Ferreira, I.J. Correia, Optimization of gold core-mesoporous silica shell functionalization with TPGS and PEI for cancer therapy, Microporous Mesoporous Mater., 285 (2019) 1-12.

[56] S. Rajendrakumar, N.-C. Chang, A. Mohapatra, S. Uthaman, B.-I. Lee, W.-b. Tsai, I.-K. Park, A lipophilic ir-780 dye-encapsulated zwitterionic polymer-lipid micellar nanoparticle for enhanced photothermal therapy and nir-based fluorescence imaging in a cervical tumor mouse model, Int. J. Mol. Sci., 19 (2018) 1189.

Chapter 4: Poly(2-ethyl-2-oxazoline)-IR780 conjugate nanoparticles for breast cancer phototherapy

Research Work 2

This chapter is based on the publication: Poly(2-ethyl-2-oxazoline)-IR780 conjugate nanoparticles for breast cancer phototherapy
Nanomedicine, 2023, 17: 2057-2072

4.1. Abstract

IR780 is a prototypic heptamethine cyanine with Near-Infrared (NIR) light-triggered photothermal capacity. However, the low water solubility and acute toxicity of IR780 limit its translation. The preparation of hydrophilic polymer-IR780 conjugates may address these limitations. Herein, the cyclohexenyl ring of IR780 was conjugated, for the first time, with thiol-terminated poly(2-ethyl-2-oxazoline). This novel poly(2-ethyl-2-oxazoline)-IR780 conjugate (PEtOx-IR) was combined with D-α-tocopheryl succinate (TOS), leading to the assembly of mixed nanoparticles (PEtOx-IR/TOS NPs). The PEtOx-IR/TOS NPs displayed optimal colloidal stability as well as cytocompatibility towards healthy cells at doses within the therapeutic range. In turn, the combination of PEtOx-IR/TOS NPs with NIR light reduced heterotypic breast cancer spheroids' viability to just 15 %. Overall, the PEtOx-IR/TOS NPs are promising agents for breast cancer photothermal therapy.

Keywords: Cancer, Polymer-IR780 conjugate, Photothermal therapy, Poly(2-ethyl-2-oxazoline), Spheroids.

4.2. Introduction

Photo-activated materials have been showing promising results in cancer therapy [1, 2]. Such has been propelled by their ability to produce, upon interaction with light, a temperature increase (PTT) and/or reactive oxygen species (PDT), which can damage cancer cells [3, 4]. For this type of application, it is of extreme importance to use the first window of Near-Infrared (abbreviated as NIR; 750-1000 nm) light due to its suitable penetration depth and minimal interactions with biological components (*e.g.,* collagen, melanin, and water), ensuring minimal off-target effects [4, 5].

Owing to these reasons, the use of NIR absorbing agents is crucial in cancer PTT/PDT. In this context, the FDA-approval of ICG for angiography, as well as its NIR absorption, have driven its investigation for cancer phototherapy [6, 7]. However, the shortcomings of ICG (such as low fluorescence quantum yield and photodegradability) have motivated the development of other heptamethine cyanines [4, 8]. The properties of the different NIR-absorbing prototypic heptamethine cyanines were recently analyzed, being disclosed that IR780 holds a great potential due to its high NIR absorption, strong photothermal/photodynamic capabilities, and potential for cancer cell imaging [4]. Nevertheless, the direct use of IR780 for cancer PTT/PDT is limited by its low water solubility and cytotoxic profile [9].

The limitations of IR780 can be surpassed through the conjugation of its cyclohexenyl ring with hydrophilic polymers [10-12]. In fact, the preparation of hydrophilic polymer-IR780 conjugates leads to an improved solubility and cytocompatibility [10, 13]. Moreover, the amphiphilic nature of these hydrophilic polymer-IR780 conjugates enables their assembly into nanostructures [10, 11]. This re-arrangement of the polymer-IR780 conjugates' linear chains into nano-sized materials is of paramount importance due to the capacity of nanostructures with well-defined physicochemical properties to accumulate at the tumor site after intravenous administration [10, 14]. Moreover, the use of nanomaterials assembled using polymer-drug conjugates is often associated with a more controlled release profile and a higher drug loading capacity when compared to the direct loading of drugs into the nanomaterials' hydrophobic core [15-17].

In this work, a novel polymer-IR780 conjugate was prepared by attaching thiol-terminated Poly(2-ethyl-2-oxazoline) (PEtOx-SH) to the cyclohexenyl ring of IR780. PEtOx was selected due to its biocompatibility and capacity to reduce protein adsorption on nanomaterials' surface, hence improving the blood circulation time and

tumor uptake [18-23]. Moreover, PEtOx was also chosen as an alternative to PEG since several reports have highlighted that PEGylated nanomaterials can be immunogenic [24-26]. The PEtOx-IR780 conjugates were then combined with D-α-tocopheryl succinate (TOS), due to the ability of the latter to facilitate the assembly of nanoparticles by stabilizing the nanostructures' core [27].

4.3. Materials and Methods

4.3.1. Materials

IR780 Iodide, Poly(2-ethyl-2-oxazoline) α-benzyl ω-thiol terminated (PEtOx-SH; M_n = 10000 Da), TOS, Resazurin, Paraformaldehyde, Dulbecco's Modified Eagle's Medium F-12 (DMEM-F12), and Trypsin were acquired from Sigma-Aldrich (Sintra, Portugal). Acetone, Chloroform, Triton X-100, and Methanol were bought from Fisher Scientific (Oeiras, Portugal). Agarose was bought from GRiSP (Porto, Portugal). Michigan Cancer Foundation-7 (MCF-7) cell line was acquired from ATCC (Middlesex, UK) and Normal Human Dermal Fibroblast (NHDF) from Promocell (Heidelberg, Germany). Triethylamine was bought from TCI (Oxford, UK). Cell Imaging Plates were obtained from Ibidi GmbH (Munich, Germany). Calcein-AM, Hoechst 33342®, Propidium Iodide (PI), Cell Culture Plates, and T-flasks were purchased from Thermo Fisher Scientific (Porto, Portugal). Fetal Bovine Serum (FBS) was obtained from Biochrom AG (Berlin, Germany). Water used in all experiments was double deionized (0.22 μm filtered, 18.2 M Ω cm).

4.3.2. Methods

4.3.2.1. PEtOx-IR conjugate synthesis and characterization

The synthesis of the PEtOx-IR conjugate was performed by adapting protocols described elsewhere [13, 28]. Initially, IR780 (66.7 mg) and PEtOx-SH (40 mg) were dissolved in chloroform (50 mL) containing triethylamine (50 μL). A molar excess of IR780 to the available PEtOx-SH chains was used. The solution was left to stir for 48 h at room temperature. Then, chloroform was removed by evaporation (Rotavap® R-215, Büchi, Switzerland) and the obtained product was resuspended in methanol. Subsequently, a dialysis against methanol was performed (1 kDa molecular weight cut-off membrane) for 24 h to remove the non-conjugated IR780. After this process, the obtained methanolic

solution containing the PEtOx-IR conjugate was concentrated (by evaporation) and was stored at 4 °C.

The synthesis of the PEtOx-IR conjugate was confirmed by Fourier Transform Infrared Spectroscopy (FTIR; Nicolet iS10 spectrometer, Thermo Scientific Inc., MA, USA) and Proton Nuclear Magnetic Resonance (^{1}H NMR; Brüker Avance III 400 MHz spectrometer, Brüker Scientific Inc., NY, USA). For ^{1}H NMR analysis, IR780, PEtOx-SH, and PEtOx-IR conjugate were dissolved in deuterated chloroform. To analyze the NMR spectra, MNova software (Mestrelab Research, SL, Santiago de Compostela, Spain) was used.

4.3.2.2. Formulation of PEtOx-IR/TOS NPs and PEtOx-IR NPs

The nanoprecipitation technique was used to formulate PEtOx-IR/TOS NPs by adapting a protocol previously described [29]. First, 1 mL of acetone containing 0.5 mg of PEtOx-IR conjugate and 0.5 mg of TOS were added dropwise into 5 mL of Phosphate buffered saline (PBS), under constant stirring, for 2 h, at room temperature. Afterwards, the solution was recovered, dialyzed against water (0.5-1 kDa molecular weight cut-off membrane) for 90 min at room temperature, and filtered (0.45 μm pore size), yielding PEtOx-IR/TOS NPs. The same protocol was used to prepare the PEtOx-IR NPs (*i.e.*, the particles without TOS). In this case, only PEtOx-IR conjugate (0.5 mg) was added to the acetone solution and the filtration step was not performed.

4.3.2.3. Nanoparticles' physicochemical, optical, and photothermal characterization

Dynamic Light Scattering (DLS) was used to evaluate the size distribution (in water) of PEtOx-IR/TOS NPs and PEtOx-IR NPs (Zetasizer Nano ZS, Malvern Instruments LTD., Worcestershire, UK). The zeta potential (in DMEM-F12 medium supplemented with 10 % (v/v) FBS) of the nanoformulations was also determined. The morphology of PEtOx-IR/TOS NPs was characterized by Transmission Electron Microscopy (TEM; TECNAI G2 20 S-TWIN; FEI Company, Netherlands), operated at an accelerating voltage of 200 kV. For this analysis, the nanoparticles were first stained with phosphotungstic acid (2 % (w/v)).

The Incorporation Efficiency of the PEtOx-IR conjugate in PEtOx-IR/TOS NPs was determined by UV-Vis-NIR absorption spectroscopy. First, a standard curve of the PEtOx-IR conjugate in water:methanol (1:1 (v/v), at 780 nm) was performed (using an Evolution 201 spectrophotometer, Thermo Scientific Inc.). Then, PEtOx-IR/TOS NPs were freeze-dried (in a ScanVac CoolSafe, LaboGene ApS, Lynge, Denmark) and resuspended in water:methanol (1:1 (v/v)). Then, the concentration of PEtOx-IR conjugate was determined by analyzing the absorbance of the freeze-dried PEtOx-IR/TOS NPs' solution at 780 nm. Finally, the Incorporation Efficiency was determined according to the following equation:

$$Incorporation\ Efficiency\ (\%) = \frac{Weight\ of\ PEtOx\text{-}IR\ conjugate\ incorporated\ in\ PEtOx\text{-}IR/TOS\ NPs}{Weight\ of\ PEtOx\text{-}IR\ conjugate\ initially\ fed} \times 100$$

To evaluate the capacity of the PEtOx-IR/TOS NPs to interact with NIR light, their Vis-NIR absorption spectrum was investigated. For that, the absorption of PEtOx-IR/TOS NPs (at 5 μg mL^{-1} of PEtOx-IR conjugate equivalents; in water) and of PEtOx-IR conjugate (at 5 μg mL^{-1}; in methanol) were acquired.

To evaluate the colloidal stability of the PEtOx-IR/TOS NPs, their size variation and Vis-NIR absorption spectrum, when dispersed in water, PBS, and cell culture medium (DMEM-F12 supplemented with 10 % (v/v) FBS), were investigated for 48 h.

Finally, the photothermal capacity of PEtOx-IR/TOS NPs was evaluated by determining the temperature variations attained upon NIR laser irradiation (808 nm, 1.7 W cm^{-2}, 5 min) using a thermocouple thermometer. Irradiated water was used as control. To assess the photostability of PEtOx-IR/TOS NPs, their Vis-NIR absorption spectrum after each minute of NIR irradiation was acquired. Furthermore, the temperature variations induced by PEtOx-IR/TOS NPs (at 20 μg mL^{-1} of PEtOx-IR conjugate equivalents), measured at the 5^{th} minute of NIR laser exposure, along 5 cycles of irradiation, were also evaluated. A new irradiation cycle only started after complete cooling of the formulation to the room temperature.

4.3.2.4. Cytocompatibility of PEtOx-IR/TOS NPs and PEtOx-IR NPs towards 2D *in vitro* cultures

The cytocompatibility of PEtOx-IR/TOS NPs and PEtOx-IR NPs towards 2D *in vitro* cultures was evaluated using the resazurin method [30]. For this assay, MCF-7 (breast cancer cell model) and NHDF (normal cell model) were seeded in 96-well plates at a density of 1×10^4 cells/well. Both cell lines were cultured in DMEM-F12 medium supplemented with 10 % (v/v) FBS and 1 % (v/v) streptomycin/gentamycin in a humidified incubator (37 °C, 5 % CO_2). After 24 h, the culture medium was replaced with fresh medium containing different concentrations of PEtOx-IR/TOS NPs or PEtOx-IR NPs. Then, after 24 and 48 h, the medium was removed and fresh culture medium with 10 % (v/v) of resazurin was incubated for 4 h in the dark (37 °C, 5 % CO_2). Finally, to evaluate the viability of the cells, the fluorescence of resorufin ($\lambda_{ex}/\lambda_{em}$ of 560/590 nm) was measured in a Spectramax Gemini EM spectrofluorometer (Molecular Devices LLC, California, USA). As negative (K-) and positive (K+) controls, cells solely incubated with medium or ethanol (70 % (v/v)) were used, respectively.

4.3.2.5. Cellular uptake of PEtOx-IR/TOS NPs in 2D *in vitro* cancer models

Prior to evaluating the cellular uptake of PEtOx-IR/TOS NPs, the fluorescence emitted by this formulation was assessed in a spectrofluorometer (λ_{ex} = 633 nm and λ_{ex} = 780 nm). To evaluate the uptake of PEtOx-IR/TOS NPs by MCF-7 cells, 1×10^4 cells/well were seeded in 96-well plates. After 24 h, the cells were incubated with fresh medium containing PEtOx-IR/TOS NPs (at 2.5 μg mL^{-1} of PEtOx-IR conjugate equivalents) or IR780 (2.5 μg mL^{-1}). After 4 h, non-internalized nanoparticles were removed by washing cells with ice-cold Krebs Ringer Buffer. After that, cells were incubated for 30 min with Triton X-100 (1 % (v/v); in Krebs Ringer Buffer) to cause their lysis. To determine the PEtOx-IR/TOS NPs' uptake, the fluorescence of PEtOx-IR conjugate (present in the cell lysate) was analyzed in a spectrofluorometer ($\lambda_{ex}/\lambda_{em}$ of 780/800 nm). Cells only incubated with Krebs Buffer were used as a control.

To further observe the uptake of PEtOx-IR/TOS NPs, Confocal Laser Scanning Microscopy (CLSM) images were acquired (Zeiss LSM 710 confocal microscope, Carl Zeiss AG, Oberkochen, Germany). For that, MCF-7 cells were seeded (1.5×10^4 cells/well) in μ-slide 8-well imaging plates (Ibidi GmbH, Munich, Germany). Two days later, the medium was replaced with fresh one containing PEtOx-IR/TOS NPs (5 μg mL^{-1} of PEtOx-IR conjugate equivalents). After 4 h, the medium was removed, and several

washing steps were performed with PBS. Paraformaldehyde 4 % was used to fix cells for 15 min, at room temperature, and Hoescht 33342® was used to label the cells' nucleus for 45 min at 4 °C. The fluorescence images were acquired using $\lambda_{ex}/\lambda_{em}$ of 633/656-758 nm (to visualize IR780) and 405/410-499 (to visualize Hoechst 33342®).

4.3.2.6. Phototherapeutic effect mediated by PEtOx-IR/TOS NPs in 2D *in vitro* cancer models

The phototherapeutic effect of PEtOx-IR/TOS NPs in 2D *in vitro* cancer models was evaluated as previously reported [29]. First, MCF-7 cells were seeded as described in 4.3.2.4. After 24 h, the culture medium was replaced by fresh medium containing PEtOx-IR/TOS NPs at 2.5 and 5 μg mL^{-1} (of PEtOx-IR conjugate equivalents). After 4 h, the cells were exposed to NIR irradiation (808 nm, 1.7 W cm^{-2}, 5 min). After reaching a total of 24 h of incubation with the nanomaterials, the cells' viability was measured using the resorufin fluorescence as described above.

CLSM images were also acquired to visualize the phototherapeutic effect of PEtOx-IR/TOS NPs. MCF-7 cells were seeded in μ-slide 8-well imaging plates as described in section 4.3.2.5. Then, cells were incubated in fresh medium containing PEtOx-IR/TOS NPs (at 2.5 and 5 μg mL^{-1} of PEtOx-IR conjugate equivalents). After 4 h, cells were irradiated with NIR light (808 nm, 1.7 W cm^{-2}, 5 min). Then, the medium was removed, and live and dead cells were stained with Calcein-AM and PI, respectively, for 15 min (according to the manufacturer's protocol). Fluorescence images were acquired using a $\lambda_{ex}/\lambda_{em}$ of 488/493-556 (to visualize Calcein-AM) and 561/566-719 nm (to visualize PI). Cells solely incubated with culture medium were used as the control for live cells.

4.3.2.7. Penetration capacity of PEtOx-IR/TOS NPs in 3D *in vitro* cancer models

Heterotypic spheroids were produced as previously described [9, 31]. In brief, agarose structures (2 % (w/v)) with round-bottom microwells were produced using a micro-mold (3D Petri Dish, Microtissues Inc., Providence RI, USA). Then, 1×10^6 MCF-7 cells and NHDF (at a cell ratio of 1:1) were seeded per structure, forming 81 spheroids per agarose construct. Every 2 days, the medium was replaced with fresh medium (DMEM-F12 medium supplemented with 10 % (v/v) of FBS and 1 % (v/v) of

streptomycin/gentamicin). Spheroids were left to grow for 10 days, being maintained in an incubator with a humidified atmosphere (37 °C, 5 % CO_2).

To visualize the penetration of the nanoparticles into the spheroids, these were incubated with fresh medium containing PEtOx-IR/TOS NPs (7.5 μg mL^{-1} of PEtOx-IR conjugate equivalents). After 24 h, spheroids were fixed with paraformaldehyde 4 % overnight and the nanoparticles' penetration capacity was visualized by CLSM using $\lambda_{ex}/\lambda_{em}$ of 633/656-758 nm (to visualize IR780). The Fluorescence Intensity plots across the diameter of the spheroid, at different z-stacks, were determined using the ImageJ software as previously described [31].

4.3.2.8. Phototherapeutic effect mediated by PEtOx-IR/TOS NPs in 3D *in vitro* cancer models

To evaluate the phototherapeutic capacity of PEtOx-IR/TOS NPs in 3D *in vitro* cancer models, spheroids were produced and maintained as described above. After 10 days of growing, PEtOx-IR/TOS NPs (at 7.5 and 15 μg mL^{-1} of PEtOx-IR conjugate equivalents) in fresh medium were incubated in the spheroids for 24 h. Then, spheroids were irradiated with NIR light (808 nm, 1.7 W cm^{-2}, 5 min). After 48 h, spheroids' viability was evaluated through the resazurin method as described above (section 4.3.2.4.). Each experimental condition was evaluated in 30 spheroids.

To visualize the phototherapeutic effect in spheroids, these were incubated with PEtOx-IR/TOS NPs (15 μg mL^{-1} of PEtOx-IR conjugate equivalents). After 24 h, spheroids were irradiated with NIR light (808 nm, 1.7 W cm^{-2}, 5 min). Finally, Calcein-AM/PI was used to stain spheroids. Fluorescence images were acquired as described in 4.3.2.6. Spheroids solely incubated with culture medium were used as the control for non-treated spheroids.

4.3.2.9. Statistical Analysis

To compare the multiple groups, a one-way Analysis of Variance (ANOVA) with the Student-Newman-Keuls test was used. The statistical analysis of two groups was performed using the unpaired *t-student* test. GraphPad Prism v6.0 (Trial version, GraphPad Software, CA, USA) was used to perform data analysis. A value of $p < 0.05$ was considered statistically significant.

4.4. Results and Discussion

4.4.1. Synthesis and characterization of PEtOx-IR conjugate

Initially, the PEtOx-IR conjugate was synthesized by binding the cyclohexenyl ring of IR780 with the thiol group of PEtOx-SH [13]. The FTIR analysis was performed to confirm the successful synthesis of the PEtOx-IR conjugate (**Figure 4.1**). The FTIR spectrum of IR780 showed peaks at 1514 and 757 cm^{-1} corresponding to the benzene ring stretch and the C-H bending, respectively (Figure 4.1). On the other hand, the PEtOx-SH spectrum displayed its characteristic peak at 1628 cm^{-1} (amides' C=O stretch) (Figure 4.1). The FTIR spectrum of the PEtOx-IR conjugate presented the above described IR780 and PEtOx-SH peaks (Figure 4.1).

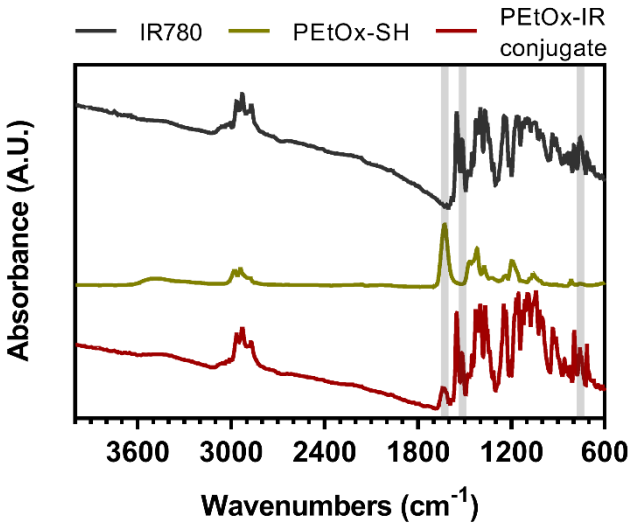

Figure 4.1. FTIR spectra of IR780, PEtOx-SH, and PEtOx-IR conjugate.

Afterwards, ^{1}H NMR analysis was also performed to confirm the PEtOx-IR conjugate's synthesis. The ^{1}H NMR spectrum of IR780 showed a peak at 8.33 ppm belonging to the methine protons (C=C**H**) of the IR780' benzene ring as well as peaks at 7.16 and 6.24 ppm corresponding to the methine protons (C-C**H**=C**H**-C) of the IR780' heptamethine chain (**Figure 4.2**A). Finally, the 1.72 ppm peak corresponding to methyl (CH_3) protons of IR780 was also observed (Figure 4.2A) [13]. Furthermore, the PEtOx spectrum displayed peaks at 3.48 and 2.43 ppm corresponding to the methylene protons (-N-CH_2 and -CH_2-CH_3) as well as at 1.12 ppm belonging to the methyl protons

(-CH_2-C**H**$_3$) (Figure 4.2B) [32, 33]. The ^{1}H NMR spectrum of PEtOx-IR conjugate presented the above-described peaks of IR780 as well as those from PEtOx-SH (Figure 4.2C). Together, this data confirms the successful synthesis of the PEtOx-IR conjugate.

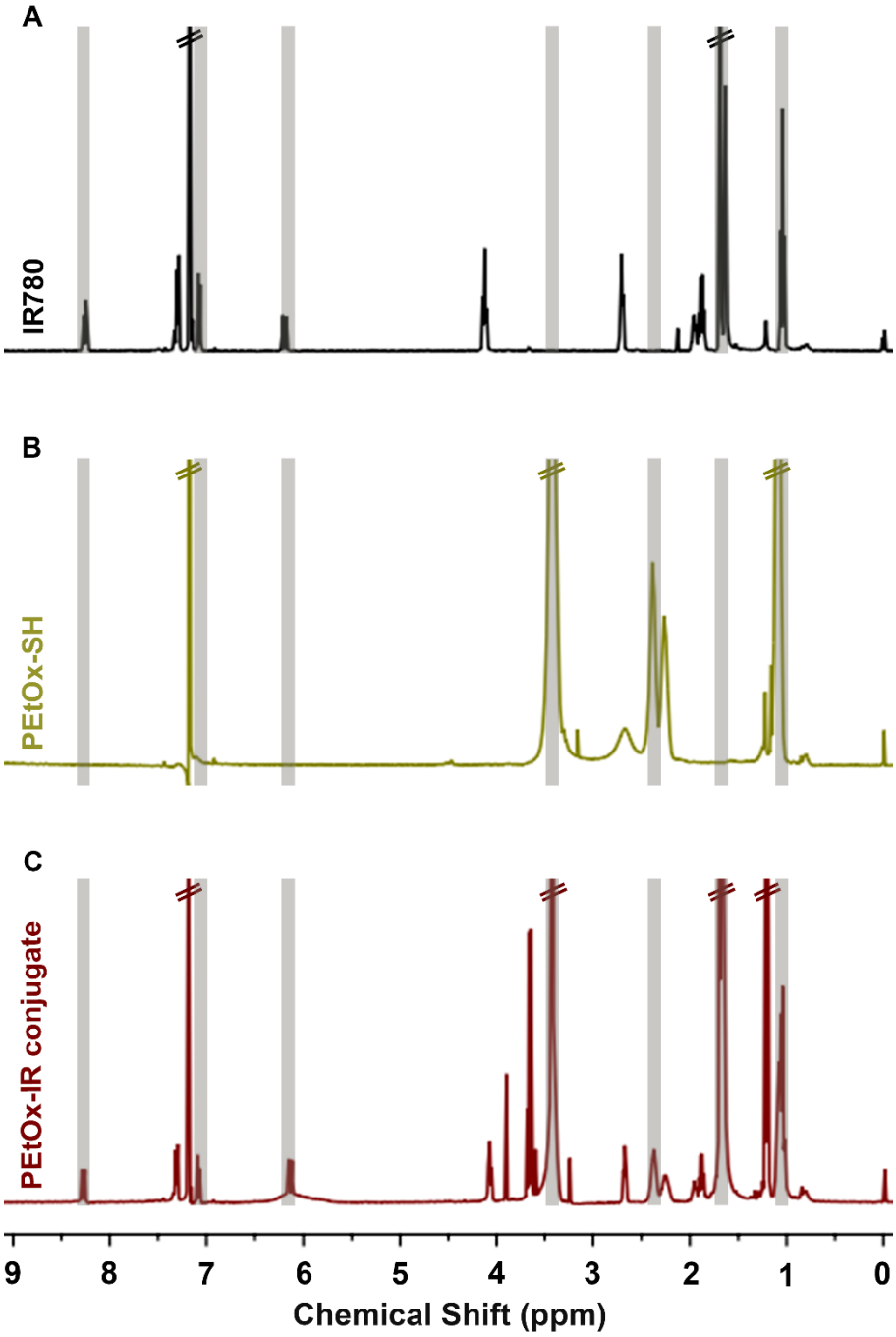

Figure 4.2. ^{1}H NMR characterization of PEtOx-IR conjugate. ^{1}H NMR spectra of IR780 (A), PEtOx-SH (B), and PEtOx-IR conjugate (C) dissolved in deuterated chloroform.

4.4.2. Formulation and characterization of PEtOx-IR/TOS NPs

After the successful synthesis of the PEtOx-IR780 conjugate, this polymer was used to produce nanoparticles through a simple nanoprecipitation technique - PEtOx-IR NPs (**Figure 4.3**A).

Surprisingly, the PEtOx-IR NPs presented sizes between 712 and 1990 nm (average size of 1092.0 ± 197.9 nm; Polydispersity Index (PDI) of 0.293; batch triplicates; Figure 4.3B). Therefore, the dimensions of PEtOx-IR NPs are not within the optimal size distribution for passive tumor accumulation (100-200 nm) [9, 34]. Such may be correlated with subpar hydrophobic-hydrophobic interactions occurring in the particles' core which cannot drive the assembly of nanostructures.

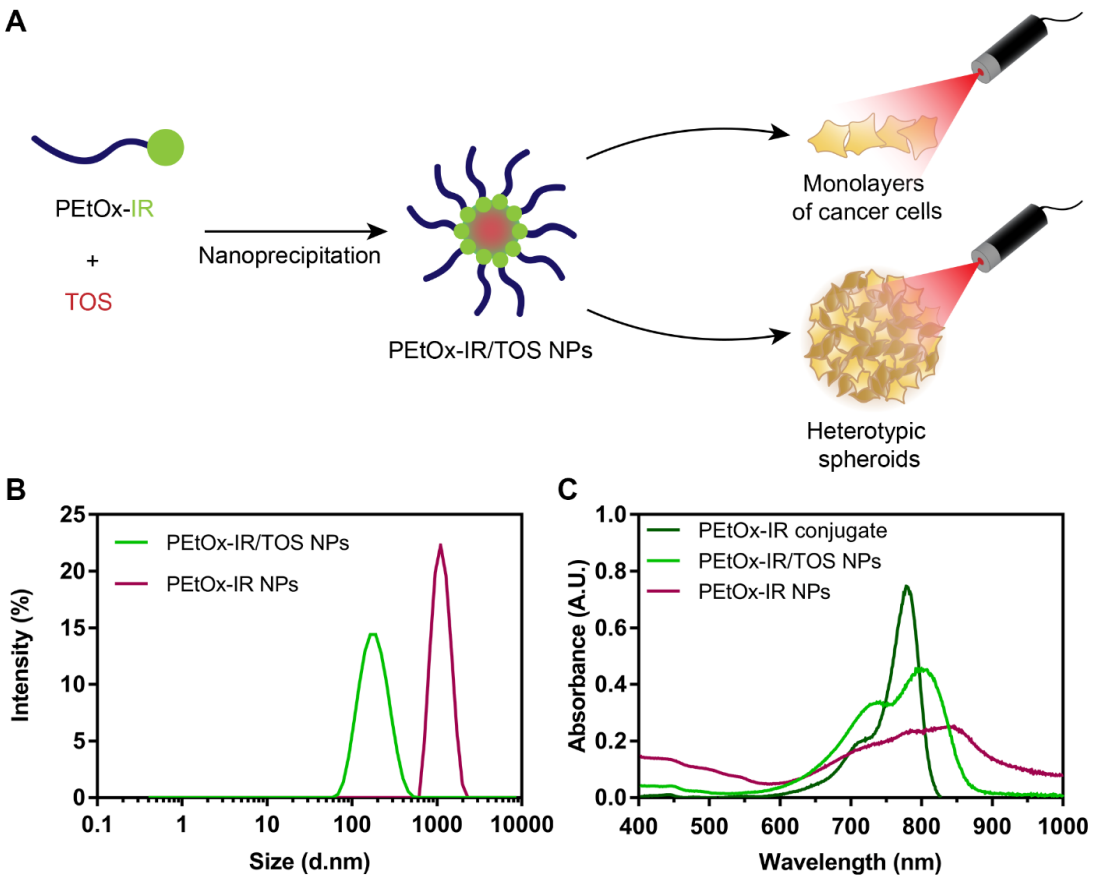

Figure 4.3. Formulation and characterization of PEtOx-IR/TOS NPs. Schematic representation of the nanoparticles' formulation and application in cancer phototherapy (A). DLS size distribution of PEtOx-IR/TOS NPs and PEtOx-IR NPs (B). Vis-NIR spectra of PEtOx-IR conjugate (5 μg mL^{-1}, in methanol), PEtOx-IR/TOS NPs, and PEtOx-IR NPs (in water), both at 5 μg mL^{-1} (of PEtOx-IR conjugate equivalents) (C).

To address this problem, TOS was also incorporated into the formulation due to its capacity to stabilize the nanomaterials' core (PEtOx-IR/TOS NPs). The PEtOx-IR/TOS NPs presented a size of 189.7 ± 4.4 nm (batch triplicates), which is suitable for their accumulation at the tumor site [35], as well as a low PDI (0.164) (Figure 4.3B). In a previous work, Pais-Silva observed that the incorporation of TOS in micelles formulated with PEGylated Vitamin E improves their size distribution [27]. The PEtOx-IR/TOS NPs were then imaged by TEM, revealing a spherical shape (**Figure 4.4**). Such morphology is consistent with that of other IR780-based nanomaterials reported in the literature, being appealing since spherically-shaped nanostructures may display an enhanced cellular uptake [36-41]. The PEtOx-IR/TOS NPs displayed a zeta potential of -7.8 ± 0.9 mV, which is also within the range considered ideal for cancer-related applications (-10 to +10 mV) [29, 42]. The Incorporation Efficiency of the PEtOx-IR conjugate in PEtOx-IR/TOS NPs was 39 ± 3 % (n = 5), being in line with that of other IR780-based nano-formulations [9, 43].

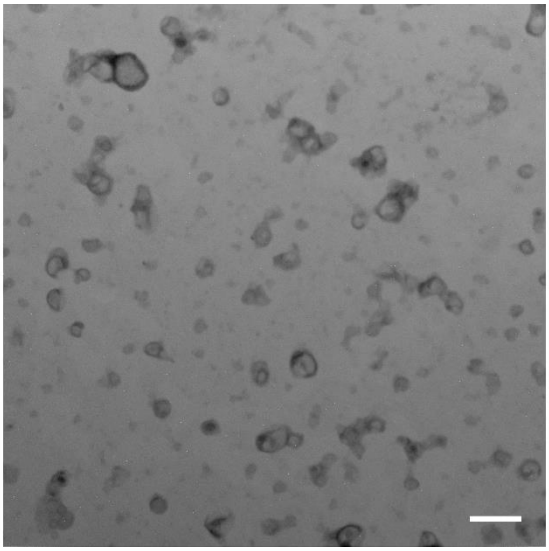

Figure 4.4. TEM image of PEtOx-IR/TOS NPs. Scale bar corresponds to 500 nm.

Subsequently, the NIR absorption of PEtOx-IR/TOS NPs was evaluated (Figure 4.3C). When compared to PEtOx-IR conjugate, the absorption of PEtOx-IR/TOS NPs had a red-shift. Due to this reason, the PEtOx-IR/TOS NPs had a 2.74-fold higher absorption at 808 nm when compared to the PEtOx-IR conjugate. Since 808 nm light will be used in photothermal experiments, the PEtOx-IR/TOS NPs may display a great photothermal capacity due to their higher absorption at 808 nm. Interestingly, the PEtOx-IR NPs had

a 1.89 times weaker absorption at this wavelength when compared to PEtOx-IR/TOS NPs. Considering that the hydrophobic-hydrophobic interactions occurring in the nanoparticles' core can drive the red-shift of IR780-based nanomaterials [27, 44-47], these results further support the incorporation of TOS in PEtOx-IR/TOS NPs.

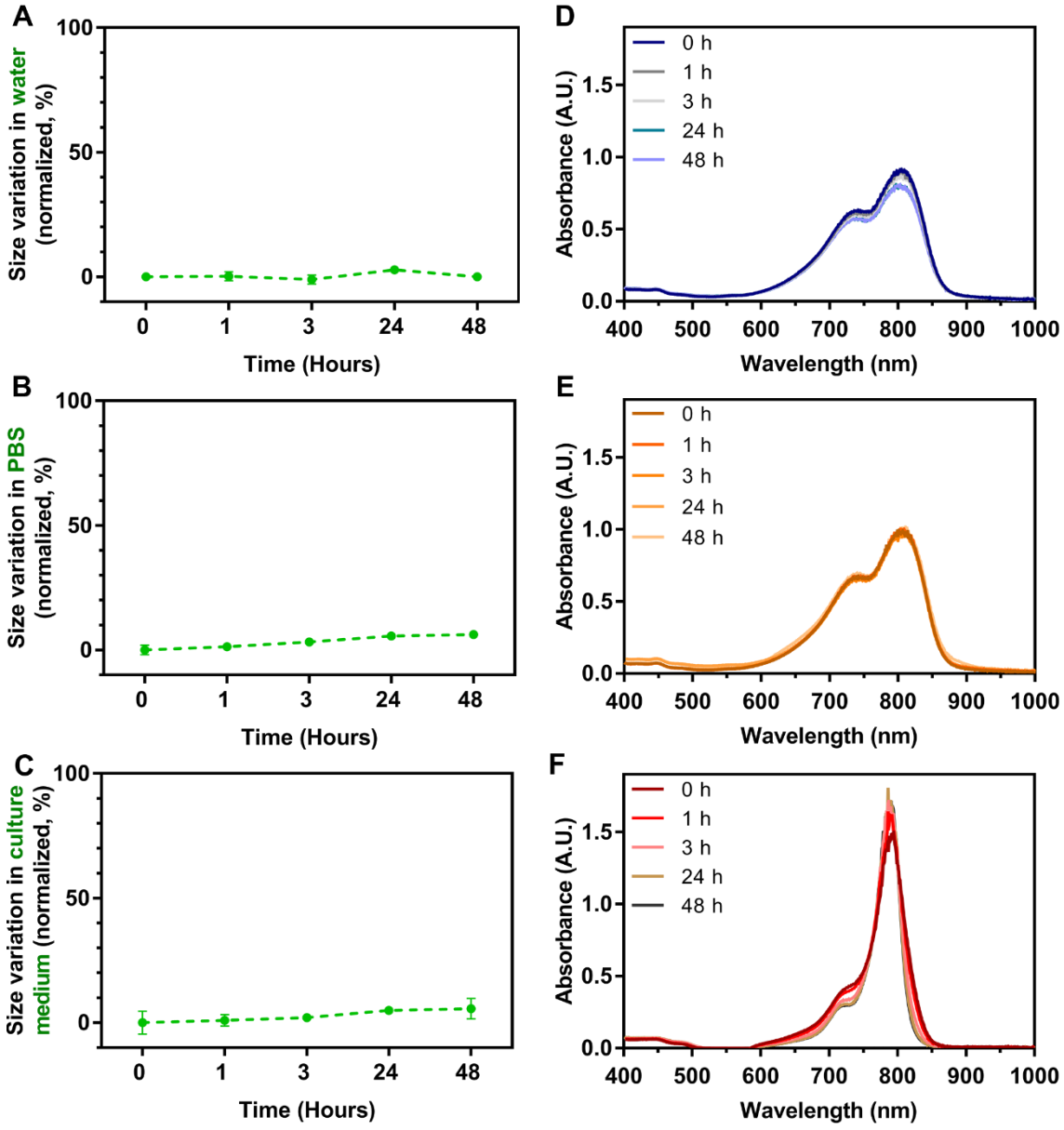

Figure 4.5. Stability of PEtOx-IR/TOS NPs. Size variation of PEtOx-IR/TOS NPs over time when dispersed in water (A), PBS (B), and cell culture medium (C). The values were normalized using the respective initial size (t = 0 h). Each bar represents mean ± S.D. (n = 3). Vis-NIR spectra of PEtOx-IR/TOS NPs in water (D), PBS (E), and cell culture medium (F), at different time points.

Then, the colloidal stability of the PEtOx-IR/TOS NPs was evaluated by dispersing them in water, PBS, and cell culture medium (DMEM-F12 supplemented with 10 % (v/v) of FBS; **Figure 4.6**). The size and NIR absorption of PEtOx-IR/TOS NPs did not suffer any meaningful variation over time (**Figure 4.5**), indicating that the PEtOx-IR/TOS NPs present good colloidal stability. In contrast, the NIR absorption of PEtOx-IR NPs decreased over time (Figure 4.6). This phenomenon was also accompanied by evident changes in the color of the PEtOx-IR NPs' solution (**Figure 4.7**).

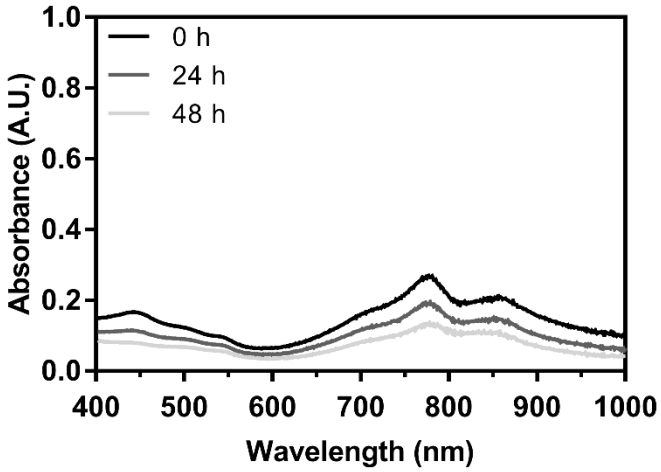

Figure 4.6. Vis-NIR absorption spectra of PEtOx-IR NPs over a 48 h period (in water).

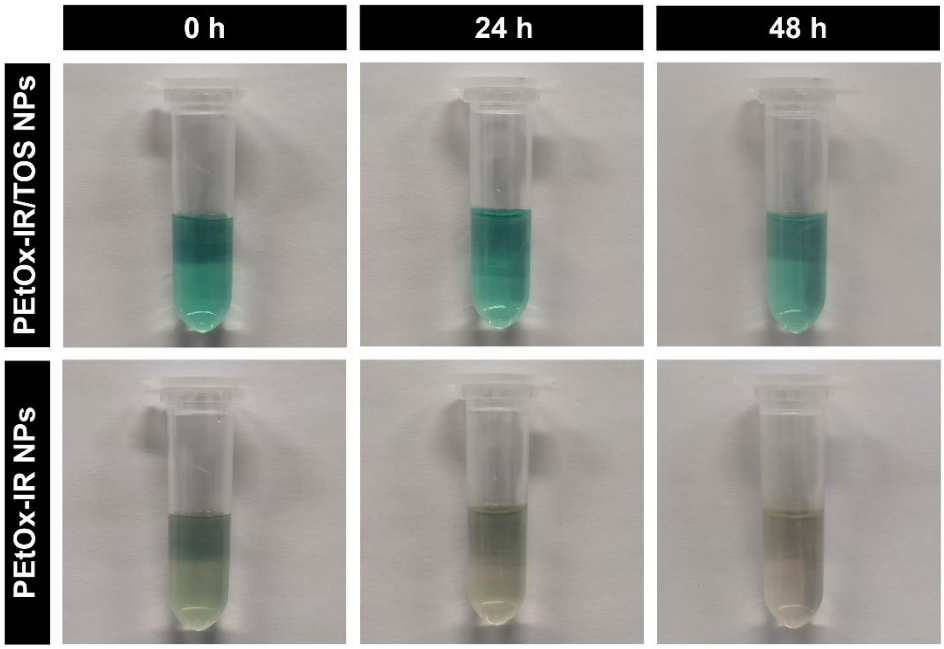

Figure 4.7. Macroscopic images of PEtOx-IR/TOS NPs and PEtOx-IR NPs, in water, over a 48 h period.

Finally, to evaluate the photothermal capacity of PEtOx-IR/TOS NPs, the temperature changes mediated by this nanoformulation after NIR irradiation (808 nm, 1.7 W cm^{-2}, 5 min) were recorded (**Figure 4.8**A).

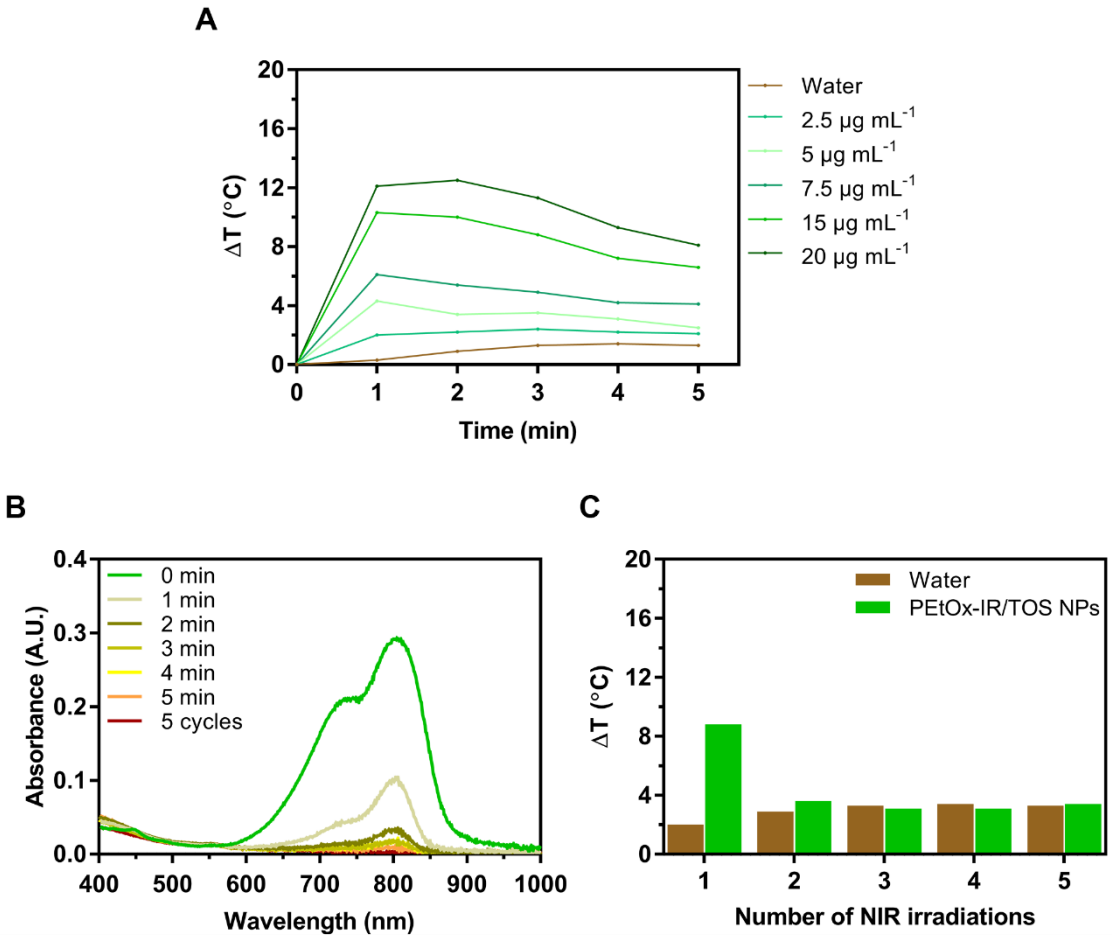

Figure 4.8. Temperature variation curves mediated by PEtOx-IR/TOS NPs (at different concentrations of PEtOx-IR conjugate equivalents) after irradiation with NIR light (808 nm, 1.7 W cm^{-2}) during a 5 min period (A). Vis-NIR spectrum of PEtOx-IR/TOS NPs (in water) during 5 minutes of NIR laser irradiation (808 nm, 1.7 W cm^{-2}), and after 5 cycles of NIR laser exposure (B). Temperature variations induced by PEtOx-IR/TOS NPs (at 20 μg mL^{-1} of PEtOx-IR conjugate equivalents), measured at the 5th minute of NIR laser exposure (808 nm, 1.7 W cm^{-2}, 5 min), along the different irradiation cycles (C).

The PEtOx-IR/TOS NPs produced a concentration-dependent photoinduced heat, achieving the maximum temperature increase after 1-2 min of irradiation. At the concentration of 20 μg mL^{-1} (of PEtOx-IR conjugate equivalents), the PEtOx-IR/TOS NPs produced a temperature increase of 12.5 °C after 2 min of exposure to NIR light, which can potentially cause cellular damage [4, 48]. The response of water (control) to NIR light was not meaningful ($\Delta T < 1.4$ °C), which is in agreement with the low

interaction of NIR light with water [4]. The highest photoinduced heat generated by PEtOx-IR/TOS NPs within the first two minutes of NIR laser exposure may be correlated with the photodegradation of IR780 by NIR light [9, 11, 49, 50]. To confirm this hypothesis, the absorption spectrum of PEtOx-IR/TOS NPs after each minute of laser exposure was analyzed, being verified that the optical properties of this formulation in the NIR are gradually lost (Figure 4.8B). Due to this reason, the PEtOx-IR/TOS NPs were not capable of producing a photothermal effect greater than the control after multiple NIR laser irradiation cycles (Figure 4.8C). Nevertheless, this behavior displayed by PEtOx-IR/TOS NPs may be an important feature since the photodegradation products of IR780 were reported to be cytocompatible [13], hence possibly avoiding issues related with the long term accumulation of photothermal nanoagents.

Together, these results confirm that the PEtOx-IR/TOS NPs have improved physicochemical and optical properties.

4.4.3. Evaluation of PEtOx-IR/TOS NPs' cytocompatibility in 2D *in vitro* cultures

Subsequently, the cytocompatibility of PEtOx-IR NPs and PEtOx-IR/TOS NPs towards 2D *in vitro* cultures of NHDF (normal cell line) and MCF-7 cells (breast cancer cell line) was evaluated (**Figure 4.9**). NHDF exposed to PEtOx-IR NPs for 24 and 48 h displayed a viability superior to 76 % (Figure 4.9A). MCF-7 cells incubated with PEtOx-IR NPs up to 5 μg mL^{-1} (of PEtOx-IR conjugate equivalents) also remained highly viable (Figure 4.9B). For higher doses of PEtOx-IR NPs (7.5 and 10 μg mL^{-1} of PEtOx-IR conjugate equivalents), the viability of the MCF-7 cells was affected (Figure 4.9B). This cytotoxicity is likely correlated with the propensity of IR780 to accumulate in the mitochondria of these cells [51] and it has also been reported for other IR780-based nanomedicines [27, 52].

NHDF and MCF-7 cells incubated with PEtOx-IR/TOS NPs, during 24 h, up to 5 μg mL^{-1} (of PEtOx-IR conjugate equivalents), remained with a viability of 82 % and 80 % respectively (Figure 4.9C and 4.9D). An incubation period for 48 h with this same dose of PEtOx-IR/TOS NPs revealed a close effect on NHDF (viability of 83 %) and a small decrease on MCF-7 cells' viability (to 65 %). However, the incubation of both cell lines with greater doses of PEtOx-IR/TOS NPs (7.5 and 10 μg mL^{-1} of PEtOx-IR conjugate equivalents) led to a high cytotoxicity. Considering the behavior of PEtOx-IR NPs, the safety profile of PEtOx-IR/TOS NPs, at high doses, appears to be mainly influenced by

TOS. In fact, TOS has been reported to produce reactive oxygen species, which can affect both cell lines [53-57]. Considering this data, when assessing the internalization and phototherapeutic capacity of PEtOx-IR/TOS NPs in 2D *in vitro* cancer models (section 4.4.4.), only doses of 2.5 and 5 μg mL^{-1} (of PEtOx-IR conjugate equivalents) were used to ensure that the observed effects are not masked by the TOS' action.

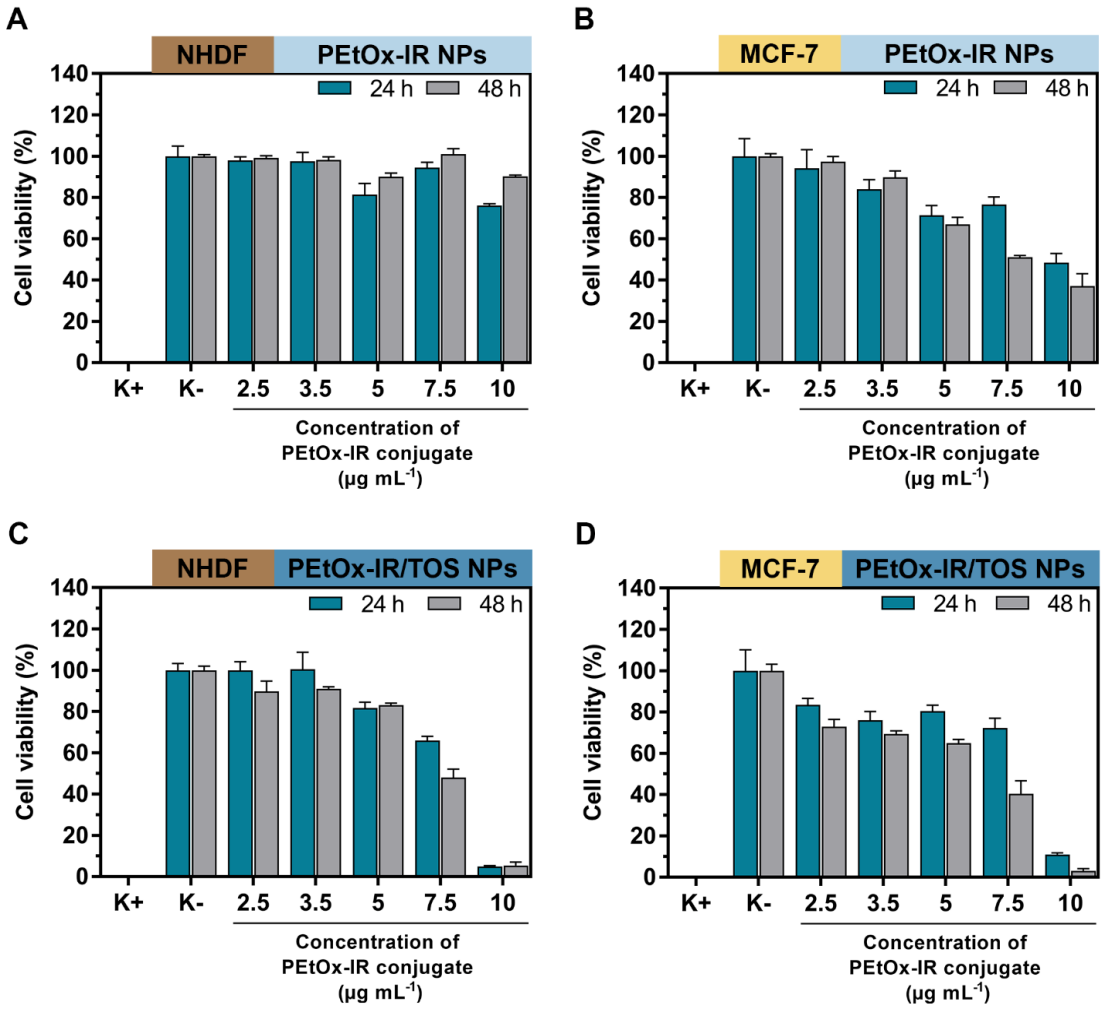

Figure 4.9. Cytocompatibility of PEtOx-IR NPs and PEtOx-IR/TOS NPs. Evaluation of the cell viability of NHDF (A) and MCF-7 cells (B) after incubation with PEtOx-IR NPs (at different concentrations of PEtOx-IR conjugate equivalents) for 24 and 48 h. Cell viability of NHDF (C) and MCF-7 cells (D) after incubation with PEtOx-IR/TOS NPs for 24 and 48 h. Positive control (K+) was cells treated with ethanol (70 % (v/v)) and negative control (K-) was cells only incubated with cell culture medium. Data are presented as mean ± S.D (n = 5).

4.4.4. Determination of PEtOx-IR/TOS NPs' ability to be internalized in cancer cells and phototherapeutic capacity

Then, the capacity of PEtOx-IR/TOS NPs to be internalized by monolayers of cancer cells (2D *in vitro* cancer cell model) was investigated. For such, the fluorescence emitted by PEtOx-IR/TOS NPs that derives from the IR780 molecule present on the PEtOx-IR conjugate was analyzed (**Figure 4.10**A).

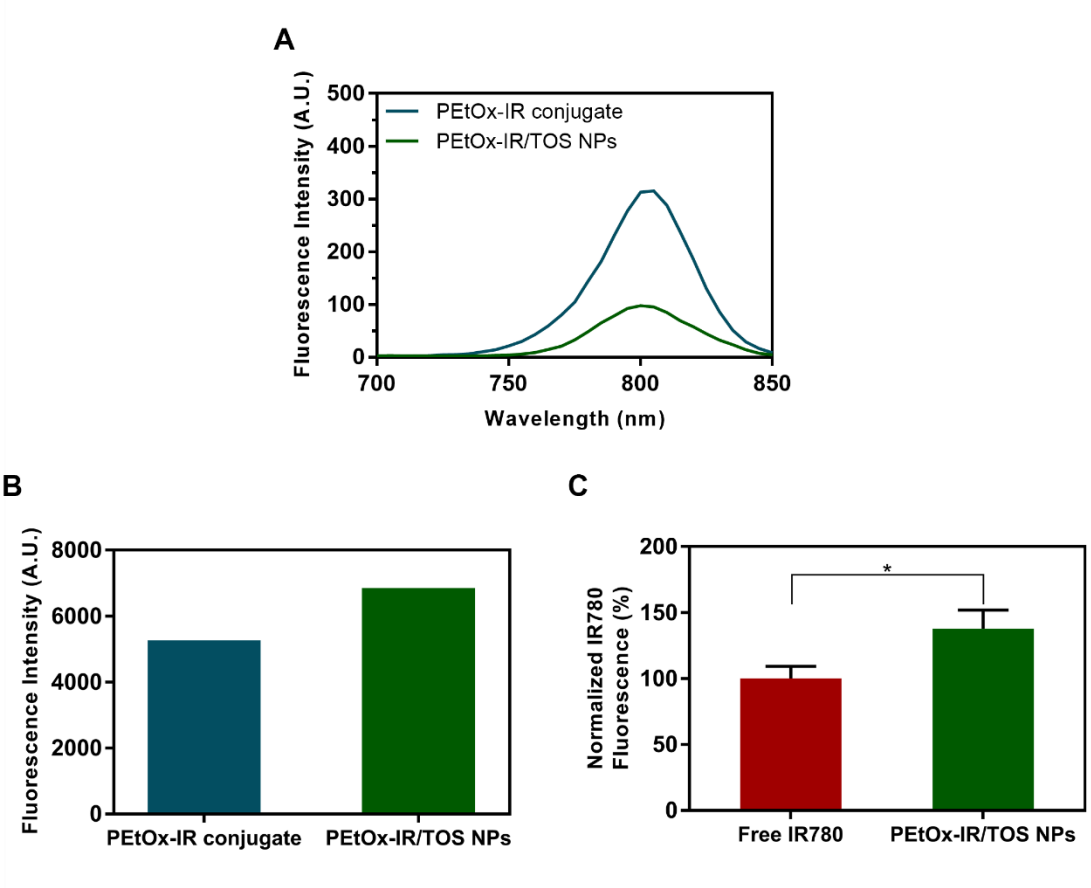

Figure 4.10. Fluorescence emission and uptake of PEtOx-IR/TOS NPs. Fluorescence emission spectra of PEtOx-IR conjugate (in methanol) and PEtOx-IR/TOS NPs (in cell culture medium), using an excitation wavelength of 633 nm (A). Fluorescence intensity emitted by PEtOx-IR conjugate (in methanol) and PEtOx-IR/TOS NPs (in cell culture medium) at 800 nm, using an excitation wavelength of 780 nm (B). Uptake of PEtOx-IR/TOS NPs (2.5 μg mL^{-1} of PEtOx-IR conjugate equivalents) by MCF-7 cells (C). The fluorescence values were normalized using the values of cells incubated with free IR780 (2.5 μg mL^{-1}).

CLSM images revealed that MCF-7 cells incubated with PEtOx-IR/TOS NPs display IR780 fluorescence signals in the cytoplasm, demonstrating the ability of the nanoformulations to become internalized in the cancer cells (**Figure 4.11**). This result was further confirmed by analyzing the IR780 Fluorescence Intensity in the MCF-7 cells incubated with PEtOx-IR/TOS NPs (Figure 4.10B and 4.10C).

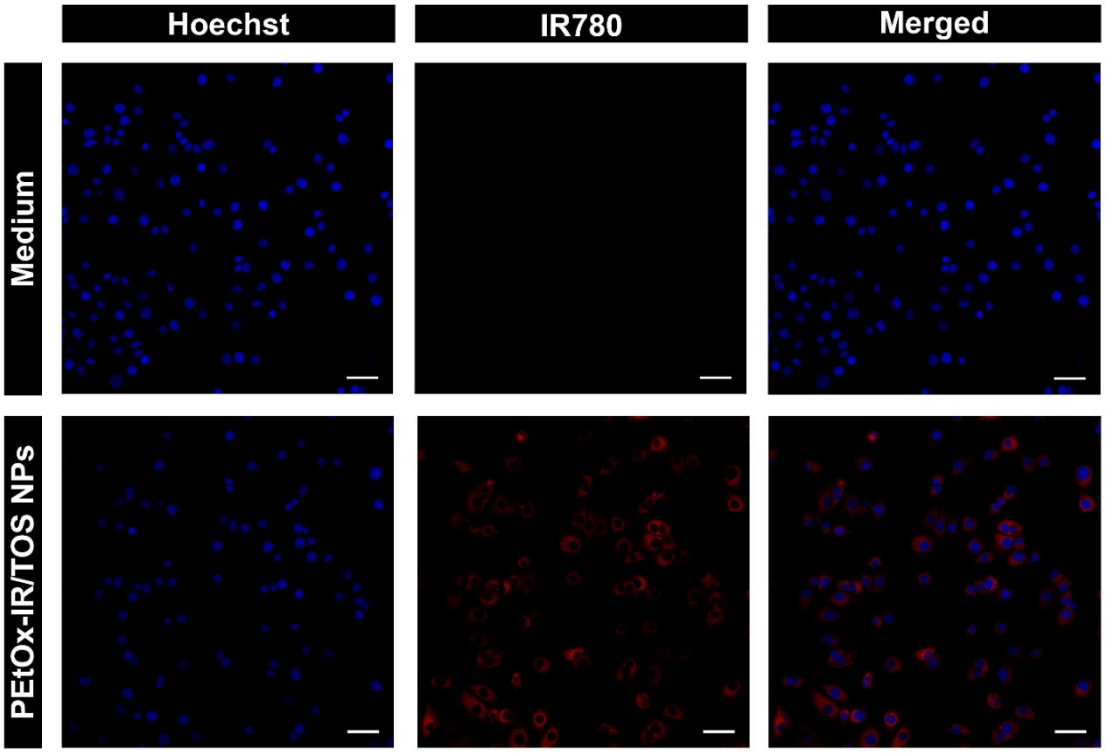

Figure 4.11. Uptake of PEtOx-IR/TOS NPs (5 μg mL^{-1} of PEtOx-IR conjugate equivalents) by MCF-7 cells. Blue channel: Hoechst 33342® stained nucleus, red channel: IR780. Scale bars correspond to 50 μm.

After confirming the PEtOx-IR/TOS NPs' capacity to be internalized by cancer cells, their phototherapeutic capacity was determined (**Figure 4.12**A). In line with the previous observations, MCF-7 cells solely exposed to NIR light, or non-irradiated PEtOx-IR/TOS NPs remained highly viable (> 80 %; Figure 4.12B). In stark contrast, the combination of NIR light and PEtOx-IR/TOS NPs at 2.5 μg mL^{-1} (of PEtOx-IR conjugate equivalents) could reduce MCF-7 cells' viability to 20 %. By further increasing the concentration to 5 μg mL^{-1} (of PEtOx-IR conjugate equivalents), the photothermal heating induced by PEtOx-IR/TOS NPs reduced the cancer cells' viability to just 9 % (Figure 4.12B).

These results were also confirmed by imaging the MCF-7 cells stained with Calcein-AM/PI (labels live/dead cells) after the different treatments (Figures 4.12 C and D). As expected, the CLSM images revealed Calcein-AM fluorescence on the vast majority

of the cancer cells exposed to only NIR light or to non-irradiated PEtOx-IR/TOS NPs. In turn, cancer cells were almost exclusively stained with PI upon exposure to PEtOx-IR/TOS NPs plus NIR light.

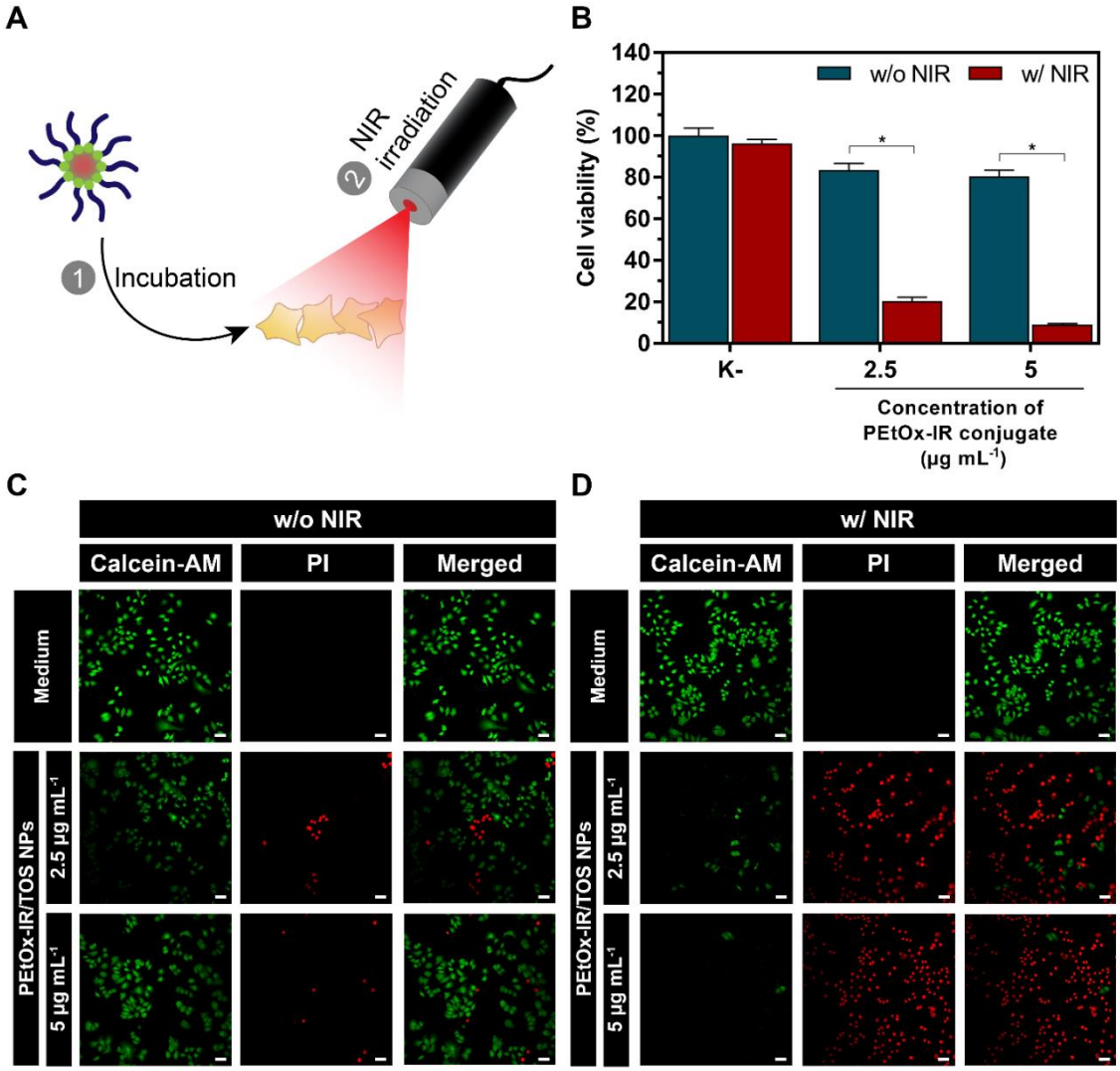

Figure 4.12. Phototherapeutic effect of PEtOx-IR/TOS NPs in 2D *in vitro* cancer models. Schematic representation of the therapeutic procedure (A). Evaluation of the effect induced by PEtOx-IR/TOS NPs (at different concentrations of PEtOx-IR conjugate equivalents) without (w/o NIR) and with NIR laser irradiation (w/ NIR, 808 nm, 1.7 W cm^{-2}, 5 min) on the viability of MCF-7 cells (B). Negative control (K- w/o NIR) was cells only incubated with culture medium. K- w/ NIR represents cells solely exposed to NIR light. Data are presented as mean ± S.D, n = 5 (*$p < 0.0001$). CLSM images of MCF-7 cells stained with Calcein-AM/PI after exposure to PEtOx-IR/TOS NPs w/o NIR (C) or w/ NIR laser irradiation (D). Medium w/o NIR represents the control for live cells and medium w/ NIR represents cells solely exposed to NIR light. Green channel: Calcein-AM, red channel: PI. Scale bars correspond to 50 μm.

Liu *et al.* produced IR780- and Perfloropentane loaded PEGylated nanoparticles, revealing their ability to reduce B16 cells' viability to about 55 % upon NIR irradiation (808 nm, 2 W cm^{-2}, 5 min; 35.4 μg mL^{-1} of IR780 equivalents) [58]. Song *et al.* produced IR780 loaded folate-targeted nanoparticles that prompted a reduction in SKOV3 cells' viability to 16 % after NIR irradiation (808 nm, 1 W cm^{-2}, 3 min, 40 μg mL^{-1} of nanoparticles) [59]. In this work, the PTT mediated by PEtOx-IR/TOS NPs could decrease MCF-7 cells' viability to 9 % (808 nm, 1.7 W cm^{-2}, 5 min; 5 μg mL^{-1} of PEtOx-IR conjugate equivalents), hence validating their phototherapeutic capacity.

4.4.5. Evaluation of PEtOx-IR/TOS NPs' penetration and phototherapeutic effect in heterotypic spheroids

Then, the performance of PEtOx-IR/TOS NPs was screened using heterotypic spheroids. This 3D *in vitro* cancer cell model was established using MCF-7 cells and NHDF in order to mimic breast tumors' cellular heterogeneity [60]. Moreover, spheroids' 3D structure, cell-cell interactions, and layered organization grant them resistance patterns to therapeutics/nanomedicines' penetration and action, similar to those occurring in *in vivo* solid tumors [61, 62]. Therefore, it is of utmost importance to use spheroids in the screening of the nanomaterials' therapeutic capacity [63].

Initially, the capacity of PEtOx-IR/TOS NPs to penetrate into the spheroid was investigated (**Figure 4.13**A). For such, spheroids were incubated with the PEtOx-IR/TOS NPs, and CLSM images at different z-stacks were acquired as well as the respective Fluorescence Intensity plots (Figure 4.13A). Fluorescence signals could be observed in the spheroids, indicating the ability of PEtOx-IR/TOS NPs to penetrate into these 3D cellular aggregates. A closer inspection revealed that the fluorescence was mostly located at the spheroids' periphery (Figure 4.13A). Such behavior results from the spheroids' resistance to nanomedicines' penetration, and it has been reported for other types of nanomaterials [31, 64, 65].

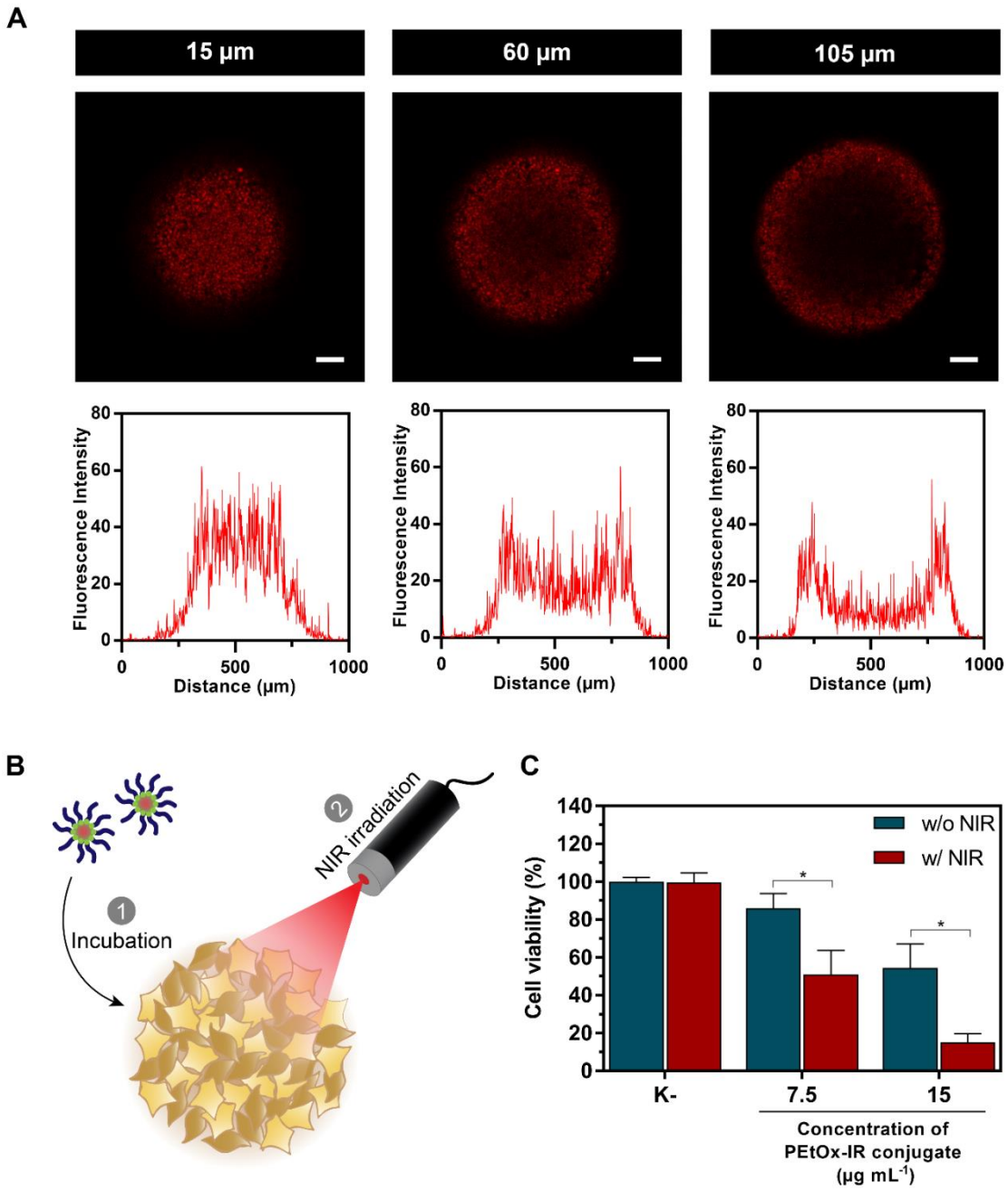

Figure 4.13. Phototherapeutic effect of PEtOx-IR/TOS NPs in 3D *in vitro* cancer models. CLSM z-stacks of spheroids, after incubation with PEtOx-IR/TOS NPs (7.5 µg mL^{-1} of PEtOx-IR conjugate equivalents), at different penetration depths and respective Fluorescence Intensity plots (across the spheroids' diameter) (A). Red channel: IR780. Scale bars correspond to 100 µm. Schematic representation of the therapeutic procedure in the heterotypic spheroids (B). Evaluation of the effect mediated by PEtOx-IR/TOS NPs (at different concentrations of PEtOx-IR conjugate equivalents) w/o NIR and w/ NIR laser irradiation (808 nm, 1.7 W cm^{-2}, 5 min) on the viability of the spheroids (C). Negative control (K- w/o NIR) was spheroids only incubated with culture medium. K- w/ NIR represents spheroids solely exposed to NIR light. Data are presented as mean ± S.D, n = 30 (*p < 0.0001).

Finally, the phototherapeutic capacity of PEtOx-IR/TOS NPs in the spheroids (Figure 4.13B) was investigated. As expected, the NIR irradiation *per se* did not affect spheroids' viability (Figure 4.13C). Considering the spheroids' greater resistance to therapeutics' action [61, 63], these were incubated with a higher dose of PEtOx-IR/TOS NPs when compared to cancer cell monolayers (section 4.4.4.). Spheroids exposed to PEtOx-IR/TOS NPs at 7.5 μg mL^{-1} (of PEtOx-IR conjugate equivalents) displayed a viability of 86 %. At the same dose, the combination of PEtOx-IR/TOS NPs with NIR light further decreased spheroids' viability to 51 %. In turn, the phototherapeutic effect mediated by PEtOx-IR/TOS NPs at 15 μg mL^{-1} (of PEtOx-IR conjugate equivalents) reduced the spheroids' viability to only 15 %. These results further emphasize the critical role of spheroids in the drug discovery stage.

To further confirm these results, spheroids stained with Calcein-AM/PI were also imaged by CLSM (**Figure 4.14**). As expected, the non-treated spheroids and the spheroids solely exposed to NIR light presented an outer layer stained with Calcein-AM, indicating the presence of mostly viable cells. In turn, the amount of PI-stained cells increased after PEtOx-IR/TOS NPs incubation. The highest levels of PI staining were observed for spheroids treated with PEtOx-IR/TOS NPs plus NIR light.

In a recent work, IR780 and DOX loaded sulfobetaine methacrylate-based nanoparticles could diminish heterotypic spheroids' viability to 16 % upon NIR laser irradiation (9 μg mL^{-1} of IR780 equivalents; 6 μg mL^{-1} of DOX; 808 nm, 1.7 W cm^{-2}, 5 min) [31]. In another work, IR780 loaded PEG-based nanoparticles functionalized with the CRGDK peptide diminished HT-29 spheroids' viability to 54 % after NIR laser exposure (30 μg mL^{-1} of IR780 equivalents; 808 nm, 2 W cm^{-2}, 20 s) [65]. In this work, the combined action of PEtOx-IR/TOS NPs and NIR light (15 μg mL^{-1} of PEtOx-IR conjugate equivalents; 808 nm 1.7 W cm^{-2}, 5 min) decreased spheroids' viability to 15 %. In this way, the PEtOx-IR/TOS NPs are promising agents for application in breast cancer PTT.

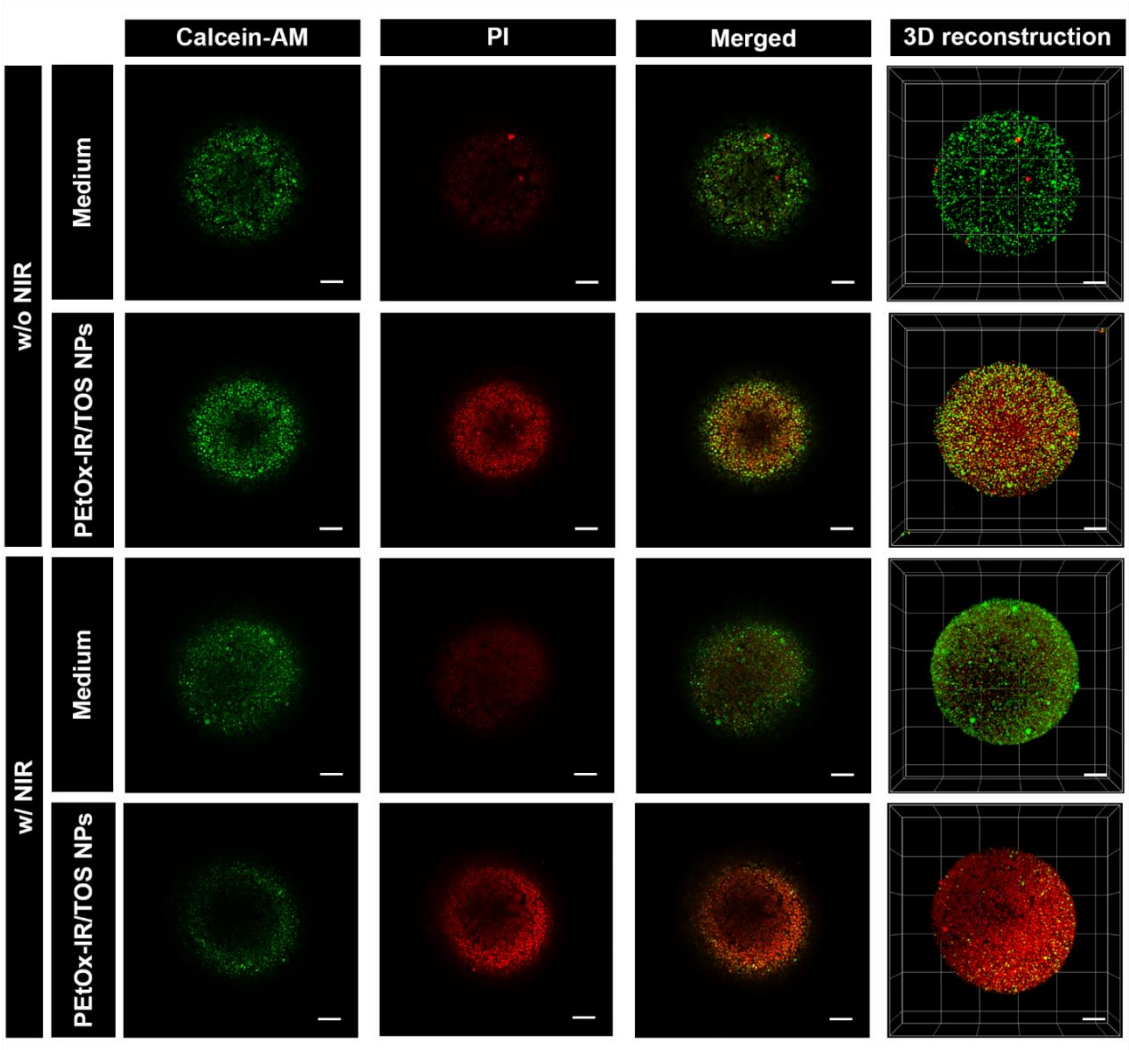

Figure 4.14. Live/Dead analysis of spheroids. CLSM images of spheroids stained with Calcein-AM/PI after exposure to PEtOx-IR/TOS NPs (15 μg mL^{-1} of PEtOx-IR conjugate equivalents) w/o NIR or w/ NIR irradiation (808 nm, 1.7 W cm^{-2}, 5 min). Medium w/o NIR represents non-treated spheroids and medium w/ NIR represents spheroids solely exposed to NIR irradiation. Green channel: Calcein-AM, red channel: PI. Scale bars correspond to 100 μm.

4.5. Conclusion

In this work, a PEtOx-IR conjugate was prepared for the first time, and it was combined with TOS through the nanoprecipitation technique, leading to the assembly of PEtOx-IR/TOS NPs. The PEtOx-IR/TOS NPs displayed suitable size (189.7 ± 4.4 nm) and surface charge (-7.8 ± 0.9 mV) for cancer-related applications. When incubated in different media, the PEtOx-IR/TOS NPs' size and NIR absorption did not suffer meaningful variations over time, displaying an optimal colloidal stability. In turn, the PEtOx-IR NPs (without TOS) did not reveal a suitable size distribution nor stability. Moreover, the PEtOx-IR/TOS NPs presented a 1.89- and 2.74-fold higher absorption at

808 nm than PEtOx-IR NPs and PEtOx-IR conjugates, hence presenting a greater photothermal potential. The PEtOx-IR/TOS NPs were also cytocompatible towards healthy cells at doses within the therapeutic range. When incubated in monolayers of cancer cells (2D *in vitro* cancer cell model), the PEtOx-IR/TOS NPs only diminished their viability to 80 %. In turn, the combination of PEtOx-IR/TOS NPs with NIR light almost led to complete cancer cell ablation (viability < 9 %). The therapeutic potential of PEtOx-IR/TOS NPs was also screened in heterotypic spheroids (3D *in vitro* cancer cell model), being capable of reducing the spheroids' viability to just 15 % upon NIR laser irradiation. Overall, the PEtOx-IR/TOS NPs are promising agents for application in breast cancer PTT.

4.6. References

[1] L. Zhao, Y. Xing, R. Wang, F. Yu, F. Yu, Self-Assembled Nanomaterials for Enhanced Phototherapy of Cancer, ACS Appl. Bio Mater., 3 (2019) 86-106.

[2] X. Li, S. Zhong, C. Zhang, P. Li, H. Ran, Z. Wang, MAGE-Targeted Gold Nanoparticles for Ultrasound Imaging-Guided Phototherapy in Melanoma, BioMed Res. Int., 2020 (2020) 6863231.

[3] A. Curcio, A.K. Silva, S. Cabana, A. Espinosa, B. Baptiste, N. Menguy, C. Wilhelm, A. Abou-Hassan, Iron oxide nanoflowers@ CuS hybrids for cancer tri-therapy: interplay of photothermal therapy, magnetic hyperthermia and photodynamic therapy, Theranostics, 9 (2019) 1288-1302.

[4] M.M. Leitão, D. de Melo-Diogo, C.G. Alves, R. Lima-Sousa, I.J. Correia, Prototypic heptamethine cyanine incorporating nanomaterials for cancer phototheragnostic, Adv. Healthcare Mater., 9 (2020) 1901665.

[5] R. Vankayala, K.C. Hwang, Near-infrared-light-activatable nanomaterial-mediated phototheranostic nanomedicines: an emerging paradigm for cancer treatment, Adv. Mater., 30 (2018) 1706320.

[6] H. Wang, X. Li, B.W.-C. Tse, H. Yang, C.A. Thorling, Y. Liu, M. Touraud, J.B. Chouane, X. Liu, M.S. Roberts, Indocyanine green-incorporating nanoparticles for cancer theranostics, Theranostics, 8 (2018) 1227-1242.

[7] C.G. Alves, R. Lima-Sousa, B.L. Melo, A.F. Moreira, I.J. Correia, D. de Melo-Diogo, Heptamethine Cyanine-Loaded Nanomaterials for Cancer Immuno-Photothermal/Photodynamic Therapy: A Review, Pharmaceutics, 14 (2022) 1015.

[8] C. Egloff-Juras, L. Bezdetnaya, G. Dolivet, H.-P. Lassalle, NIR fluorescence-guided tumor surgery: new strategies for the use of indocyanine green, Int. J. Nanomed., 14 (2019) 7823-7838.

[9] C.G. Alves, D. de Melo-Diogo, R. Lima-Sousa, E.C. Costa, I.J. Correia, Hyaluronic acid functionalized nanoparticles loaded with IR780 and DOX for cancer chemo-photothermal therapy, Eur. J. Pharm. Biopharm., 137 (2019) 86-94.

[10] T. Lin, A. Yuan, X. Zhao, H. Lian, J. Zhuang, W. Chen, Q. Zhang, G. Liu, S. Zhang, W. Cao, Self-assembled tumor-targeting hyaluronic acid nanoparticles for photothermal ablation in orthotopic bladder cancer, Acta Biomater., 53 (2017) 427-438.

[11] X. Qiu, L. Xu, Y. Zhang, A. Yuan, K. Wang, X. Zhao, J. Wu, H. Guo, Y. Hu, Photothermal ablation of in situ renal tumor by PEG-IR780-C13 micelles and near-infrared irradiation, Mol. Pharmaceutics, 13 (2016) 829-838.

[12] M.A. de Oliveira, M.G.C. Machado, S.E.D. Silva, T.L. Nascimento, E.M. Lima, G. Pound-Lana, V.C.F. Mosqueira, IR780-polymer conjugates for stable near-infrared labeling of biodegradable polyester-based nanocarriers, Eur. Polym. J., 120 (2019) 109255.

[13] A. Yuan, X. Qiu, X. Tang, W. Liu, J. Wu, Y. Hu, Self-assembled PEG-IR-780-C13 micelle as a targeting, safe and highly-effective photothermal agent for in vivo imaging and cancer therapy, Biomaterials, 51 (2015) 184-193.

[14] G. Wan, Y. Cheng, J. Song, Q. Chen, B. Chen, Y. Liu, S. Ji, H. Chen, Y. Wang, Nucleus-targeting near-infrared nanoparticles based on TAT peptide-conjugated IR780 for photo-chemotherapy of breast cancer, Chem. Eng. J., 380 (2020) 122458.

[15] J. Nicolas, Drug-Initiated Synthesis of Polymer Prodrugs: Combining Simplicity and Efficacy in Drug Delivery, Chem. Mater., 28 (2016) 1591-1606.

[16] S. Manandhar, E. Sjöholm, J. Bobacka, J.M. Rosenholm, K.K. Bansal, Polymer-Drug Conjugates as Nanotheranostic Agents, J. Nanotheranostics, 2 (2021) 63-81.

[17] I. Ekladious, Y.L. Colson, M.W. Grinstaff, Polymer–drug conjugate therapeutics: advances, insights and prospects, Nat. Rev. Drug Discovery, 18 (2019) 273-294.

[18] Z. Novy, V. Lobaz, M. Vlk, J. Kozempel, P. Stepanek, M. Popper, J. Vrbkova, M. Hajduch, M. Hruby, M. Petrik, Head-To-Head Comparison of Biological Behavior of Biocompatible Polymers Poly (Ethylene Oxide), Poly (2-Ethyl-2-Oxazoline) and Poly [N-(2-Hydroxypropyl) Methacrylamide] as Coating Materials for Hydroxyapatite Nanoparticles in Animal Solid Tumor Model, Nanomaterials, 10 (2020) 1690.

[19] H. Bludau, A.E. Czapar, A.S. Pitek, S. Shukla, R. Jordan, N.F. Steinmetz, POxylation as an alternative stealth coating for biomedical applications, Eur. Polym. J., 88 (2017) 679-688.

[20] O. Koshkina, D. Westmeier, T. Lang, C. Bantz, A. Hahlbrock, C. Würth, U. Resch-Genger, U. Braun, R. Thiermann, C. Weise, Tuning the Surface of Nanoparticles: Impact of Poly (2-ethyl-2-oxazoline) on Protein Adsorption in Serum and Cellular Uptake, Macromol. Biosci., 16 (2016) 1287-1300.

[21] S.Y. Fam, C.F. Chee, C.Y. Yong, K.L. Ho, A.R. Mariatulqabtiah, W.S. Tan, Stealth coating of nanoparticles in drug-delivery systems, Nanomaterials, 10 (2020) 787.

[22] H. Xu, W. Zhang, Y. Li, F.F. Ye, P.P. Yin, X. Yu, M.N. Hu, Y.S. Fu, C. Wang, D.J. Shang, The Bifunctional Liposomes Constructed by Poly(2-ethyl-oxazoline)-cholesteryl Methyl Carbonate: an Effectual Approach to Enhance Liposomal Circulation Time, pH-Sensitivity and Endosomal Escape, Pharm. Res., 31 (2014) 3038-3050.

[23] N. Gao, C. Xing, H. Wang, L. Feng, X. Zeng, L. Mei, Z. Peng, PH-responsive dual drug-loaded nanocarriers based on poly (2-Ethyl-2-Oxazoline) modified black phosphorus nanosheets for cancer chemo/photothermal therapy, Front. Pharmacol., 10 (2019) 270.

[24] A.S. Abu Lila, H. Kiwada, T. Ishida, The accelerated blood clearance (ABC) phenomenon: Clinical challenge and approaches to manage, J. Controlled Release, 172 (2013) 38-47.

[25] N. d'Avanzo, C. Celia, A. Barone, M. Carafa, L. Di Marzio, H.A. Santos, M. Fresta, Immunogenicity of polyethylene glycol based nanomedicines: mechanisms, clinical implications and systematic approach, Adv. Ther. (Weinheim, Ger.), 3 (2020) 1900170.

[26] N. Luo, J.K. Weber, S. Wang, B. Luan, H. Yue, X. Xi, J. Du, Z. Yang, W. Wei, R. Zhou, PEGylated graphene oxide elicits strong immunological responses despite surface passivation, Nat. Commun., 8 (2017) 1-10.

[27] C. Pais-Silva, D. de Melo-Diogo, I.J. Correia, IR780-loaded TPGS-TOS micelles for breast cancer photodynamic therapy, Eur. J. Pharm. Biopharm., 113 (2017) 108-117.

[28] M.-H. Tsai, C.-L. Peng, S.-J. Yang, M.-J. Shieh, Photothermal, targeting, theranostic near-infrared nanoagent with SN38 against colorectal cancer for chemothermal therapy, Mol. Pharmaceutics, 14 (2017) 2766-2780.

[29] C.G. Alves, D. de Melo-Diogo, R. Lima-Sousa, I.J. Correia, IR780 loaded sulfobetaine methacrylate-functionalized albumin nanoparticles aimed for enhanced breast cancer phototherapy, Int. J. Pharm., 582 (2020) 119346.

[30] R. Lima-Sousa, D. de Melo-Diogo, C.G. Alves, E.C. Costa, P. Ferreira, R.O. Louro, I.J. Correia, Hyaluronic acid functionalized green reduced graphene oxide for targeted cancer photothermal therapy, Carbohydr. Polym., 200 (2018) 93-99.

[31] I. Mó, C.G. Alves, D. de Melo-Diogo, R. Lima-Sousa, I.J. Correia, Assessing the Combinatorial Chemo-Photothermal Therapy Mediated by Sulfobetaine Methacrylate-Functionalized Nanoparticles in 2D and 3D In Vitro Cancer Models, Biotechnol. J., 15 (2020) 2000219.

[32] D. de Melo-Diogo, E.C. Costa, C.G. Alves, R. Lima-Sousa, P. Ferreira, R.O. Louro, I.J. Correia, POxylated graphene oxide nanomaterials for combination chemo-phototherapy of breast cancer cells, Eur. J. Pharm. Biopharm., 131 (2018) 162-169.

[33] G.G. Alvaradejo, M. Glassner, R. Hoogenboom, G. Delaittre, Maleimide end-functionalized poly (2-oxazoline) s by the functional initiator route: synthesis and (bio) conjugation, RSC Adv., 8 (2018) 9471-9479.

[34] E. Blanco, H. Shen, M. Ferrari, Principles of nanoparticle design for overcoming biological barriers to drug delivery, Nat. Biotechnol., 33 (2015) 941-951.

[35] H. Vu-Quang, M.S. Vinding, T. Nielsen, M.G. Ullisch, N.C. Nielsen, D.-T. Nguyen, J. Kjems, Pluronic F127-Folate Coated Super Paramagenic Iron Oxide Nanoparticles as Contrast Agent for Cancer Diagnosis in Magnetic Resonance Imaging, Polymers, 11 (2019) 743.

[36] M. Chen, N. Bhattarai, M. Cong, R.L. Pérez, K.C. McDonough, I.M. Warner, Mitochondria targeting IR780-based nanoGUMBOS for enhanced selective toxicity towards cancer cells, RSC Adv., 8 (2018) 31700-31709.

[37] Y. Tan, Y. Zhu, L. Wen, X. Yang, X. Liu, T. Meng, S. Dai, Y. Ping, H. Yuan, F. Hu, Mitochondria-Responsive Drug Release along with Heat Shock Mediated by Multifunctional Glycolipid Micelles for Precise Cancer Chemo-Phototherapy, Theranostics, 9 (2019) 691-707.

[38] Y. Li, M. Kröger, W.K. Liu, Shape effect in cellular uptake of PEGylated nanoparticles: comparison between sphere, rod, cube and disk, Nanoscale, 7 (2015) 16631-16646.

[39] D.R. Dias, A.F. Moreira, I.J. Correia, The effect of the shape of gold core–mesoporous silica shell nanoparticles on the cellular behavior and tumor spheroid penetration, J. Mater. Chem. B, 4 (2016) 7630-7640.

[40] D.B. Chithrani, Intracellular uptake, transport, and processing of gold nanostructures, Mol. Membr. Biol., 27 (2010) 299-311.

[41] K. Zhang, H. Fang, Z. Chen, J.-S.A. Taylor, K.L. Wooley, Shape effects of nanoparticles conjugated with cell-penetrating peptides (HIV Tat PTD) on CHO cell uptake, Bioconjugate Chem., 19 (2008) 1880-1887.

[42] M.J. Ernsting, M. Murakami, A. Roy, S.-D. Li, Factors controlling the pharmacokinetics, biodistribution and intratumoral penetration of nanoparticles, J. Controlled Release, 172 (2013) 782-794.

[43] J. Kulbacka, A. Pucek, M. Kotulska, M. Dubińska-Magiera, J. Rossowska, M.-P. Rols, K.A. Wilk, Electroporation and lipid nanoparticles with cyanine IR-780 and flavonoids as efficient vectors to enhanced drug delivery in colon cancer, Bioelectrochemistry, 110 (2016) 19-31.

[44] Y. Kuang, K. Zhang, Y. Cao, X. Chen, K. Wang, M. Liu, R. Pei, Hydrophobic IR-780 dye encapsulated in cRGD-conjugated solid lipid nanoparticles for NIR imaging-guided photothermal therapy, ACS Appl. Mater. Interfaces, 9 (2017) 12217-12226.

[45] K. Wang, Y. Zhang, J. Wang, A. Yuan, M. Sun, J. Wu, Y. Hu, Self-assembled IR780-loaded transferrin nanoparticles as an imaging, targeting and PDT/PTT agent for cancer therapy, Sci. Rep., 6 (2016) 1-11.

[46] M. Potara, T. Nagy-Simon, M. Focsan, E. Licarete, O. Soritau, A. Vulpoi, S. Astilean, Folate-targeted Pluronic-chitosan nanocapsules loaded with IR780 for near-infrared fluorescence imaging and photothermal-photodynamic therapy of ovarian cancer, Colloids Surf., B, 203 (2021) 111755.

[47] G. Liu, T. Lin, Q. Zhang, S. Zhang, C. Ji, S. Zhang, H. Guo, Hyaluronic Acid-IR780 Nanoparticles for Photothermal Ablation in Orthotopic Renal Cancer, J. Nanomater., 2020 (2020) 2421971.

[48] D. de Melo-Diogo, R. Lima-Sousa, C.G. Alves, I.J. Correia, Graphene family nanomaterials for application in cancer combination photothermal therapy, Biomater. Sci., 7 (2019) 3534-3551.

[49] Y. Chen, Z. Li, H. Wang, Y. Wang, H. Han, Q. Jin, J. Ji, IR-780 Loaded Phospholipid Mimicking Homopolymeric Micelles for Near-IR Imaging and Photothermal Therapy of Pancreatic Cancer, ACS Appl. Mater. Interfaces, 8 (2016) 6852-6858.

[50] F. Guo, M. Yu, J. Wang, F. Tan, N. Li, The mitochondria-targeted and IR780-regulated theranosomes for imaging and enhanced photodynamic/photothermal therapy, RSC Adv., 6 (2016) 11070-11076.

[51] C. Zhang, T. Liu, Y. Su, S. Luo, Y. Zhu, X. Tan, S. Fan, L. Zhang, Y. Zhou, T. Cheng, C. Shi, A near-infrared fluorescent heptamethine indocyanine dye with preferential tumor accumulation for in vivo imaging, Biomaterials, 31 (2010) 6612-6617.

[52] C. Jiang, H. Cheng, A. Yuan, X. Tang, J. Wu, Y. Hu, Hydrophobic IR780 encapsulated in biodegradable human serum albumin nanoparticles for photothermal and photodynamic therapy, Acta Biomater., 14 (2015) 61-69.

[53] N. Duhem, F. Danhier, V. Préat, Vitamin E-based nanomedicines for anti-cancer drug delivery, J. Controlled Release, 182 (2014) 33-44.

[54] C. Constantinou, A. Papas, A.I. Constantinou, Vitamin E and cancer: An insight into the anticancer activities of vitamin E isomers and analogs, Int. J. Cancer, 123 (2008) 739-752.

[55] A. Meyenberg, D. Goldblum, J.-M. Zingg, A. Azzi, K. Nesaretnam, M. Kilchenmann, B.E. Frueh, Tocotrienol inhibits proliferation of human Tenon's fibroblasts in vitro: a comparative study with vitamin E forms and mitomycin C, Graefe's Arch. Clin. Exp. Ophthalmol., 243 (2005) 1263-1271.

[56] A.K. Gupta, S. Wells, Surface-modified superparamagnetic nanoparticles for drug delivery: preparation, characterization, and cytotoxicity studies, IEEE Trans. Nanobioscience, 3 (2004) 66-73.

[57] F. Danhier, T.T.B. Kouhé, N. Duhem, B. Ucakar, A. Staub, N. Draoui, O. Feron, V. Préat, Vitamin E-based micelles enhance the anticancer activity of doxorubicin, Int. J. Pharm., 476 (2014) 9-15.

[58] M. Liu, P. Zhang, L. Deng, D. Guo, M. Tan, J. Huang, Y. Luo, Y. Cao, Z. Wang, IR780-based light-responsive nanocomplexes combining phase transition for enhancing multimodal imaging-guided photothermal therapy, Biomater. Sci., 7 (2019) 1132-1146.

[59] J. Song, N. Zhang, L. Zhang, H. Yi, Y. Liu, Y. Li, X. Li, M. Wu, L. Hao, Z. Yang, IR780-loaded folate-targeted nanoparticles for near-infrared fluorescence image-guided surgery and photothermal therapy in ovarian cancer, Int. J. Nanomed., 14 (2019) 2757-2772.

[60] M. Zanoni, F. Piccinini, C. Arienti, A. Zamagni, S. Santi, R. Polico, A. Bevilacqua, A. Tesei, 3D tumor spheroid models for in vitro therapeutic screening: a systematic approach to enhance the biological relevance of data obtained, Sci. Rep., 6 (2016) 1-11.

[61] H. Lu, M.H. Stenzel, Multicellular Tumor Spheroids (MCTS) as a 3D In Vitro Evaluation Tool of Nanoparticles, Small, 14 (2018) 1702858.

[62] G. Mehta, A.Y. Hsiao, M. Ingram, G.D. Luker, S. Takayama, Opportunities and challenges for use of tumor spheroids as models to test drug delivery and efficacy, J. Controlled Release, 164 (2012) 192-204.

[63] I. Mó, I.J. Sabino, D.d. Melo-Diogo, R. Lima-Sousa, C.G. Alves, I.J. Correia, The importance of spheroids in analyzing nanomedicine efficacy, Nanomedicine, 15 (2020) 1513-1525.

[64] X. Wang, X. Zhen, J. Wang, J. Zhang, W. Wu, X. Jiang, Doxorubicin delivery to 3D multicellular spheroids and tumors based on boronic acid-rich chitosan nanoparticles, Biomaterials, 34 (2013) 4667-4679.

[65] C. Zhao, Y. Tong, X. Li, L. Shao, L. Chen, J. Lu, X. Deng, X. Wang, Y. Wu, Photosensitive Nanoparticles Combining Vascular-Independent Intratumor Distribution and On-Demand Oxygen-Depot Delivery for Enhanced Cancer Photodynamic Therapy, Small, 14 (2018) 1703045.

Chapter 5: Concluding Remarks and Future Trends

Concluding Remarks and Future Trends

Despite all the funding and human resources allocated to study cancer, this disease is still one of the leading causes of death worldwide. The currently available therapies to tackle this disease (*e.g.*, surgery, radiotherapy, chemotherapy, immunotherapy) have been proven to show lack of efficacy and selectivity towards cancer cells, causing severe side effects on patients. Due to these limitations, several researchers have been focusing their attention on alternative therapies that promise a greater efficacy and safety.

In this regard, PTT mediated by nanomaterials has been showing promising results for cancer therapy. The success of this therapeutic strategy depends on the nanomaterials' physicochemical features as well as on the laser's and nanostructures' optical properties. Regarding the nanomaterials' physicochemical properties, their size, charge, shape, and corona composition revealed to be of extreme importance since these affected their blood circulation time and consequently, their tumor uptake. In general, the optimization of the nanomaterials' size was intensively pursued to improve their tumor uptake (by taking advantage from the EPR effect). However, recent findings demonstrated that nanostructures can also exploit dynamic vents (also called spontaneous eruptions), that occur at the tumor vasculature, to achieve tumor uptake. Owing to this new phenomenon, the emphasis shifted to the modulation of the nanostructures' corona in order to improve their blood circulation time and hence the likelihood to benefit from these eruptions.

Furthermore, the laser-related parameters also revealed to be impactful in nanomaterials' mediated PTT. In this regard, the use of NIR light revelated to be of utmost importance since it displayed a suitable penetration depth and minimal off-target heating. Moreover, the optimization of the irradiation onset as well as the power density and irradiation protocol (time and number of irradiations) allowed the achievement of greater therapeutic outcomes. In what concerns the nanomaterials' optical properties, the use of nanostructures with high NIR absorption was essential due to their capacity to interact with NIR light. Furthermore, the nanostructures' photothermal conversion efficiency, singlet oxygen quantum yield, and photostability also had a decisive role.

Among the several NIR-absorbing photothermal nanoagents, those incorporating IR780 have been showing promising results in pre-clinical models. The IR780-based nanomaterials displayed a high versatility due to their ability to produce, upon NIR laser exposure, a temperature increase (PTT), reactive oxygen species (PDT) and/or emit fluorescence (imaging). Despite their potential, the vast majority of IR780-based

nanostructures has been functionalized with PEG with the intent to improve their tumor-homing capacity. Such approach has revealed to be unsuitable due to the growing evidence demonstrating the immunogenicity of PEGylated nanomaterials. Such fact has pushed the development and validation of alternative materials in the coating of IR780-based nanostructures.

In this way, the research work developed during this PhD aimed to validate the potential of novel materials as PEG alternatives, namely SBMA-brushes and PEtOx, in the coating of nanostructures incorporating IR780 intended for cancer PTT.

In the **first research work**, a novel SBMA-BSA polymer was produced and employed to encapsulate IR780 through the nanoprecipitation technique. The IR/SBMA-BSA NPs demonstrated an ideal size (≈ 96 nm) for cancer-related applications, neutral surface charge (≈ -9 mV), and stability in complex medium (DMEM-F12 supplemented with FBS). In stark contrast, their equivalents without SBMA functionalization (*i.e.*, IR/BSA NPs) displayed a negatively charged surface (≈ -12 mV) and their size increased overtime when incubated in the previously described medium. These properties displayed by the IR/SBMA-BSA NPs (neutral surface charge and improved colloidal stability) enabled this formulation to achieve a 1.9-fold greater uptake by MCF-7 cells when compared to IR/BSA NPs. When combined with NIR light, the IR/SBMA-BSA NPs diminished the MCF-7 cells' viability to just 12 %.

In the **second research work**, a novel amphiphilic PEtOx-IR conjugate was produced and combined with TOS through nanoprecipitation technique, yielding PEtOx-IR/TOS NPs. This nanoformulation also displayed a suitable size (≈ 190 nm) as well as a neutral surface charge (≈ -8 mV). Similar to the first research work, herein, the size and NIR absorption of PEtOx-IR/TOS NPs did not change meaningfully when incubated in complex medium (DMEM-F12 supplemented with FBS). The PEtOx-IR/TOS NPs could be successfully internalized by MCF-7 cells, reducing their viability to just 9 % upon NIR laser irradiation. When evaluated in heterotypic spheroids, the PEtOx-IR/TOS NPs could penetrate into their 3D mass and, after laser exposure, reduced their viability to just 15 %.

Overall, the obtained results showed that the passivation of IR780-based nanomaterials with SBMA- and PEtOx-based coatings can improve their surface charge and colloidal stability, yielding nanostructures with enhanced biological properties whose PTT diminished the viability of relevant breast cancer *in vitro* models. In this way, the data obtained during this PhD establishes the applicability of these novel coatings in the

functionalization of IR780-based nanomaterials. In fact, SBMA and PEtOx appeared to be promising coatings to be used as PEG alternatives.

There are some key points that need to be considered as **future perspectives** regarding IR780-based nanomaterials' PTT (being also applicable to other photothermal nanoagents). The **combination of PTT with other therapeutic modalities**, such as chemotherapy or immunotherapy, is highly desirable. In fact, combinatorial therapeutic approaches allow these nano-systems to kill the cancer cells through different mechanisms, which is of extreme importance since human tumors are highly heterogenic, showing resistance through specific pathways [1, 2]. Additionally, the nanomaterials' photoinduced heat can trigger the release of the encapsulated therapeutic agents and sensitize cancer cells to their action [3]. Such can enable the use of lower doses of both therapeutics by exploiting synergistic effects. Moreover, due to the nanostructures' greater accumulation at the tumor periphery, the photothermal effect is mostly limited to this zone [4]. In this way, the combination of PTT with drug delivery is also important since the released drugs may reach deeper zones of the tumor mass, leading to a better therapeutic outcome [5-7]. Recently, it was shown that the PTT mediated by IR780-based nanomaterials can trigger the release of tumor-associated antigens and damage-associated molecular patterns [8]. Thereby, these events can be explored in combination with immunostimulants and/or immune checkpoint inhibitors, paving the way for the establishment of immune system responses towards local and metastasized cancer cells [8]. As importantly, this nanomaterial-immune system crosstalk may lead to the establishment of memory that prevents tumor's recurrence [8].

Moreover, the **large-scale production** of these photothermal nanoagents also needs to be fine-tuned. Before reaching clinical trials, the nanostructures' assembly methods need to be optimized from a milligram lab scale to a multi-gram industrial scale. Achieving such goal is a complex process since larger batches carry a greater difficulty in controlling the dimensions of these structures at the desired nanoscale [9, 10]. In this regard, the fabrication of nanostructures using microfluidic apparatus should be further pursued since it can potentially allow a good control over the nanomaterials' physicochemical properties as well as high production yields [11, 12].

Lastly, another important concern regarding nanomaterials' PTT is their **long-term biocompatibility**. In this regard, it is fundamental to develop nanomaterials with FDA/EMA approved materials as well as to use photothermal nanoagents that are easily

biodegraded/cleared. As importantly, this long-term biocompatibility should be assessed in small and large animal models.

5.1. References

[1] J. Wang, X. Wu, P. Shen, J. Wang, Y. Shen, Y. Shen, T.J. Webster, J. Deng, Applications of Inorganic Nanomaterials in Photothermal Therapy Based on Combinational Cancer Treatment, Int. J. Nanomed., 15 (2020) 1903-1914.

[2] T. Ahmad, R. Sarwar, A. Iqbal, U. Bashir, U. Farooq, S.A. Halim, A. Khan, A. Al-Harrasi, Recent advances in combinatorial cancer therapy via multifunctionalized gold nanoparticles, Nanomedicine, 15 (2020) 1221-1237.

[3] A. Zhang, L. Hai, T. Wang, H. Cheng, M. Li, X. He, K. Wang, NIR-triggered drug delivery system based on phospholipid coated ordered mesoporous carbon for synergistic chemo-photothermal therapy of cancer cells, Chin. Chem. Lett., 31 (2020) 3158-3162.

[4] Y. Liu, B.M. Crawford, T. Vo-Dinh, Gold nanoparticles-mediated photothermal therapy and immunotherapy, Immunotherapy, 10 (2018) 1175-1188.

[5] F.Z. Dahmani, D. Zhong, Y. Qi, A.E.G. Dahmani, T. Xie, B. Zhou, W. Li, K. Yao, L. Li, M. Zhou, A size-tunable and multi-responsive nanoplatform for deep tumor penetration and targeted combinatorial radio-/chemotherapy, J. Mater. Chem. B, 7 (2019) 4484-4498.

[6] C. Li, X.Q. Yang, J. An, K. Cheng, X.L. Hou, X.S. Zhang, X.L. Song, K.C. Huang, W. Chen, B. Liu, Y.D. Zhao, T.C. Liu, A near-infrared light-controlled smart nanocarrier with reversible polypeptide-engineered valve for targeted fluorescence-photoacoustic bimodal imaging-guided chemo-photothermal therapy, Theranostics, 9 (2019) 7666-7679.

[7] Q. Xu, Q. Li, Z. Yang, P. Huang, H. Hu, Z. Mo, Z. Qin, Z. Xu, T. Chen, S. Yang, Lenvatinib and Cu 2− x S nanocrystals co-encapsulated in poly (d, l-lactide-co-glycolide) for synergistic chemo-photothermal therapy against advanced hepatocellular carcinoma, J. Mater. Chem. B, 9 (2021) 9908-9922.

[8] C.G. Alves, R. Lima-Sousa, B.L. Melo, A.F. Moreira, I.J. Correia, D. de Melo-Diogo, Heptamethine Cyanine-Loaded Nanomaterials for Cancer Immuno-Photothermal/Photodynamic Therapy: A Review, Pharmaceutics, 14 (2022) 1015.

[9] S. Cheng, J. Qian, X. Zhang, Z. Lu, B. Pan, Commercial Gel-Type Ion Exchange Resin Enables Large-Scale Production of Ultrasmall Nanoparticles for Highly Efficient Water Decontamination, Engineering, (2021).

[10] C.S. Morales, P.M. Valencia, A.B. Thakkar, E. Swanson, R. Langer, Recent developments in multifunctional hybrid nanoparticles: opportunities and challenges in cancer therapy, Front. Biosci., Elite Ed., 4 (2012) 529-545.

[11] T.F. Abelha, T.W. Phillips, J.H. Bannock, A.M. Nightingale, C.A. Dreiss, E. Kemal, L. Urbano, J.C. deMello, M. Green, L.A. Dailey, Bright conjugated polymer nanoparticles containing a biodegradable shell produced at high yields and with tuneable optical properties by a scalable microfluidic device, Nanoscale, 9 (2017) 2009-2019.

[12] T. Baby, Y. Liu, A.P.J. Middelberg, C.-X. Zhao, Fundamental studies on throughput capacities of hydrodynamic flow-focusing microfluidics for producing monodisperse polymer nanoparticles, Chem. Eng. Sci., 169 (2017) 128-139.